GaAs Quantum Well Devices For Detection and Nonlinear Optics in the Mid-Infrared

Thesis by
Ilan Gravé

In Partial Fulfillment of the Requirements
for the Degree of
Doctor of Philosophy

California Institute of Technology
Pasadena, California
1993
(Defended April 28, 1993)

To my mother

and to the memory of my father

Acknowledgements

It is a great pleasure to acknowledge the support and encouragement of my advisor, Professor Amnon Yariv. He has been a source of continuous inspiration. In his group I found the atmosphere and resources necessary for exciting research and for blending my experience from the past with new, reinvigorating challenges. I would like to thank all the talented members of this group for the stimulating environment they provided all along the way. In particular I enjoyed the collaboration and the friendship of Dr. Mordechai Segev. I thank Lars Eng for introducing me to molecular beam epitaxy (MBE) and for sharing with me his knowledge and skills in that field. I have benefitted from the collaboration and the discussions with Ali Shakouri, in the work on tunable detectors. I acknowledge helpful discussions with Dr. Yaakov Shevy, Dr. Amir Sa'ar, Sidney Kan and Nao Kuze. I have greatly enjoyed and benefitted from collaborations with Drs. Shmuel Borenstain, Dan Rich and Anders Larsson from J.P.L. I would like to acknowledge the complementary measurements for characterization and calibration of infrared detectors performed by Dr. Tim Krabach and Susan Dejewsky at JPL. I would also like to thank the staff of the Microelectronics Devices Laboratory at JPL, for allowing me to use most of the equipment, during the first stage of my research, when I was just starting to set up the lab and the facilities at Caltech.

I have greatly enjoyed the collaboration with Dr. Giora Griffel, in additional exciting research in semiconductor lasers, performed during my Caltech years, but not included among the topics of this thesis.

A special word of acknowledgement to Prof. Bruno Crosignani, from the Universities of Roma and L'Aquila in Italy. During his summer stays at Caltech I enjoyed the privilege of learning from his vast knowledge and intuition in physics, from his incomparable culture and unique personality. (And I also received from him an endless number of "assists" on the soccer field.)

The technical assistance of Desmond Armstrong, Ali Ghaffari, Larry Begay, Tony Stark, and Kevin Cooper is acknowledged: they made possible, and easier, much of the experimental work. The help and kindness of Jana Mercado, Linda Dozsa and Paula Samazan is truly appreciated.

To my wife Yarona and my children Lidar and Daniel, thanks for the love, the support and the so-many wonderful moments during these beautiful years in Pasadena. Thanks to my mother and to my sister Nava for their continuous encouragement, love and support from overseas.

Abstract

The basic physical limits for infrared detection based on intersubband processes in semiconductor quantum wells are presented. An evaluation of the potential of GaAs intersubband detectors and a comparison with other systems is attempted. It is shown that the performances of the single GaAs detector falls short with respect to the single HgCdTe detector. Still, the performances of GaAs intersubband detectors answer the needs of many conceivable applications; this fact, together with the maturity, integrability and uniformity of the cheaper GaAs technology might make these detectors the choice for many future applications and systems.

Optimization of parameters in the design and epitaxial growth of these structures yield standard intersubband detectors with very respectable performances at reasonable cooling costs.

The narrow bandwidth and the lack of post-growth tunability limit the capability and versatility of intersubband detection. A new kind of intersubband detector, the multi-stack integrated detector, is conceived in an attempt to address these issues. This detector can operate in a number of modes; it can have a narrow or wide bandwidth of detection, and even a voltage-controlled expandable bandwidth. Among its features a multi-color option and a switching-peak option for combined or alternate color detection. The underlying physics involves the formation, expansion and readjustment of electric field high and low domains along the multi-quantum well region.

Additional topics in the physics and applications of intersubband processes for detection of infrared light are explored: a band-gap design involving a variably-spaced superlattice barrier, is investigated by photocurrent spectroscopy. The experiments reveal the subtle breaking of the parity selection rules, and also the possibility of detecting infrared light at shorter wavelengths than previously thought possible in the GaAs/AlGaAs system.

The second part of this thesis deals with the study and observation of enhanced nonlinear optical effects at the mid infrared, close to intersubband resonances. Second harmonic generation is obtained around 5 µm. Third-order effects are then investigated in different experimental configurations, including the first observation of phase conjugation based on these nonlinearities. Very large third-order susceptibilities and intensity-dependent refractive indices are deduced from the experimental results.

Contents

Chapter 1

Introduction and review

1.1 Introduction

The development and improvement of advanced epitaxial crystal growth techniques such as molecular beam epitaxy (MBE) and metal-organic chemical vapour deposition (MOCVD) during the last two decades, has opened the door for the realization of devices in the quantum size regime. Quantum size phenomena can be observed when the experimental dimensions approach the order of magnitude of the DeBroglie wavelength associated with the system under investigation.

During the early seventies Tsu and Esaki introduced the ideas of resonant tunneling within the conduction band of a semiconductor and of a man-made superlattice, and predicted the occurrence of a negative differential conductance in the current-voltage characteristics [1,2]. The quantum size properties of engineered superlattices were also studied and observed by the same researchers a few years later [3,4]. This prompted an unprecedented effort to investigate both the fundamental aspects and the applications of man-made semiconductor materials. The tools needed to understand and design these artificial semiconductor structures, recognized under the label "bandgap engineering," were readily developed and improved.

At center stage, as the major building block of simple and more complex bandgap designs, stands the quantum well. A particle in one dimension, confined between two potential barriers represents the basic model of a quantum well. The Schroedinger equation for this system is the simplest, involving only the kinetic term and boundary conditions. Quantum wells can be realized with advanced epitaxy techniques by growing alternate layers of a low bandgap material and a higher bandgap material; the dimensions of such layers range from a few Angstroms to a few hundred Angstroms.

1.2 Background

The work presented in this thesis was performed using the GaAs/$Al_xGa_{1-x}As$ system. However, many other material systems can be used, and have been used, to realize quantum wells for different studies and applications.

Bulk GaAs has a bandgap of 1.42 eV at 300 ^{O}K, while in $Al_xGa_{1-x}As$ the bandgap increases monotonically with the Al percentage x. Some attributes of this material systems are well known. The GaAs/$Al_xGa_{1-x}As$ system is lattice matched over the whole alloying range. This allows the growth of heterojunctions which do not induce detrimental misfit dislocations. GaAs and $Al_xGa_{1-x}As$ (for $x < 0.42$) are direct bandgap materials. This allows high efficiency in light generation through the recombination of electrons and holes. The refractive index of GaAs is larger than that of $Al_xGa_{1-x}As$ at near infrared wavelengths: this fact is used for guiding the coherent radiation in quantum well lasers [5].

As a result of the fact that the electron effective mass in GaAs is quite small, and by using growth control to subnanometer scale, quantum wells with energy levels in the range of few tens to hundreds of millielectronvolts (meV), with respect to the GaAs bulk band edges, can be prepared. Transitions between these levels can be observed and used to the advantage of applications. The GaAs layer, sandwiched between the $Al_xGa_{1-x}As$ barriers, confines both the electrons and the holes, since at a GaAs/$Al_xGa_{1-x}As$ heterojunction about 60% of the bandgap difference is offset by the conduction band, while 40% is offset by the valence band. The carriers (electrons in the conduction band, holes in the valence band) are thus confined in one dimension, along the direction of the growth. In the additional two dimensions there is no confinement and the carriers behave like free carriers in the crystal, in the effective mass approximation. The carriers are then said to occupy energy subbands, rather than energy levels. The allowed energies of a carrier in a GaAs quantum well, retelative to the bulk GaAs band edges (the "bottom" of the well) are given, in the approximation of an infinitely deep square well by

$$E = E_n + \frac{h^2}{2m^*}(k_x^2 + k_y^2) \tag{1.1}$$

where m^* is the effective mass and has different value for different types of carriers, and k_x k_y are the wave vectors in the plane parallel to the layers. Denoting by d the width of the quantum well, the confinement energy is given by

$$E_n = \frac{\hbar^2}{2m^*}\left(\frac{n\pi}{d}\right)^2 \tag{1.2}$$

Interband transitions between the conduction band quantum well and the valence band quantum well have been the object of an extensive study in the past decade or so. In the GaAs/$Al_xGa_{1-x}As$ system, the interband wavelengths correspond to the near infrared, around 0.8 μm. Along with the basic study of how confinement in one of the three spatial dimensions affect the properties of bulk interband processes, some quantum well interband devices were found to largely benefit in performances, (mainly) due to the modified density of states arising from the confinement. The best known example refers to the most important optoelectronic device to date, the semiconductor laser [6]. In addition, new effects and devices were discovered and developed, while studying quantum well interband transitions: among them, it is noteworthy to mention devices based on the quantum confined Stark effect .

Intersubband transitions, or the transitions among different subbands within the conduction band quantum well (or the valence band quantum well) has been only more recently the subject of an intense research effort. One can probably consider the studies of inversion layers in Silicon, during the seventies, a precursor of the present research on intersubband transitions in quantum well systems [7]. In 1977 a few ideas about intersubband transitions in quantum wells and their applications were disclosed [8]. However, only in 1983, the two most important intersubband applications were proposed in details in two separate papers. Smith, Chiu, Margalit, Yariv and Cho proposed the intersubband and bound-to-continuum infrared detectors [9], while Gurnick and DeTemple discussed the possibility of enhanced optical nonlinearities associated with these transitions [10].

In 1985 West and Englash reported on the absorption of 10 μm light by a quantum well structure designed to have the energy separation between the two first subband corresponding to that wavelength. At the same time they measured the large oscillator strength of the transition [11]. In the following few years, intersubband infrared detectors displaying large responsivities and good detectivities have been demonstrated [12]. The enhancement, versatility and optimization of such detectors have become topics of intensive applied research .

During the same period, some theoretical works analyzed the possibility of generating second harmonic radiation using an intersubband resonance [13,14]; shortly later, in 1989, came the first demonstrations of second harmonic generation via intersubband transitions [15]. Apart from these two main applied efforts, additional topics involving intersubband transitions are nowadays being addressed by various research groups. Among them the monitoring of spontaneous emission [16], and the fabrication of modulators for the mid infrared [17]. A few research teams have started looking into the very challenging goal of designing an intersubband-based mid or far infrared semiconductor laser [18-20]. Such an invention would be a breakthrough and would open the way for many integrated applications in the mid infrared.

Even before one explores promising applications, the study of intersubband transitions offers a fascinating playground where to observe basic quantum mechanical effects, in the simplest of all quantum mechanical systems. One can directly witness many of the basic features and properties encountered in first courses of quantum mechanics; among them the quantization of energy levels in a quantum well, the formation of energy subbands, dipole radiation selection rules, parity selection rules and more. On the other hand, a simple model such as an infinitely deep quantum well or a finite depth quantum well are only first approximations, and much more complexity is introduced by the presence of real materials, band structures, and dense carrier concentrations.

1.3 Intersubband versus interband transitions

Interband transitions involve two levels in two different bands. Thus the wave functions of the two states have different Bloch functions. Intersubband transitions instead involve states within the same band, displaying same Bloch functions but different envelope functions. In the envelope function approximation [21], we can write the wavefunction of the states in the wells as

$$\Psi_{s,n,k_{\parallel}}(\mathbf{r}) = \Phi_{s,n}(z)\, U_{s,n}(\mathbf{r})\, e^{i\mathbf{k}_{\parallel}\cdot\mathbf{r}_{\parallel}} \tag{1.3}$$

where s is the index for the conduction or valence bands, n is the index for the subband in the quantum well, $\mathbf{r}_{\parallel} = (x,y)$ is the component of the position vector in the direction parallel to the surface of the layers, $\mathbf{k}_{\parallel} = (k_x, k_y)$ is the wave vector in the same parallel direction. $U_{s,n}(\mathbf{r})$ is the Bloch function, $\Phi_{s,n}(z)$ is the envelop function for subband n in band s. The orthogonality and normalization relations are

$$\frac{1}{d}\int_{-d/2}^{d/2} \Phi_n^*(z)\, \Phi_{n'}(z)\, dz = \delta_{n,n'} \tag{1.4a}$$

$$\frac{1}{a}\int_{\substack{\text{unit}\\\text{cell}}} U_s^*(\mathbf{r})\, U_{s'}(\mathbf{r})\, d\mathbf{r} = \delta_{s,s'} \quad . \tag{1.4b}$$

The matrix element for the interaction of the quantum well system with incident radiation is proportional to

$$\left\langle \psi_{s,n,\mathbf{k}_{\parallel}} \middle| \mathbf{A}\cdot\mathbf{P} \middle| \psi_{s',n',\mathbf{k}'_{\parallel}} \right\rangle \;\alpha\; \frac{1}{a}\int_{\substack{\text{unit}\\\text{cell}}} \varepsilon_{\parallel}\, d\mathbf{r}_{\parallel} \left[U_s^* \nabla_{\parallel} U_{s'} + U_s^*\, i\, \mathbf{k}'_{\parallel} U_s \right] \delta_{n,n'}\, \delta_{\mathbf{k}_{\parallel},\mathbf{k}'_{\parallel}} + $$
$$+ \frac{1}{d}\varepsilon_z \int_{-d/2}^{d/2} dz \left[\Phi_n^* \nabla_z \Phi_{n'} \right] \delta_{s,s'}\, \delta_{\mathbf{k}_{\parallel},\mathbf{k}'_{\parallel}} \quad . \tag{1.5}$$

A is the vector potential of the electromagnetic field and its direction is in the direction of the polarization vector ε . For interband transitions the second term

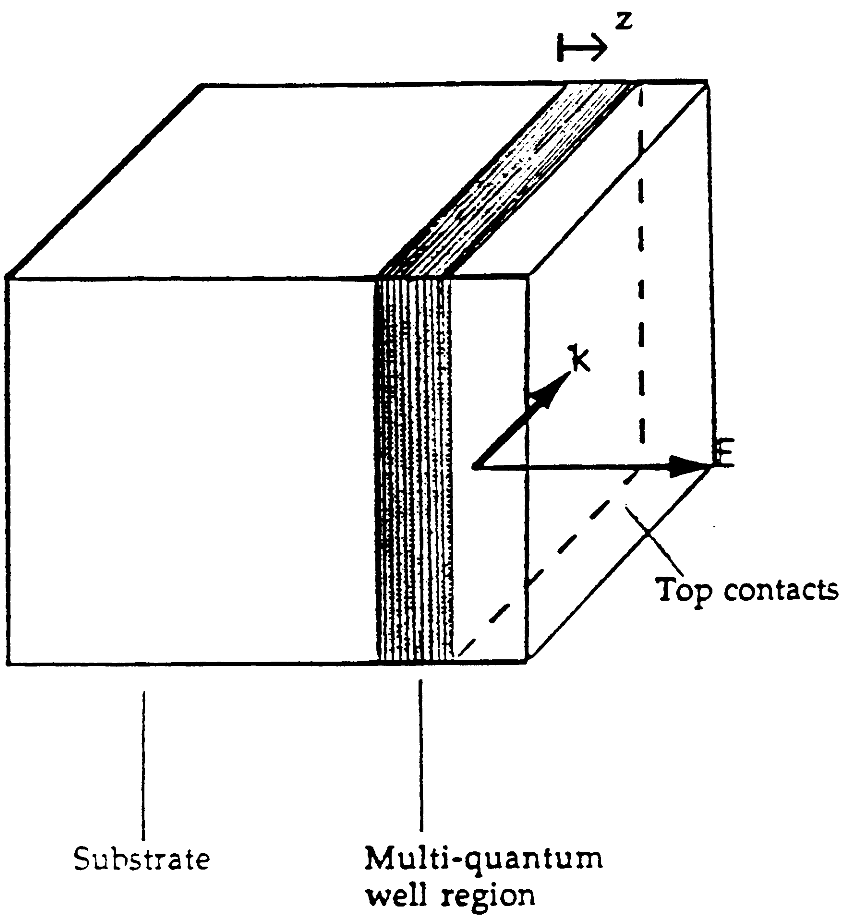

Figure 1.1. Intersubband selection rules for electric dipole transitions require the incident light to be polarized in the direction of the growth and the confinement, the z direction, as in the figure.

vanishes since $s \neq s'$ and the first term requires for n (in the conduction band quantum well) to be equal to n' (in the valence band quantum well). These are the well known selection rules for interband transitions for radiation in the near infrared in QW semiconductor lasers, for example.

We can see that the selection rules for the intersubband transition are quite different. In particular an intersubband transition can be induced only by light polarized in the plane of the quantum well [22], with the electric field in the direction of the growth, (the z direction in our notation), as portrayed in Figure 1.1. Whenever the configuration is symmetric, e.g., in a square well with symmetric barriers, additional selection rules allow nonvanishing transitions only for subbands of the same parity, within the same quantum well.

Another important difference is shown in Figure 1.2. Contrary to the large spread in energies allowed for interband QW transitions, for an intersubband transitions the energy range is very narrow, ideally a delta function, if one neglects the natural linewidth, nonparabolicity of the bands and a few additional broadening effects. In other words the joint density of states of the transition is much narrower for intersubband transitions.

A calculation of the energy levels of the subbands within the quantum well is of major concern in order to master the design of such structures. The starting model of an infinitely deep quantum well can be improved in successive steps, starting with a finite depth quantum well structure, with the barrier height corresponding to the conduction (or valence) band offset of the material (in our case AlGaAs). An

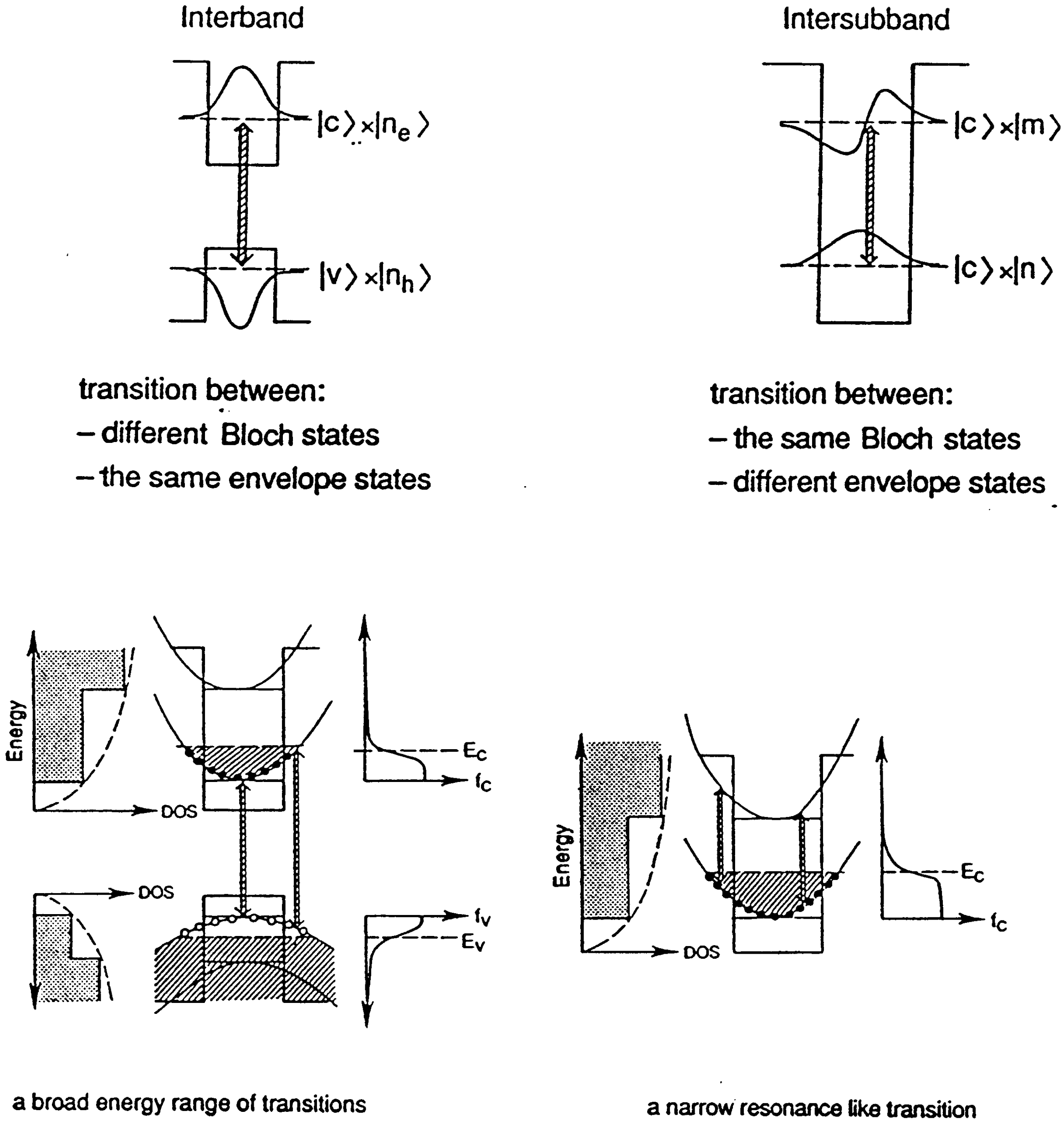

Figure 1.2. The nature of interband and intersubband transitions.

inclusion of the correct band structure can be attempted. Usually a band non-parabolicity term is included in most models, or a **k·p** theory is invoked to bring the model closer to reality. Energy shifts from the standard models, arising from various physical mechanisms have been calculated and observed, starting with the so-called depolarization shift, due to the fact that the carriers confined in the well form a degenerate two-dimensional electron gas and the excitations involve plasma-like modes in addition to single particle transitions [23]. A Coulomb direct shift has also to be included, tantamount to solve the Schroedinger equation in conjunction with Poisson's equation. Especially for large doping densities, the quantum mechanical behavior of identical Fermion particles, i.e., Pauli's exclusion principle or, equivalently, an anti-symmetrization requirement for the wave-functions are important. The energy levels have to be recalculated to include the exchange integral, and for electrons this generally means the lowering of the energy of the first heavily populated subband [24]. Even an exciton-like shift within the conduction band has been argumentatively calculated]25].

Energy broadening is also a topic of great importance, both when targeting a fundamental understanding of the relaxation processes, and when dealing with practical and applied aspects. Undoubtedly, one of the attractive features of the transition is the fact that it is fast, in the picosecond time regime. First of all, the transition has a finite lifetime which leads to some linewidth. In addition, various effects, such as the nonparabolicity of the bands and the dependence of the effective barrier height, as seen by the electrons in the well, on traverse momentum wavevector, induce a homogeneous broadening, while variations in well widths over the growth of a multi quantum well system add some inhomogeneous broadening.

Experimental evidence clearly indicates that the main mechanism for a fast relaxation is the scattering of carriers by optical longitudinal phonons. Experiments performed on different samples, with subband separation designed above and below the optical phonon threshold (36 meV), show a dramatical increase in the relaxation times when no optical phonons are present, from few picoseconds to few hundred picosecond [26]. This could have a large importance on the eventual feasibility and design of an intersubband laser, since the requirement of population inversion, within standard schemes, would need a relaxation time not worse than some attainable pumping time; this would seem to favour the effort for an intersubband laser at longer wavelengths, below the optical phonon threshold [27].

1.4 Intersubband and bound-to-continuum detectors

One can use intersubband transitions to detect infrared light. The idea, as proposed by Smith et al. [9], involves the excitation of carriers from a ground-state subband inside one of the quantum wells , to an excited subband located in energy just close to the top of the well, or even above the barrier level, in the continuum. Technically we call these bound-to-continuum transitions (or bound-to-extended-states transitions), as opposed to bound-to-bound excitations. An electric field, applied through electrodes on opposite side of the quantum well or multi-quantum well region, collects the carriers and a photocurrent can thus be measured. The transport is through the continuum in the bound-to-extended configuration, or involves some tunneling through the barriers, if the bound-to-bound design is used. These schemes are plotted in Figure 1.3. Experiments showed that performances of detectors (in terms of internal quantum efficiencies or responsivities) are largely enhanced in the bound-to-extended configuration. An optimum is achieved when the excited subband is just very close to the top of the well at the conduction band edge of the barrier [28]. Bound-to-continuum transitions display wider bandwidth than bound-to-bound configurations . An optimized detector can display a spectral bandwitdh 10-40% of its central wavelength. Designing the quantum well so that the excited level will be well above the barrier, deep into the continuum, allows for a somewhat larger bandwidth at the expense of a reduced responsivity [29]. Optimizing the performances of devices, along with figures of merit used in detector characterization, required the understanding of basic limits in the detection mechanism [30], as well as some efforts in optimizing materials, epitaxial growth, band engineering and overall design of these structures. Additional efforts have also addressed the versatility of these detectors and the improvement of many aspects for different applications. One example is the quest to expand the wavelength range where these detectors are effectively used (7 - 12 μm) towards longer or shorter wavelengths [31,32].

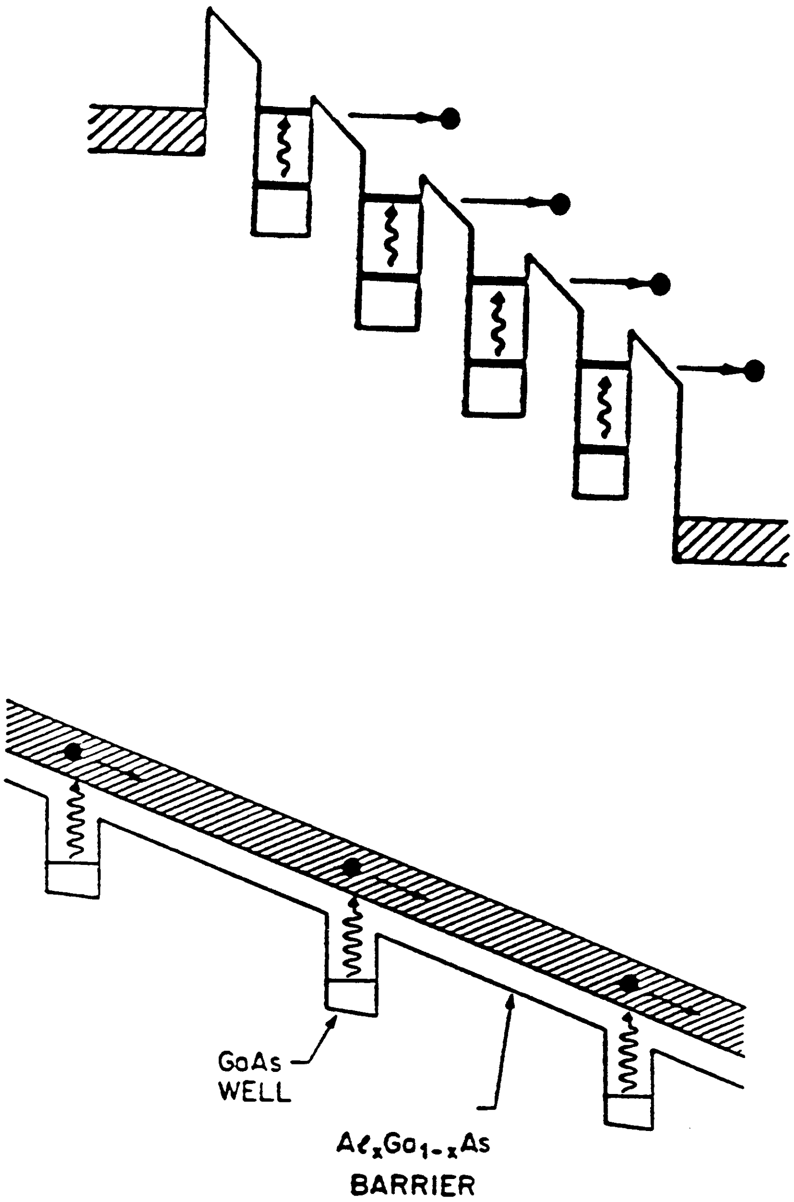

Figure 1.3. Intersubband infrared detection schemes based on bound-to-bound transitions (top) and on bound-to-continuum excitations (bottom).

Other efforts have tryed to implement the same schemes of intersubband detection in various materials , in a search for systems displaying improved performances [33,34].

1.5 Nonlinear optics via intersubband transitions

The transitions between the subbands of a quantum well have extremely large oscillator strengths. The dipole moment associated with these transitions is of the order of the electric charge e times the QW size d (~ 20-100 Å), which isquite large. The nonlinear susceptibility of order n is proportional to the product of (n+1) dipole matrix elements. Although other factors do influence the relative magnitude of the susceptibility, such as the density of available carriers and the dephasing time T_2 of the transitions, it is apparent that large nonlinear susceptibilities can be expected near intersubband resonances. Enhanced nonlinear effect over what is observed in bulk are possible close to the resonance. Even-order nonlinearities can be further enhanced by careful design and bandgap engineering: asymmetrical well configurations can be used to enlarge the mean electronic displacement during optical transitions. Electrical fields can be used to finely tune subband separations to achieve multi-resonance situations.

Additional experimental results on second order nonlinearities, second-harmonic generation and optical rectification, confirmed that large second-order susceptibilities could be obtained in QW structures via intersubband transitions [35,36]. Enhancement over bulk value of up to three order of magnitudes were measured.

There is a strong incentive to study third-order nonlinear effects, coming both from the expectation of large enhancements over bulk values and from the fact that third-order nonlinearities are much useful for a large number of optical signal processing applications.

1.6 Outline of the thesis

This thesis is based on the work of the author in the field of intersubband devices, during his residence at Caltech for studies towards the Ph.D degree. Contributions to additional topics in optoelectronics and semiconductor devices, generated during the same period, are not presented here, and the interested party would have to refer to the relevant publications [37-40].

Following these introductory paragraphs, chapter 2 will present the basic physical limits for intersubband detection [30,41]. Different detection regimes, where thermally limited detection or background limited detection are predominant will be analyzed. The chapter will conclude with an appraisal of the performances of $GaAs/Al_xGa_{1-x}As$ intersubband detectors in comparison to the state-of-the-art technology for infrared detectors, based on the HgCdTe material system.

Chapter 3 will present the procedures and techniques involved in the design, growth and characterization of intersubband infrared detectors and nonlinear optics samples. These experimental efforts included the optimization of MBE growth for intersubband samples; the development and implementation of a number of processes for sample preparation and characterization; the development of absorption and photocurrent intersubband spectroscopies; the build-up of a cryogenic liquid Helium station for the characterization and calibration of detector performances; the introduction of 10 μm optics set-up, including coherent and broadband sources. Chapter 3 will conclude presenting our results on "standard" intersubband detectors, displaying excellent performances in terms of the commonly used figures of merits, responsivities, dark currents, noise performances and detectivities [42].

Chapter 4 will present our idea, design and results for a novel intersubband detector, capable of working in a number of modes, and addressing some of the most important issues in performances and versatility for intersubband detectors [43,44]. Among its capability a voltage-controllable bandwidth, tunability and multicolor operation. In this chapter we shall briefly recognize the very interesting physics underlying this multi-mode operation, which involves the formation, expansion and readjustment of static electric field domains in the active multi-quantum well region.

Chapter 5 will feature the characterization and analysis of a sophisticated multi quantum well intersubband structure, known as the variably spaced superlattice electron filter (VSSEF). This chapter is the outcome of a wide collaboration including a team at the Jet Propulsion Laboratory (JPL), a team at Chalmers University in Sweden where the sample was grown, and the author [45]. The experimental results here show a subtle way to observe "forbidden" transitions due to the breaking of parity symmetry in the wells ; new type of peaks and features occur in the intersubband absorption spectra, shown to be linked with states localized in the barriers; an interesting photocurrent spectroscopy also reveals how forbidden transitions can be used, in principle, for detection at wavelengths much shorter than usually thought. This work also features the first demonstration of photon-assisted resonant tunneling. Finally a simple model gives an acceptable fit to the experimental results.

In chapter 6 and 7 our work on intersubband nonlinear effects will be presented. Chapter 6 deals with second-order nonlinear effects, more specifically second-harmonic generation; following an introduction to the subject our experimental results on second-harmonic generation in long samples are presented [46]. Chapter 7 describes the demonstration and measurements of third-order effects, including the dc Kerr effect [47], phase conjugation at 10.6 μm [48] and the optical Kerr effect [49].

References

[1] L. Esaki and R. Tsu, IBM J. Res. Dev. 14, 61 (1970).

[2] R. Tsu and L. Esaki, Appl. Phys. Lett. 22, 562 (1973).

[3] L.L. Chang, L. Esaki, and R. Tsu, Appl. Phys. Lett. 24, 593 (1974).

[4] L. Esaki and L.L. Chang, Phys. Rev. Lett. 33, 495 (1974).

[5] A. Yariv: "Quantum Electronics", 3rd ed. , J. Wiley & Sons .

[6] P.L. Derry, A. Yariv, K.Y. Lau, N. Bar-Chaim, and J. Rosenberg, Appl. Phys. Lett. 50, 1773 (1987).

[7] R.G. Wheeler and H.S. Goldberg, IEEE Trans. Electron. Dev. ED-22, 1001 (1975).

[8] L.L. Chang, L. Esaki, and G.A. Sai-Halash, IBM Techn. Discl. Bull. 20, 2019 (1977).

[9] J.S. Smith, L.C. Chiu, S. Margalit, A. Yariv and A.Y. Cho, J. Vac. Sci. Technol. B1, 376 (1983).

[10] M.K. Gurnick and T.A. DeTemple, IEEE J. Quantum Electron., QE-19, 791 (1983).

[11] L.C. West and S.J. Englash, Appl. Phys. Lett. 46, 1156 (1985).

[12] B.F. Levine, C.G. Bethea, G. Hasnain, J. Walker, and R.J. Malik, Appl. Phys. Lett. 53, 296 (1988).

[13] Z. Ikonic, V. Milanovic and D. Tjapkin, IEEE J. Quantum Electron. QE-25, 54 (1989).

[14] J. Khurgin, Appl. Phys. Lett. 51, 2100 (1987); J. Khurgin, Phys. Rev. B 38, 4056 (1988).

[15] M.M. Fejer, S.J.B. Yoo, R.L. Byer, A. Harwit and J.S. Harris, Jr., Phys. Rev. Lett. 62, 1041 (1989).

[16] M. Helm, P. England, E. Colas, F. DeRosa, and S.J. Allen, Jr., Phys. Rev. lett. 63, 74 (1989).

[17] Y.J. Mii, R.P.G. Karunasuri, K.L. Wang, M. Chen, and P.F. Yuh, Appl. Phys. Lett. 56, 1986 (1990).

[18] P.F. Yuh, and K.L. Wang, Appl. Phys. Lett. 51, 1404 (1987).

[19] A. Kastalsky, V.J. Goldman, and J.H. Abeles, Appl. Phys. Lett.59, 2 636 (1991).

[20] Q. Hu and S. Feng, Appl. Phys. Lett. 59, 2923 (1991).

[21] G. Bastard, Phys Rev B 24, 5693 (1981); Phys Rev B 25, 7594 (1982).

[22] F. Stern, Phys. Rev. Lett. 33, 960 (1974).

[23] W.P. Chen, Y.J. Chen, E. Burstein, Surface Science 53, 263 (1976); S.J. Allen, Jr., D.C. Tsui, B. Vinter, Sol. State Commun. 20, 425 (1976)

[24] K.M.S.V. Bandara, D.D. Coon, Byungsung O, Y.F. Lin, and M.H. Francombe, Appl. Phys. Lett. 53, 1931 (1988).

[25] W.L. Bloss, J. Appl. Phys. 66, 3639 (1989).

[26] D.Y. Oberli, D.R. Wake, M.V. Klein, J. Klem, T. Henderson, and H. Morkoç, Phys. Rev. Lett. 59, 6796 (1987).

[27] S.I. Borenstain and J. Katz, Appl. Phys. Lett. 55, 654 (1989).

[28] D.D. Coon and P.G. Karunasuri, Appl. Phys. lett. 45, 649 (1984); K.W. Goossen and S.A. Lyon, J. Appl. Phys. 63, 5149 (1988).

[29] B.F. Levine, G. Hasnain, C.G. Bethea, N. Chand, Appl. Phys. Lett. 54, 2704 (1989).

[30] M.A. Kinch and A. Yariv, Appl. Phys. Lett. 55, 2093 (1989)

[31] A. Zussman, B.F. Levine, J.M. Kuo, and J. de Jong, J. Appl. Phys. 70, 5101 (1991).

[32] H. Schneider, F. Fuchs, B. Dischler, J.D. Ralston, and P. Koidl, Appl. Phys. Lett. 58, 2234 (1991).

[33] S.D. Gunapala, B.F. Levine, R.A. Logan, T. Tanbun-Ek, and D.A. Humphrey, Appl. Phys. Lett. 57, 1802 (1990).

[34] S.D. Gunapala, B.F. Levine, D. Ritter, R. Hamm, and M.B. Panish, Appl. Phys. Lett. 58, 2024 (1991).

[35] E. Rosencher, P. Bois, J. Nagle and S. Delaitre, Electron. Lett., 25, 1063 (1989).

[36] E. Rosencher, P. Bois, J. Nagle , E. Costard and S. Delaitre, Appl. Phys. Lett. 55, 1597 (1989).

[37] I. Gravé, S.C. Kan, G. Griffel, S.W. Wu, A. Sa'ar, and A. Yariv, "Monolithic Integration of a Resonant Tunneling Diode and a Quantum Well Semiconductor Laser, "Appl. Phys. Lett. 58, 110 (1991).

[38] G. Griffel, W.K. Marshall, I. Gravé, and A. Yariv, " Frequency Control Using a Complex Effective Reflectivity in Laterally Coupled Semiconductor Laser Arrays, " Optics Letters 16, 1174 (1991).

[39] G. Griffel, H..Z. Chen, I. Gravé, and A. Yariv, " Single-mode Very Wide Tunability in Laterally Coupled Semiconductor Lasers with Electrically Controlled Reflectivities, " Appl. Phys. Lett. 58, 1827 (1991).

[40] A. Sa'ar, J. Feng, I. Gravé, and A. Yariv, "Resonsnt Tunneling Through Low Dimensional QWuantum Structures, " J. Appl. Phys. 72, 3598 (1992).

[41] I. Gravé and A. Yariv, "Fundamental Limits in Quantum Well Intersubband Detection," NATO ASI Series, Volume on Intersubband Transitions in Quantum

Wells. Editors: Rosencher, Vinter and Levine (1992).

[42] A. Yariv, M. Kinch, S.I. Borenstain and I. Gravé, Proceedings of the Innovative Long Wavelength Infrared Detector Workshop, Jet Propulsion Laboratory, Pasadena, CA, April 1990.

[43] I. Gravé, A. Shakouri, N. Kuze and A. Yariv, Appl. Phys. Lett. 60, 2362 (1992).

[44] A. Shakouri, I. Gravé, Y. Xu, A. Gheffari and A. Yariv, submitted to Appl. Phys. Lett.

[45] S.I. Borenstain, I. Gravé, A. Larsson, D.H. Rich, B. Jonsson, I. Andersson, J. Westin, T. Andersson, Phys. Rev. B 43, 9320 (1991).

[46] A. Sa'ar, I. Gravé, N. Kuze and A. Yariv, Proceedings of the OSA Topical Meeting on Nonlinear Optics (NLO90), Kauai, Hawaii, July 1990.

[47] A. Sa'ar, N. Kuze, J. Feng, I. Gravé and A. Yariv, Appl. Phys. Lett. 61, 1263 (1992).

[48] I. Gravé, M. Segev and A. Yariv, Appl. Phys. Lett. 60, 2717 (1992).

[49] M. Segev, I. Gravé and A. Yariv, Appl. Phys. Lett. 61, 2403 (1992).

Chapter 2

Fundamental limits in intersubband detection

2.1 Introduction

Since the concept was first proposed by Smith et al. [1], the understanding of infrared photodetection by intersubband and bound-to-continuum transitions has been deepened and carried to new promising frontiers in a relatively short time; many additional features of these detectors, including some relevant to users' needs, have been addressed and investigated: wide-band responses [2], grating-assisted frontal detection schemes [3,4] (to overcome basic selection rules limitations), photoconductive gains [5], tunability of the wavelength of detection [6-8] are just a few of the issues that have been undertaken and partially resolved. Most notably detectors presenting very respectable performances in terms of responsivity, noise figures and, ultimately, detectivity, have been demonstrated, mainly in the GaAs/AlGaAs system [9-11]. Typical wavelengths of detection in this material include the atmospheric window 8-12 μm and the range of detection can be pushed up and down a few microns by different techniques [12-14], or by using different, yet compatible, material systems [15-16].

The time had quickly come when, considering such demonstrated performances and thriving on the advantages of the mature, reliable and integrable GaAs material technology, hopes have arisen for the possibility of fabricating focal staring arrays with acceptable performances for many applications; and questions were asked about the performances of (GaAs) multi-quantum well detectors per se and with respect to other materials [17] and/or other schemes, including the Mercury-Cadmium-Telluride (HgCdTe) system, which has been considered for years the natural choice for many applications in the wavelength range described above.

Many are the issues involved when one tries to compare different technologies and different schemes of detection: these include the preparation of materials, the maturity, reliability and integrability of the technology, the capability of fabricating large arrays at highest yield and lowest cost; moreover technologies do evolve and what seems difficult or looks costly today could prove to be easy and cheap tomorrow. System considerations are very much important [18], yet different applications generally address different problems with different emphasis. All these and other issues have undoubtly to be addressed and weighted, at some stage, during the design of a system and before the choice of a technology for a particular application. The place to start, however, is an analysis of the fundamental limitations for a single element or detector, due to the basic physical processes involved in the detection mechanism. This can both serve the understanding of the basic, ultimate limits and at the same time provide a meaningful comparison between different schemes and/or technologies. And this is what we shall attempt to do and review in this chapter [19].

2.2 Photoconductive gain in multi-quantum well detectors

We consider a multi-quantum well (MQW) long wavelength infrared detector consisting of a number of n-doped (GaAs) quantum wells confined by adjacent (AlGaAs) layers of higher potential barriers. The length of the barriers is assumed large enough that the quantum well are basically decoupled; this reflects also practical designs, since, in most cases, one wants to reduce the dark current due to tunneling. The operation of the MQW infrared detector (Figure 2.1), is based upon the excitation of electrons by an incident optical flux, from the lowest subband to the second subband, generally located very close to the top of the well or even in the continuum above the barrier. The application of an external electric field in the perpendicular transport direction will sweep the electrons towards the collecting contact and a photocurrent will be recorded. The MQW infrared detector in this configuration operates very similarly to a photoconductive detector.

Consider an optical field of power P and frequency ν which is incident on a MQW detector, or, for that matter, on any photoconductive detector. Denoting the probability for excitation of a single carrier by an incident photon by η, the so called quantum efficiency, the carrier generation rate is

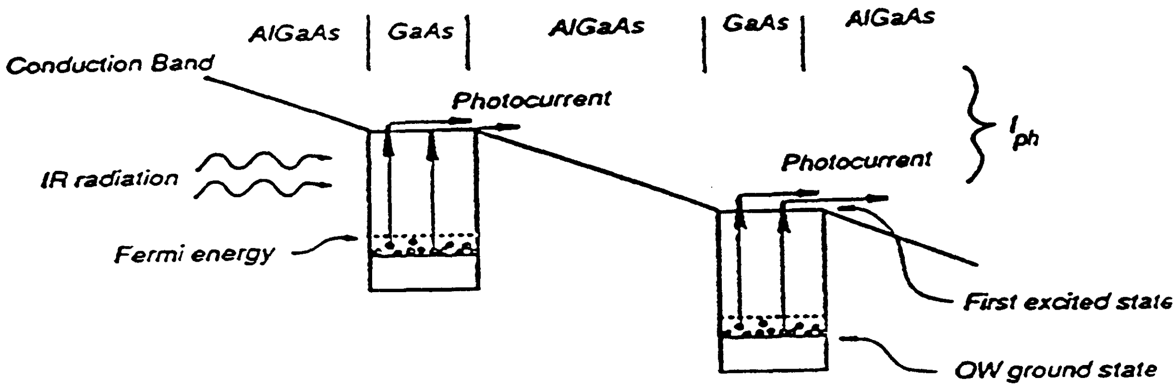

Figure 2.1. Operation of a multi quantum well intersubband infrared detector under applied bias. Infrared radiation, incident on the device, must have a component propagating in the plane of the grown layers, according to the selection rules. The wells are heavily doped with electrons, which absorb the infrared photons and are excited from the ground subband to a second subband located on top of the well. The excited carriers are then swept towards the anode by the applied electric field.

$$G = \frac{P\eta}{h\nu} \tag{2.1}$$

Assuming the carrier lasts on average τ_0 seconds before it is retrapped by a quantum well (or before it recombines, in other type of photoconductors), the average number of carriers N_c can be found by equating the generation rate to the recombination or retrapping rate.

$$N_c = G\tau_o = \frac{P\eta}{h\nu}\tau_o \tag{2.2}$$

The carriers drift under the influence of an applied electric field at a velocity $v = \mu E$, μ being the mobility and E the electric field. The contribution of each carrier to output current flowing in the external circuit is

$$i_e = \frac{ev}{l} \tag{2.3}$$

where l is the distance between electrodes. The total average current is thus

$$\bar{I} = N_c i_e = \frac{P\,\eta\tau_o e\,v}{h\,\nu l} = \frac{e\eta}{h\nu}\left(\frac{\tau_o}{\tau_d}\right)P \tag{2.4}$$

where $\tau_d = l/v$ is the drift time for a carrier across the length of the device. Notice that the average excited carrier drifts a fraction τ_o/τ_d of the crystal (if $\tau_o/\tau_d > 1$, then a photoconductive gain exists).

2.3 Generation-recombination noise in photoconductive detectors

The limiting noise mechanism in cooled, ideal photoconductive detectors, comes from the randomness inherent in current flow. Even if the incident optical flux were constant in time, the generation of carriers by the flux would still constitute a random process. Moreover, the lifetime τ is not a constant, but rather a random variable displaying a statistical distribution, whose mean value is τ_o. To see how this randomness translates to output noise current, we consider a carrier excited by an absorbed photon at $t' = 0$ and lasting t seconds. The resulting current pulse is

$$i_e(t') = \left\{ \begin{array}{ll} \frac{ev}{l} & 0 < t' < t \\ & \\ 0 & otherwise \end{array} \right\} \qquad (2.5)$$

For a photoconductor in which generation-recombination effects are described by one lifetime τ, the distribution function of τ is taken to be exponential

$$g(\tau)\,d\tau = \tau_o^{-1} e^{-\tau/\tau_o} \tag{2.6}$$

Alternatively this corresponds to representing the process by a Langevin equation for the fluctuation ΔN in the number of carriers N.

$$\frac{d\Delta N(t)}{dt} = -\frac{\Delta N(t)}{\tau_o} + L(t) \qquad (2..7)$$

where $L(t)$ is a "white" source term

$$\overline{L(t)L(t')} = \delta(t-t') \tag{2.8}$$

Directly from the solution of (2.7)

$$\Delta N(t) = \int_{-\infty}^{t} L(t')e^{-(t-t')/\tau_o}\,dt' \tag{2.9}$$

one can get

$$\overline{\Delta N(t)\Delta N(t+s)} = \overline{\Delta N^2(t)}\; e^{-s/\tau_o} \tag{2.10}$$

Obtaining an autocorrelation function of the form

$$c(s) \equiv \frac{\overline{\Delta N(t)\Delta N(t+s)}}{\overline{\Delta N^2(t)}} = e^{-s/\tau_o} \tag{2.11}$$

for the fluctuation ΔN in the number of carriers N . Implicitely, we have assumed that either $\tau_o << \tau_d$ or that, upon the arrival of an individual carrier at the collecting contact, a "replacement" carrier is injected at the emitting contact within a time interval much smaller than τ_o. The latter assumption corresponds also to the condition $\tau_e << \tau_d$ where τ_e is the dielectric relaxation time in the material.

Applying the Wiener-Khintchine theorem, the spectral density function of the fluctuation ΔN in N (the number of excited carriers, whose mean is N_c), is given by

$$S_N(f) = 4\overline{\Delta N^2} \frac{\tau_o}{1 + 4\pi^2 f^2 \tau_o^2} \tag{2.12}$$

and the spectral density of the current fluctuation is

$$S_i(f) = i_e^2 S_N(f) = 4\, i_e^2 \overline{\Delta N^2} \frac{\tau_o}{1 + 4\pi^2 f^2 \tau_o^2} = 4\, \bar{i}^2 \frac{\overline{\Delta N^2}}{N_c^2} \frac{\tau_o}{1 + 4\pi^2 f^2 \tau_o^2} \tag{2.13}$$

where $i = Ni_e$ is the total instantaneous current and

$$\bar{I} = N_c i_e = \frac{N_c e}{\tau_d} \tag{2.14}$$

is the total average current.

For the MQW infrared detector , which is a majority carrier device, it can be shown [20] that the variance $\overline{\Delta N^2}$ is equal to N_c , the average number of conduction electrons, which is also the total number of carriers excited, either by the signal or by some other mechanism.

This is also the situation in impurity photoconductors when the conduction electrons can readily find empty donor levels at which they can recombine. For this cases we then have

$$S_i(f) = \frac{4\,\bar{I}^2}{N_c}\,\frac{\tau_o}{1+4\pi^2 f^2 \tau_o^2} = \frac{4\,e\bar{I}\left(\frac{\tau_o}{\tau_d}\right)}{1+4\pi^2 f^2 \tau_o^2} \tag{2.15}$$

Therefore the mean-square noise current attendant upon an average current $\bar{I}$ in a frequency interval f to $f+\Delta f$ is

$$\overline{i_n^2} = \frac{4\,e\bar{I}\left(\frac{\tau_o}{\tau_d}\right)\Delta f}{1+4\pi^2 f^2 \tau_o^2} \tag{2.16}$$

which, for $f\tau_o \ll 1$ reduces to

$$\overline{i_n^2} = 4\, e\bar{I}\left(\frac{\tau_o}{\tau_d}\right)\Delta f \tag{2.17}$$

(This expression is reminiscent of shot noise in photoemission, for example, but for the multiplicative factor $2\tau_0 / \tau_d$; the numerical factor $x2$ comes from the fact that both generation and recombination processes are involved, each displaying its own shot noise, while the lifetime to drift-time ratio reflects the fact that on the average the electrons drift but a fraction τ_0 / τ_d of the distance l.)

We are interested in understanding the physical limits on MQW detector performances and in comparing those to other materials, especially the HgCdTe system.

The spectral density of the current fluctuations in the case of a two-carrier (electrons and holes) semiconductor is given by [21]

$$S_i(f) = 4\, \bar{I}^2 \left[\frac{(b+1)}{bN+P}\right]^2 \frac{\overline{\Delta N^2}\,\tau_o}{1 + 4\pi^2 f^2 \tau_o^2} \tag{2.18}$$

where b is the ratio of the electron mobility to the hole mobility, N and P are the average numbers of electrons and holes respectively and τ_0 is the recombination lifetime.

Generally, for the wavelength region of interest, 8-12 µm, HgCdTe detectors are either n or p type doped. As such, the dark conductivity is determined by an excess of donors or acceptors. However, the impurity levels are fully ionized at the temperatures of operation and carriers cannot recombine into them; thus, all recombinations take place between the valence and the conduction band, i.e., are electron-hole recombinations. Due to this feature, HgCdTe not only acts as an intrinsic photoconductor, where excitation of carriers at the desired wavelengths occur through electron-hole generation, but also its statistics for carrier fluctuation is dominated by the number of minority carriers. It can be shown that the variance appearing in the current spectral density formula above is given under these assumption by [22]

$$\overline{\Delta N^2} = \frac{NP}{N+P} \approx P \qquad (\,for\ N >> P\ ) \tag{2.19}$$

i.e., the fluctuation in the majority carrier population N is determined by the minority population P. In HgCdTe, $b >> 1$; also for an n-doped sample $N >> P$. The spectral density of the current fluctuation, when $f\tau_0 << 1$, is given by

$$S_i(f) = \frac{4\bar{I}^2 P\tau_0}{N^2} = \frac{4e\bar{I}P\left(\frac{\tau_0}{\tau_d}\right)}{N} = 4e\overline{I_p}\left(\frac{\tau_0}{\tau_d}\right) \tag{2.20}$$

where $\overline{I_p} = eP/\tau_d$.

2.4 Background-limited and thermally-limited detection

In this section we calculate the limiting performance, due to basic physical constraints of MQW infrared detectors; later we will compare it to the limiting performance of a single HgCdTe detector.

Consider the photoconductive detector shown in Figure 2.2. The radiation to be detected is incident on the effective area A, and, for the case of an intersubband detector, let us assume that the correct geometry for the selection rules does apply. The thickness of the detector, or the superlattice length, is l. The optical signal input to the detector is P_s, and ν is the optical frequency of the signal, corresponding to wavelengths, say, around 8-12 µm. The incident power gives rise, as in (2.4), to a signal current

$$i_s = \frac{\eta P_s e}{h\nu}\left(\frac{\tau_o}{\tau_d}\right) \tag{2.21}$$

In addition to the signal current, we have two major sources of noise currents that are not related to the signal. The first is the generation-recombination noise associated with the drift, under the influence of the applied external field, of thermally excited carriers, while the second is the generation-recombination noise due to carriers excited by the ever-present incoming background optical radiation. Accordingly , and

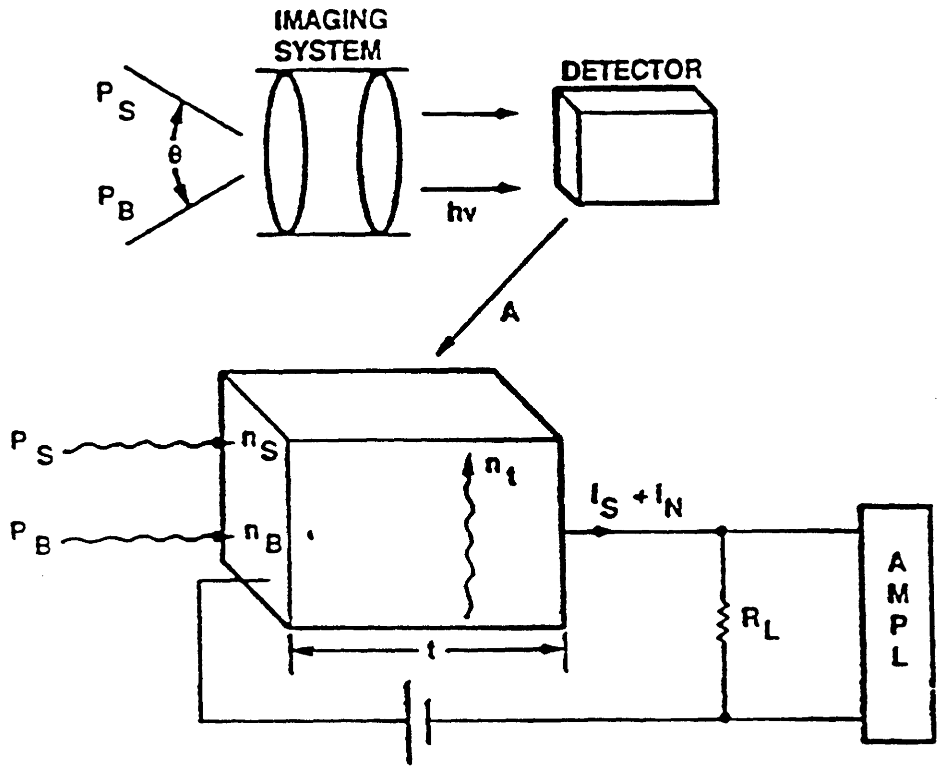

Figure 2.2. A schematic view of the imaging system, the photoconductor and the biasing circuit. The incident radiation is collected at an angle of view θ. The incident power includes the signal P_s and the ever present background radiation P_b. In the detector of area A, three different populations of excited carriers are present: n_s is the density of excited carriers due to the signal, n_b is the one due to the background radiation, and n_t is the density of electrons due to thermal excitation. The current monitored through a load resistor and transferred to the amplifying stages will accordingly include a signal component and a noise component.

as depicted in Fig. 2.2, we can distinguish three populations of carriers, quantified by the following three densities (cm^{-3}): n_s due to the signal, n_t due to the thermal excitation and n_b due to the incoming background radiation.

When P_s, $= 0$, an average noise current

$$\bar{I}_n = \left(n_t + n_b\right) e v \tag{2.22}$$

is generated where, as before, v is the drift velocity. Associated with this flow is a generation recombination noise (eqs. 2.16, 2.17)

$$\overline{i_n^{\,2}} = 4\, e\bar{I}_n \left(\frac{\tau_o}{\tau_d}\right) \Delta f \tag{2.23}$$

where Δf is the bandwidth of the (electronic) detection circuit.

The density n_b of carriers excited by the background radiation can be calculated, as seen above, by considering the steady state in which the rate of photon absorption per unit volume is equal to the rate of carrier retrapping by the quantum wells

$$n_b = \frac{\left(P_b / A\right) \eta \tau_o}{h v l} \tag{2.24}$$

η is the fraction of the incident background power P_b, (Watts) which gives rise to photoelectrons. This power, in many occasions, is that of the background blackbody radiation incident on the effective cross sectional area A of the detector, and is thus given by

$$P_b = \frac{2\pi h\, \nu^3 \Delta\nu A \sin^2(\theta/2)}{c^2\left(e^{h\nu/K_B T_b} - 1\right)} \tag{2.25}$$

where $\Delta\nu$ is the optical bandwidth around the optical frequency ν allowed into the detector. (For a real detector sensitive to a finite bandwith B, one has to integrate the expression over B, or make use of useful integrating blackbody tables). T_b is the background temperature, while θ is the cone angle subtended by the radiation accepted by the detector. In many cases T_b and θ are dictated by the application. A reasonable strategy in such a case is to cool the the detector to the point where $n_t < n_b$. Additional cooling will not significantly improve the signal-to-noise ratio at the output. Whenever this condition has been reached, the signal-to-noise ratio is determined by the background radiation and the detector displays a background limited infrared performance (BLIP).

2.4.1 Background-limited detection

Assuming a BLIP operation of a MQW detector, we can calculate the resulting figures of merits for the detector performance. The mean-squared output noise current, in the limit $f\tau_0 << 1$, is

$$\left(\overline{i_n^2}\right)_{BLIP} \equiv \overline{i_{n,B}^2} = 4e\overline{I_b}\left(\frac{\tau_o}{\tau_d}\right)\Delta f \tag{2.26}$$

Notice that, as seen when we dealt with different photoconductor statistics, n_b is the density of electrons excited, at steady state, by the background radiation above the barrier level, in the MQW detector. For an HgCdTe detector operating at a BLIP condition, n_b is the density of minority carriers excited by the background radiation (e.g., holes in an n-doped device). Substituting for n_b from Eq. 2.24, we obtain

$$\overline{i_{n,B}^2} = \frac{4e^2P_b\eta}{h\nu}\left(\frac{\tau_o}{\tau_d}\right)^2\Delta f \tag{2.27}$$

The most commonly used figures of merit for detectors include the minimum detectable signal, also called the noise equivalent power (NEP) of the detector. The NEP is defined as the value of the signal power P_s, which results in a signal output power equal to the noise power, i.e.,

$$\overline{i_s^2} = \overline{i_n^2} \tag{2.28}$$

Substituting for the two squared currents and solving for P_s, we get for the minimum detectable power, in the BLIP condition $n_t < n_b$

$$(NEP)_B = P_s\left(\overline{i_s^2} = \overline{i_{n,B}^2}\right) = 2\sqrt{\frac{P_b h\nu\Delta f}{\eta}} \tag{2.29}$$

Another widely used figure of merit for detector sensitivity is the specific peak detectivity D^* defined as

$$D^* = \frac{\sqrt{A\,\Delta f}}{NEP} \tag{2.30}$$

Again for a BLIP situation, the value of the detectivity is

$$D_B^* = \frac{1}{2}\sqrt{\frac{\eta}{h\nu\left(P_b/A\right)}} \tag{2.31}$$

which depends only on on the incoming photon flux, the optical frequency and the quantum efficiency of the detector. It is also clear, from the definitions, that alternative ways of stating the BLIP condition $n_t < n_b$ are

$$(NEP)_t < (NEP)_b \qquad and \qquad D^*_t > D^*_b. \tag{2.32}$$

2.4.2 Thermally-limited detection

In the thermal limit $n_b << n_t$ the performance of the detector is limited by the generation-recombination noise of thermally excited carriers, i.e., for the MQW detector, of those mobile electrons which populate the higher continuum states above the well at the temperature of operation. The average current due to n_t is

$$\overline{I_t} = n_t evA \tag{2.33}$$

corresponding to a mean-square noise

$$\overline{i_{n,t}^2} = 4e\overline{I_t}\left(\frac{\tau_o}{\tau_d}\right)\Delta f \tag{2.34}$$

Equating, as before, $\overline{i_n^2}$ to $\overline{i_s^2}$ and solving for P_s, we obtain the noise equivalent power in the thermal limit

$$(NEP)_t = \frac{2h\nu}{\eta}\sqrt{n_t vA\,\Delta f\left(\frac{\tau_d}{\tau_o}\right)} \tag{2.35}$$

And similarly, for the specific peak detectivity

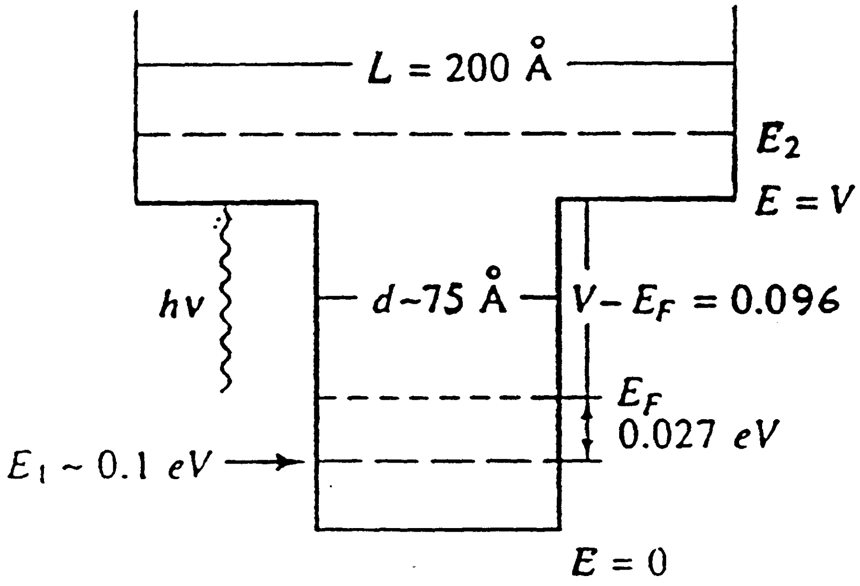

Figure 2.3. Schematic illustration of a typical quantum well detector through a spatially resolved representation of the energy levels in the conduction band of the heterostructure. The energies are usually referred to the bottom of the well, i.e., to the conduction band edge of GaAs. The barriers are made of AlGaAs. The subband levels are given by E_1 and E_2. The second subband is above the level of the barrier, into the continuum. The detector is thus of the bound-to-continuum type.

$$D_t^* \equiv \frac{\sqrt{A\,\Delta f}}{(NEP)_t} = \frac{\eta}{2h\nu}\sqrt{\frac{1}{n_t v}\left(\frac{\tau_o}{\tau_d}\right)} = \frac{\eta}{2h\nu}\sqrt{\frac{\tau_o}{n_t\, l}} \tag{2.36}$$

To obtain an expression for the density n_t of electrons excited to the continuum above the well, we use the model of Fig. 2.3 in which we approximate the continuum states as those of a wide quantum well of width L equal to the mean well spacing. The two-dimensional density of states is then (assuming that only one state, n=1, is confined in the deep well) [19]

$$\rho_{2D}(E) = \frac{m^*}{\pi h^2}\left(1 + Int\left[\sqrt{\frac{2m^*(E-V)}{h^2\pi^2/L^2}}\right]\right) \qquad (cm^{-2}eV^{-1}) \tag{2.37}$$

where *Int(x) = largest integer < x.* The corresponding volumetric density of states (electrons/cm^3-eV) is ρ_{2D}/L. As expected,when

$$\sqrt{\frac{2m^*(E-V)}{\hbar^2\pi^2/L^2}} >> 1 \tag{2.38}$$

the volumetric density tends to the bulk 3-D density of states

$$\frac{\rho_{2D}}{L} \rightarrow \frac{1}{2\pi^2}\left(\frac{2m^*}{\hbar^2}\right)^{3/2}(E-V)^{1/2} \tag{2.39}$$

The volume density of free carriers (electrons/cm^3) is given by the product of the volumetric density and the Fermi occupation function

$$n_t = \frac{m^*}{\pi\hbar^2 L}\int_V^\infty \left(1 + Int\left[\sqrt{\frac{2m^*(E-V)}{\pi^2\hbar^2/L^2}}\right]\right)\frac{dE}{e^{(E-E_F)/K_BT}+1} \approx \tag{2.40}$$

$$\approx \frac{m^* e^{-(V-E_F)/K_BT}}{\pi\hbar^2 L}\int_0^\infty \left(1 + Int\left[\sqrt{\frac{2m^*u}{\pi^2\hbar^2/L^2}}\right]\right)e^{-u/K_BT}du \tag{2.41}$$

where E_F is the Fermi energy.

When $(h^2/m^*\pi^2L^2) > K_BT$, we can neglegt the *In [.]* term in the integral, which represents higher lying subbands, since most of the thermal carriers come from the first electron subband of the quantum well. In this case

$$n_t \approx \frac{m^* K_B T}{\pi\hbar^2 L} e^{-(V-E_F)/K_BT} \tag{2.42}$$

which slightly underestimates n_t . The Fermi level can be calculated to various degrees of accuracy. We can get a good approximation by assuming an infinite potential; in this limit we have

$$E_F = \frac{n_0 \pi\hbar^2 d}{m^*} \tag{2.43}$$

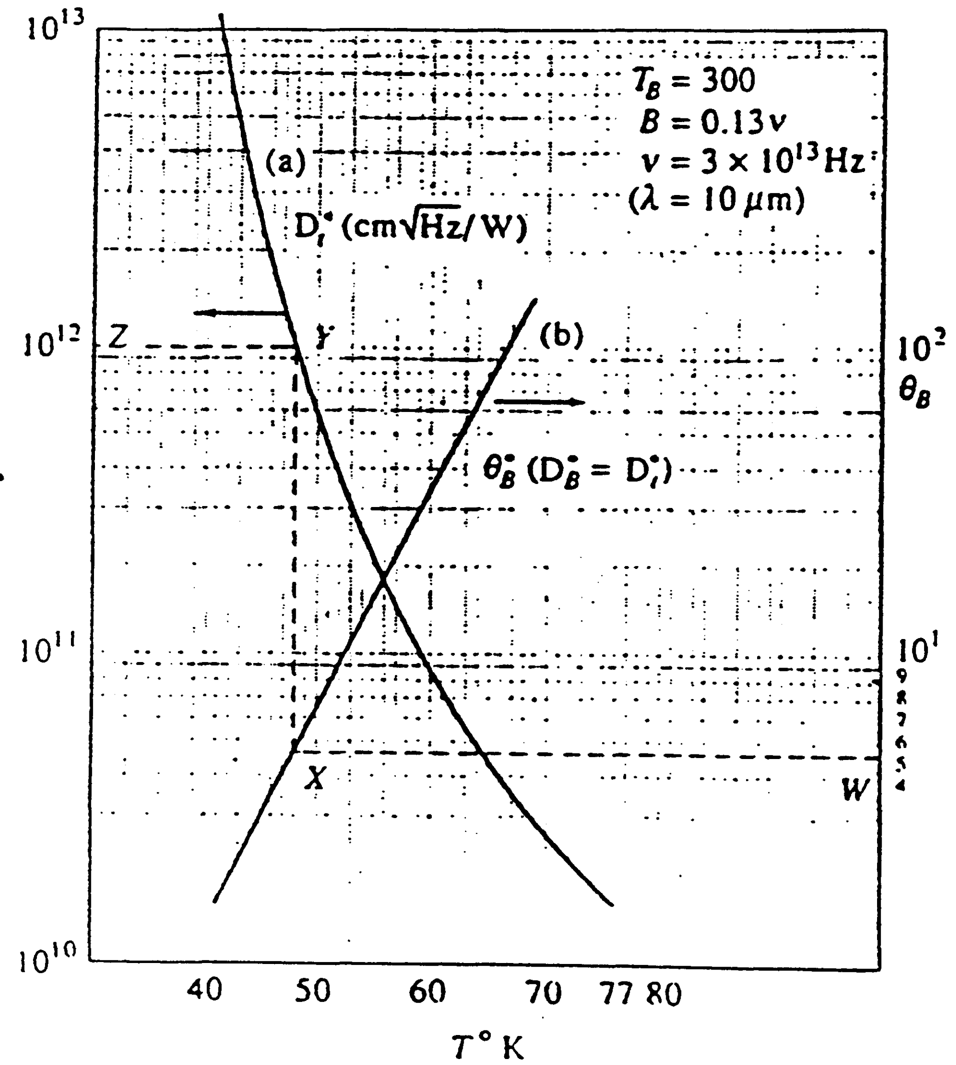

Figure 2.4. Curve (a) is a plot of the thermally limited detectivity D_t^* at 10 μm versus temperature of the GaAs quantum well detector described in Figure 2.3. Curve (b) is a plot of the acceptance angle θ_b which results in $D_b^* = D_t^*$ (BLIP) for the background conditions stated in the figure.

In Figure 2.4 we show the calculated thermally limited detectivity D^* vs. the detector temperature for the parameters of Fig.ure 2.3, and $m^* = 0.067m_e$, , $\tau_0 / \tau_d = 0.5$, $\lambda = 10\mu m$ and $v = 3x10^7 cm/s$. .

To use this curve we need first to obtain a value for D_b^* based on the background flux in the given application. We then find the temperature in Figure 4(a), where $D_t^* = D_b^*$. As an example, given $D_b^* = 10^{12}$ we can see from Figure 4(a) that the MQW detector needs to be cooled to $T < 48^0 K$ in order to become background limited. Figure 4(b) is a plot of the acceptance angle θ_b for which D_b^* is equal to D_t^* , assuming a black-body $300^0 K$ background. Further increase of θ_b will thus cause the detector to be background limited. Figure 4(b) uses a background temperature $T_b = 300^0 K$, $\nu = 3x10^{13}$ (= $10\mu m$), $B = 0.13\nu$. As an example, if a detector has $D_t^* = 10^{12}$, then the BLIP condition is obtained for $\theta_b = 4.6^0$. We can also use the curve of Figure 4(b) in the opposite direction to find D_b^* for a given θ_b. For instance, for $\theta_b = 4.6^0$ we follow the sequence W→X→Y→Z to find $D_b^* = 10^{12}$; in the process we also learn that the detector temperature must be below $48^0 K$ in order to be background limited.

2.4.3 Comparison with the HgCdTe system

The most widely used material for infrared imaging near $\lambda = 10\mu m$, is the semiconductor HgCdTe, (MCT) whose composition can be adjusted to yield a bandgap corresponding to a photon with energies in the mid infrared. The photoconduction in this case is due to excitations from the valence band to the conduction band. Let us assume, a typical n-type material; as discussed above, the number of excited minority carriers, in this case holes, is the important parameter determining the signal and the noise. Our theoretical discussion up to this point applies if we take n_b, n_t and n_s, respectively as the density of holes excited by the background radiation, thermal processes and the signal radiation. One is forever striving, in this business, to find materials that enable backgound-limited performance at the highest possible temperature, an important mark being liquid nitrogen temperature. The background limit condition $n_b = n_t$ can be written as

$$\frac{(P_b/A)\eta\tau_o}{h\nu l} = n_t \tag{2.44}$$

Since n_t invariably increases with T, it follows that the temperature for background-limited operation increases with the carrier lifetime τ_0. In MQW intersubband detectors the order of magnitude at $T=77^0K$ is $\tau_0 \sim 10^{-11}\,s$ corresponding to the time for an excited electron to be retrapped by a well. (This generally happens after the emission of only a few optical-branch phonons by the excited carrier). In typical "good" MCT detectors the carrier lifetime can be as long as $\tau_0 \sim 10^{-6}\,s$. These order-of-magnitude considerations indicate that an HgCdTe detector is background-limited at a higher temperature than a GaAs intersubband detector. We can quantify this result by calculating the thermal generation current, that is, the rate (per unit of incidence area) of thermal excitation of carriers; since this rate is equal, at thermal equilibrium, to the rate at which "thermal" carriers recombine, it is given by

$$I_{tg} = \frac{n_t l}{\tau_o} \qquad \left[photons / \left(cm^2 s\right)\right] \tag{2.45}$$

Notice that exactly at the background limit (BLIP), I_{tg} is equal to the rate of absorbed background photons (per unit area) incident on the detector. Since the latter is generally determined by system considerations, given the background absorbed flux $\eta P_b/h\nu A$ we can determine at a glance, from a plo tof I_{tg} vs T, the temperature to which our detector needs to be cooled to achieve BLIP condition. We calculate the thermal generation current for the quantum well detector whose subband structure, together with other relevant parameters, are shown in Figure 5. (This structure was used by Levine et al. [9] The well width is taken to be $d=4nm$, the height of the AlGaAs potential barrier is $V=250meV$, the superlattice period is $L=34nm$, the doping level in the wells is $n_o = 2x10^{18}cm^{-3}$, the effective mass is taken to be $m^* = 0.067m_o$ and the length of the device is $l = 1.7\mu m$. Using a "typical" value for the lifetime $\tau_o = 8.5ps$. We calculate $E_f = 28.7meV$. This design yields a peak wavelength of $8.3\mu m$. By changing the width of the well to $d = 30Å$, we obtain a detector with peak at $10\mu m$.

In both cases we can use the approximated result of Eq. (2.42)

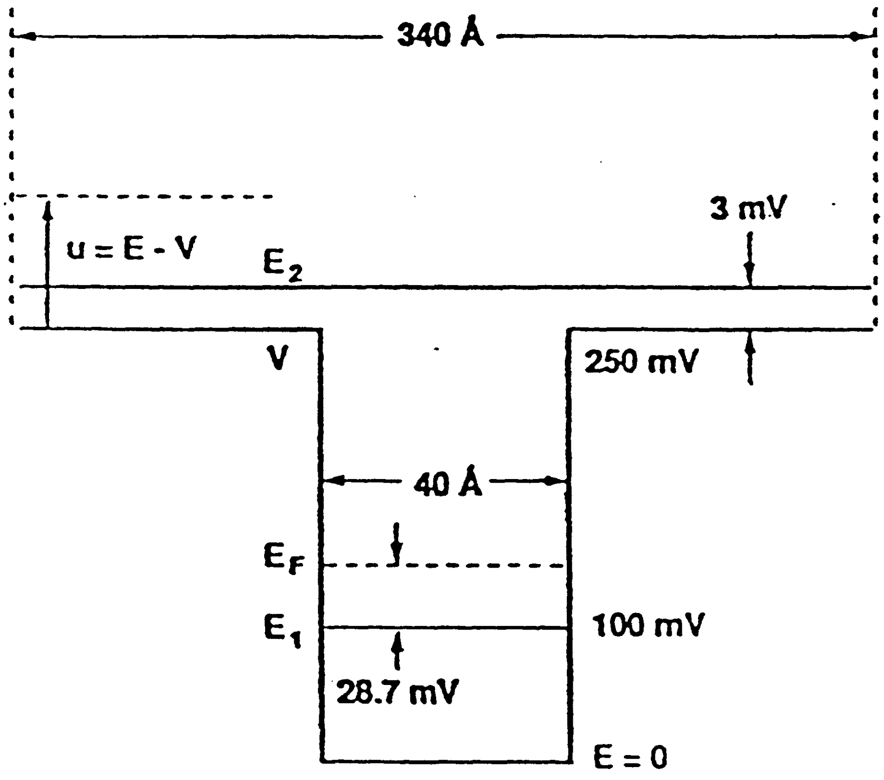

Figure 2.5. Quantum well infrared detector designed for 8.3 µm. By changing the well width to 30 Å, the center wavelength for which the detector is designed shifts to 10.0 µm. This configuration and the modified one are used for the calculations done to compare between the expected performances of a multi-quantum well GaAs/AlGaAs detector and a HgCdTe infrared detector, for both the 8µm and 10 µm range.

$$n_t \approx \frac{m^* K_B T}{\pi \hbar^2 L} e^{-(V-E_F)/K_B T} \approx n_o \left(\frac{K_B T}{E_F} \right) \frac{d}{L} e^{-(V-E_F)/K_B T} \tag{2.46}$$

This last result is used in Eq. (2.45) to calculate the thermal generation current in two MCT detectors with cutoff wavelengths of $8.3 \mu m$ and $10 \mu m$. In good quality material, the minority-carrier lifetime τ_p is limited by Auger recombination and is given by

$$\tau_o = \tau_p = 2\tau_{Ai} \frac{n_i^2}{n_o^2} \tag{2.47}$$

where τ_{Ai} is the intrinsic Auger lifetime. τ_{Ai} has been measured [23] for a variety of HgCdTe compositions, is in reasonable agreement with theory [24] and is given by

$$\tau_{Ai} = \left[\frac{8.3x10^{-13} E_g^{1/2}}{\left(K_B T\right)^{3/2}} \right] e^{E_g / K_B T} \tag{2.48}$$

For MCT, as discussed above,

$$I_{tg} = \frac{p_n l}{\tau_p} \tag{2.49}$$

our Eqs. (2.47) and (2.48), where p_n is the thermal minority (hole) density, and recalling that

$$p_n = \frac{n_i^2}{n_o} \tag{2.50}$$

we find for the thermal generation current

$$I_{tg} = \frac{p_n l}{\tau_p} = \frac{n_o l}{2\tau_{Ai}} \tag{2.51}$$

Using a typical value of $n_n = 10^{15} cm^{-3}$ for the doping density, and Eq. (2.48) for τ_{Ai}, we calculate I_{tg} for the two MCT detectors with cutoff at $8.3 \mu m$ and $10 \mu m$ respectively.

The results, for both kinds of detectors, are displayed in Figure 2.6. Typical quantum efficiencies have been assumed to normalize the thermal current axis; for the GaAs MQW detectors $\eta = 0.175/\sqrt{2} = 0.125$ was used, and for HgCdTe we took $\eta = 0.7$. The plots show that the thermal generation rate at any specific temperature and cutoff is approximately five orders of magnitude smaller for the MCT detector than for the GaAs MQW detector. This translates into a cooling requirement of up to an additional 50^0K for the intersubband detector to achieve the same performance as HgCdTe. Comparing the detectors on the basis of peak detectivities, at 80^0K the two superlattices considered here would exhibit maximum values of $D^*_\lambda(8.3 \mu m) = 1.85x10^{10}\ cm\ Hz^{1/2} W^{-1}$ and $D^*_\lambda(10 \mu m) = 6.15x10^9\ cm\ Hz^{1/2} W^{-1}$, while for the HgCdTe detectors we would have $D^*_\lambda(8.3 \mu m) = 1.75x10^{13}\ cm\ Hz^{1/2} W^{-}$ and $D^*_\lambda(10 \mu m) = 3x10^{12}\ cm\ Hz^{1/2} W^{-1}$. This agrees with the qualitative discussion.

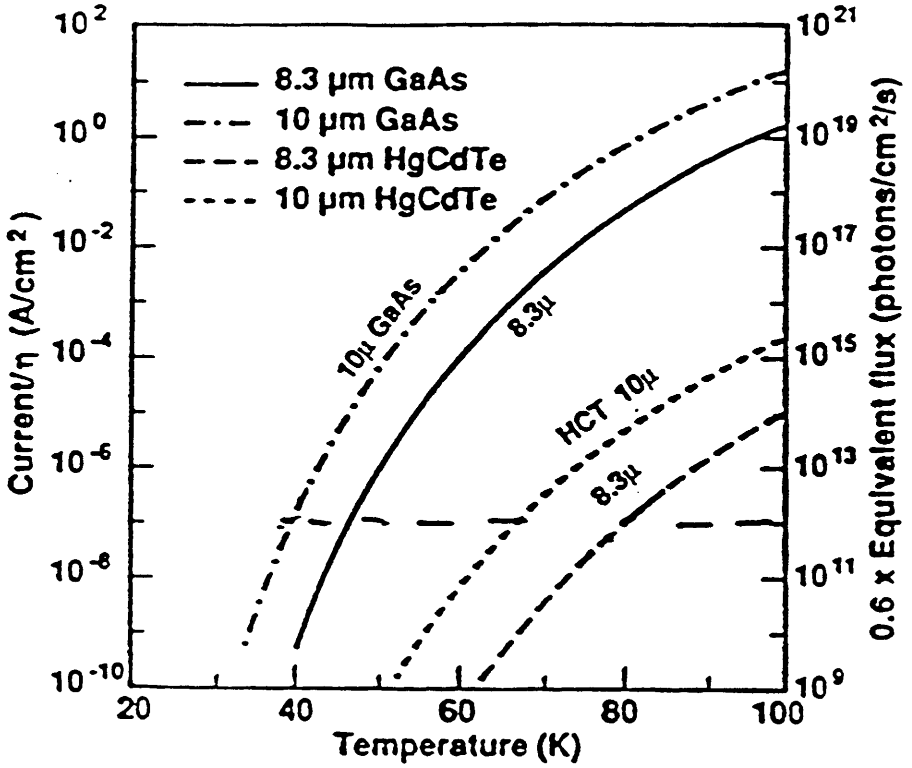

Figure 2.6. Thermal generation current versus temperature for GaAs/AlGaAs infrared superlattices and HgCdTe alloys at λ = 8.3 and 10.0 µm. The assumed quantum efficiencies are η = 0.125 and 0.7 for GaAs/AlgaAs and HgCdTe, respectively.

A few comments are appropriate at this point. It should be pointed out that the GaAs/AlGaAs MQW detectors considered above are not theoretically optimized structures. On the other hand we have neglected in our model the contribution to the dark current arising from tunneling or even photon assisted tunneling, assuming that in real design these can be reduced by using wide barriers. Some benefits toward improving the intersubband detectors could come instead from quantum efficiency improvements, or by a careful trading off device thickness and doping concentrations such that a high overall quantum efficiency is maintained together with a decrease in E_f and hence n_t one can think that widening the barriers, beyond taking care of the tunneling currents, could bring in some enhancement in carrier lifetime, but there are limits to this too, since by enlarging L the contributions of higher subbands to n_t become more important, contrary to the assumptions in our calculations here, so that an increase in τ_0 would be offset by an increase in n_t . The complete picture about devices designed to offer a large photoconductive gain has not yet been studied; in this case the lifetime is not limited by sweep-off and time of flight up to the contacts. However, the lifetime will still be limited by the basic relaxation mechanisms for intersubband transitions and the ratio of well widths to barrier widths; moreover, at least in simple direct schemes for photonductive gain, it is apparent that this can enhance the responsivity but not the signal-to-noise, under BLIP conditions, since also every "noise" electron is subject to the same photoconductive gain.

2.5 Conclusions

We considered above the basic limits on detectivities of quantum well infrared detectors based on intersubband transitions. We compared them to interband MCT detectors and showed that the latter possess considerably higher inherent detectivities (at liquid N_2 temperature), due to longer carrier lifetimes. The quantum well detectors in III-V materials, however, still possess useful detectivities which, coupled with real world considerations of uniformity across a wafer, ease of processing and cost, may make them the detectors of choice in many a practical situation.

References

[1] J.S. Smith, L.C. Chiu, S. Margalit, A. Yariv and A.Y. Cho, J. Vac. Sci. Technol. B1, 376 (1983)

[2] B.F. Levine, G. Hasnain, C.G. Bethea, N. Chand, Appl. Phys. Lett. 54, 2704 (1989).

[3] K.W. Goossen and S.A. Lyon, J. Appl. Phys. 63, 5149 (1988).

[4] G. Hasnain, B.F. Levine, C.G. Bethea, R.A. Logan, J. Walker, and R.J. Malik, Appl. Phys. Lett. 54, 2515 (1989).

[5] G. Hasnain, B.F. Levine, S. Gunapala, and N. Chand, Appl. Phys. Lett. 57, 608 (1990).

[6] S.R. Parihar, S.A. Lyon, M. Santos and M. Shayegan, Appl. Phys. Lett. 55, 2417, (1989).

[7] B.F. Levine, C.G. Bethea, V.O. Shen, R.J. Malik, Appl. Phys. Lett. 57, 383 (1990).

[8] I. Gravé, A. Shakouri, N. Kuze and A. Yariv, Appl. Phys. Lett. 60, 2362 (1992).

[9] B.F. Levine, C.G. Bethea, G. Hasnain, J. Walker, and R.J. Malik, Appl. Phys. Lett. 53, 296 (1988).

[10] B.K. Janousek, M.J. Daugherty, M.L. Bloss, M.L. Rosenbluth, M.J. O'Loughlin, H. Kanter, F.J. De Luccia, and L.E. Perry, J. Appl. Phys. 67, 7608 (1990).

[11] B.F. Levine, C.G. Bethea, G. Hasnain, V.O. Shen, E. Pelve, R.R. Abbott, S.J. Hsieh, Appl. Phys. Lett. 56, 851 (1990).

[12] A. Zussman, B.F. Levine, J.M. Kuo, and J. de Jong, J. Appl. Phys. 70, 5101 (1991).

[13] H. Schneider, F. Fuchs, B. Dischler, J.D. Ralston, and P. Koidl, Appl. Phys. Lett. 58, 2234 (1991).

[14] S.I. Borenstain, I. Gravé, A. Larsson, D.H. Rich, B. Jonsson, I. Andersson, J. Westin, T. Andersson, Phys. Rev. B 43, 9320 (1991).

[15] S.D. Gunapala, B.F. Levine, R.A. Logan, T. Tanbun-Ek, and D.A. Humphrey, Appl. Phys. Lett. 57, 1802 (1990).

[16] S.D. Gunapala, B.F. Levine, D. Ritter, R. Hamm, and M.B. Panish, Appl. Phys. Lett. 58, 2024 (1991).

[17] M.A. Kinch and A. Yariv, Appl. Phys. Lett. 55, 2093 (1989).

[18] B.F. Levine, Appl. Phys. Lett. 56, 2354 (1990).

[19] I. Gravé and A. Yariv, "Fundamental Limits in Quantum Well Intersubband Detection," NATO ASI Series, Volume on Intersubband Transitions in Quantum Wells. Editors: Rosencher, Vinter and Levine (1992).

[20] A. Van Der Ziel, "Fluctuation Phenomena in Semiconductors, " Academic Press (1959).

[21] K.M. Van Vliet, Proc. Inst. Radio Engrs. 46, 1004 (1958).

[22] D. Long, Infr. Phys. 7, 169 (1967).

[23] .M.A. Kinch, M.J. Brau, A. Simmons, J. Appl. Phys. 44, 1649 (1973).

[24] P.E. Petersen, J. Appl. Phys. 41, 3465 (1970).

Chapter 3

Intersubband infrared detectors

3.1 Introduction

Having shown in the previous chapter that intersubband infrared detectors can achieve respectable performances which could make them the choice for many systems and applications, we now present in the first part of this chapter a brief description of the techniques involved in all stages of the design, material growth, preparation and characterization of detector samples. These form the package of technical knowledge and facilities that have been developed in order to complete the cycle, from conception and design, to device implementation. The second part of this chapter is devoted to present our experimental results on "standard" intersubband detectors. Chronologically, this part of the work was done during the first period of the research, when the main drive was to understand the effects of different factors on detector operation, in conjunction with the theoretical aspects presented in chapter 2; the final goal was optimizing performances. The experimental results disclose excellent figures of merit as for responsivities, dark current and detectivities.

3.2 Design and growth of detector samples

The principle of operation of a bound-to-continuum detector has been presented in chapters 1 and 2. One can design the detector to exhibit a center wavelength of choice by varying the structural parameters of the quantum well and of the barrier. For simple square wells, the design always includes a ground state subband and a second subband located close to the top of the well. More specifically the location of the second subband could be inside the well, just on top of it or outside the well, in the continuum above the barrier.

The two structural parameters which control the energy levels of the subband are the well width and the barrier height. Since there is always a few percent accuracy in calibrations and repeatability of MBE growth parameters (corresponding to fluctuations of one or two monolayers for uniformity during the deposition process), one has to push for accuracy of the design to about that limit. The simple model of a finite quantum well including band nonparabolicity, is good enough for most designs. There is a spread of values reported from calculations or measurements in the published literature for structural parameters such as the band offset and the nonparabolicity coefficients. By sticking to a definite value and incorporating feedbacks from actual growths and characterizations, one can achieve experimental results very close to the design needs and reasonable reproducibility.

Following is a review of the materials parameters and the model used for our design of intersubband samples [1-3].

The electron effective mass in the barrier is taken to be, in units of m_e,

$$m_b^* = m_w^* + 0.083\,x \tag{3.1}$$

where $m_w^* = 0.0665$ is the effective mass of an electron in the GaAs quantum well in units of m_e , the free electron mass. Band nonparabolicity is taken into account by using an energy dependent effective mass in the GaAs layers of the well [4]

$$m^*_{w,np}(E) = m_w + 0.0436\,E + 0.236\,E^2 - 0.147\,E^3 \quad \text{where E is in eV.} \tag{3.2}$$

In the valence band, the heavy hole and light hole masses are taken to be

$$m^*_{hh} = 0.5 \quad ; \quad m^*_{lh} = 0.082 \qquad \text{again, in units of } m_e. \tag{3.3}$$

The energy gap as a function of temperature, for GaAs is taken to be

$$E_{G,0} = 1.519 - \frac{5.405\text{x}10^{-4}T^2}{(204 + T\ )} \tag{3.4}$$

The energy gap for AlGaAs is

$$E_{G,x} = E_{G,0} + 1.425\,x - 0.9\,x^2 + 1.1\,x^3 \tag{3.5}$$

for a direct bandgap, i.e., for Al concentration $x \leq 0.42$. We used band offset values

$$\Delta E_c = 0.6\,(E_{G,x} - E_{G,0}) \;\; ; \;\; \Delta E_v = 0.4\,(E_{G,x} - E_{G,0}) \tag{3.6}$$

The refractive index of GaAs in the region of interest (8-12 μm) is in the range

$$13.1 \leq \varepsilon_r \leq 13.3 \tag{3.7}$$

and for AlGaAs it is given by

$$\varepsilon_{r,x} = \varepsilon_{r,0} - 3x \tag{3.8}$$

For bound-to-bound transitions generally it's enough to solve for the single quantum well case, under the assumption that the presence of long barriers (> 200 Å), as required to achieve low dark currents, completely decouples the wells one from the other in a multi-quantum well sample. For bound-to-continuum transitions, the calculation are slightly different, involving extended states [5]. Resonances in a transmission problem can be calculated; or some approximation, as the one used in chapter 2 can be employed (the levels in a larger well representing the continuum). As a general trend, the wider the well, the deeper inside it are the energy levels located, and the closer are they spread apart, for a given barrier height. The narrower the width, the higher the excited subband is pushed towards or into the continuum.

Samples used for the measurements of nonlinear optical properties usually are designed in the bound-to-bound scheme. Sometimes more than one excited subband are designed to be included within the well.

An additional important parameter is the doping technique and the doping level in the structure. Carriers have to be made available inside the quantum wells for the detection of incident infrared light. Various doping schemes can be used; among them, doping of the whole well, partial well doping and delta doping, have all been successfully tried for detector structures. Barrier doping or modulation doping has also been used for other types of samples.

The level of the doping is important both for detector structures and for nonlinear samples. For detection purposes, the responsivity or quantum efficiency increases with the doping, although the same happens for the dark current and the noise equivalent power [6]. The detectivity (defined in chapter 2), is much less influenced by the doping level. Especially for low background levels, as in space exploration and detection, a large responsivity is always preferred to a small one for comparable detectivity levels.

Also for samples prepared for nonlinear studies, the doping is a very important parameter. The carrier concentration appears as a direct multiplication factor in the formula for the higher order susceptibilities. Any linewidth reduction is also very important for nonlinear effects since an enhancement in T_2 (the dephasing time) generally results in a larger susceptibility in near-resonance configurations. [And recent results tend to indicate that doping schemes do have a strong impact on the linewidth of the transition.]

For heavily doped samples the most important shift in energy levels, with respect to the basic model, is the many-body exchange interaction. The effect strongly increases for longer wavelength transitions and of course for high concentration of electrons. To correct for this effect one has to renormalize the populated subband (in many situations it is just the ground state subband); this is done by introducing the exchange integral [7,8]

$$E_{exch} = -\frac{e^2}{2\varepsilon}\int_0^{K_f} \frac{d^2k'}{(2\pi)^2}\int dz \int dz' \frac{e^{-q|z-z'|}}{q}\left|\Phi_o(z')\right|^2 \left|\Phi_o(z)\right|^2 \tag{3.9}$$

where $q = \left|\vec{k} - \vec{k'}\right|$ and $k_F = (2\pi\rho_{2D})^{1/2}$.

Notice that when Φ_0 is strongly localized in the well, the important region of integration is around small $q|z - z'|$ and then the integrand is more easily treatable by retaining the first terms in a Taylor expansion of the exponential factor.

The MBE growth of intersubband devices is standardly performed at low substrate temperature (~ 580 - 630 C). The temperature of the substrate was found to be important in fine tuning the performances of such devices in terms of infrared absorption and quantum efficiency.

For devices involving transport, such as detectors, the quality of the growth is even more important. Defects in the barriers can affect the photoconductive gain, by augmenting the impurity scattering cross section and enhancing the probability of recapture of an excited electron by the wells. The result would be that each excited carrier, for a given applied voltage between the electrodes, would drift a smaller number of superlattice periods per excitation, thus reducing the responsivity or external quantum efficiency of the device. Deep defects or impurities in the barriers could also detrimentally affect the noise performances of such devices, through an enhancement of tunneling dark currents through impurity states in the barriers [9].

Generally, calibrations of rates of growth for GaAs and AlAs were performed routinely on MBE grown samples and analyzed with the help of scanning electron microscopy. In addition, RHEED calibrations were used at the beginning of selected growths to monitor eventual changes in growth rates. Doping or carrier concentration calibrations were obtained by Hall measurements and, sometimes, in addition, differential capacitance measurements.

We will not review here all the techniques for sample preparation, MBE growth and calibration of growth rates, since they have been amply described in the literature or in previous thesis in our group.

3.3 Characterization of detector samples

The GaAs/AlGaAs multi quantum well wafers grown by MBE were then characterized for electrical and optical properties. Consistent design together with the accuracy of our MBE calibration rates could then be checked with a few techniques. The most important and natural tool is infrared absorption spectroscopy. Additional techniques included low temperature photoluminescence (PL), visible and near infrared interband absorption and excitation spectroscopy (PLE). From these measurements we could get a check on some growth parameters, such as the barrier height; studying the interband transitions between the conduction band quantum well subbands to the valence quantum well subbands, we could get complementary information on the location and separation of the subbands in the conduction band well.

We will not present here results or examples of these complementary techniques and measurements; they are all well known experimental tools which have been the subject of extensive publications; instead let us proceed to describe the main tool, infrared absorption spectroscopy.

3.3.1 Absorption measurements

Our common and mostly used tool to characterize the wafers grown by MBE is infrared absorption spectroscopy. From the infrared absorption spectra one can immediately obtain the separation of the subbands involved in the transitions, and thus check if the design of the structural parameter plus the MBE growth itself were accurate enough. In addition, one can check the strength of the absorption, thus getting indication on the quality of the growth. This measurement is also useful in extracting some important parameters, such as the intersubband absorption coefficient and oscillator strengths [10].

The absorption rate $\alpha(\omega)$ is the rate at which light incident on the medium will decay exponentially with distance. This is related to the imaginary part of the susceptibility by

$$\alpha(\omega) = -k_o\chi''/n_o = (-2\pi/n_o\lambda_o)\,\chi'' \tag{3.10}$$

where n_o and λ_o are, respectively, the refractive index in the material and the free-space wavelength of the radiation. By using the Fermi Golden Rule for the calculation of transition rates under the application of a sinusoidal perturbation, representing the incident optical radiation, one can get for the absorption between subband i and j

$$\alpha_{ij}(\omega) = \frac{\pi e^2 \Delta\rho_{ij}^{(0)} f_{ij}}{2 m_e n \varepsilon_o c} \frac{\Gamma_{ij}/\pi}{(\omega_{ij}-\omega)^2+\Gamma_{ij}^2} \tag{3.11}$$

where $\Delta\rho_{ij}^{(0)}$ is the difference in the surface (2-D) density of carriers between the two subbands at thermal equilibrium, $\Gamma_{ij} = 1/T_{ij}$ is the inverse of the dephasing time, n_o is the refractive index of the material, ε_o the dielectric constant, c the speed of light and $\omega_{ij} = \hbar E_j - \hbar E_i$ is the resonant frequency for the transition. f_{ij} is the oscillator strength, defined as

$$f_{ij} = \frac{2m_e\omega_{ij}}{\hbar}\left|\langle i|z|j\rangle\right|^2 \tag{3.12}$$

Experimentally, a normal incidence top (or bottom) illumination scheme is not able to induce intersubband absorption, due to the dipole selection rules, which require the radiation to be polarized along the growth direction (z axis), as in Figure 1.1. The measurements are instead performed in one of four configurations, as shown in Figure 3.1. In the first geometry the sample is illuminated from the top (or the bottom) at Brewster's angle ($\theta=73^{\circ}$) [10]. This results in a one-pass measurement; by calculating the refractions involved, and by taking into account the selection rules, one can realize that only about 9% of the incident light is available for absorption. These measurements thus require a very sensitive apparatus and the signal-to-noise that can be achieved is usually not too good.

The second method uses a multipass waveguiding geometry [11]. The sample is lapped from both sides to 45° , (other angles are also possible), and is then illuminated from the side, perpendicularly to the lapped surface. The infrared light travels in a zig-zag pattern, bouncing back and forth from the top and bottom edges of the substrate. In this way, the more favorable angular geometry allows for half of the power of a polarized light beam to be available for absorption at each pass; the multipass scheme enhances the signal-to-noise ratio. This measurement has its own problems, such as unwanted loss at imperfect boundaries and a rich refractive pattern within the superlattice. However one can get absorption coefficients with a reasonable error bar (around 10%) without too many efforts. This multipass

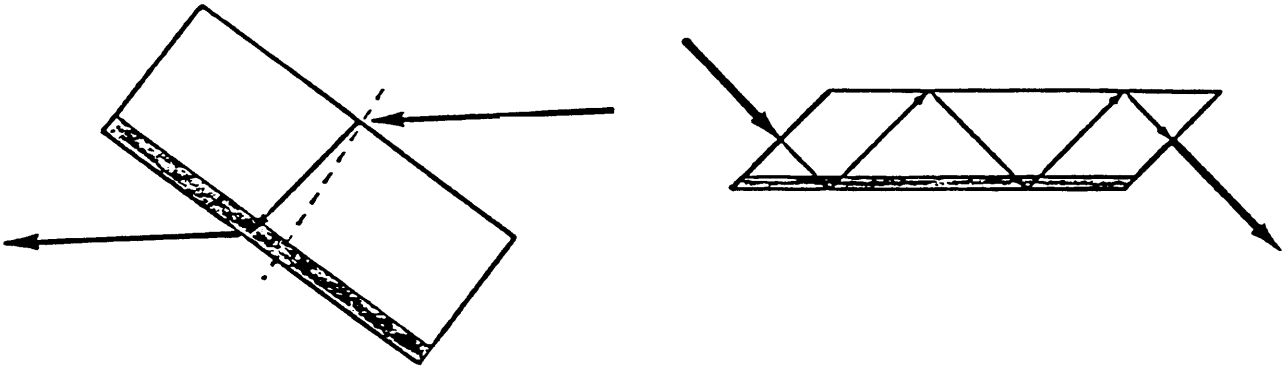

(a) Brewster's Angle

(b) Waveguide Mode

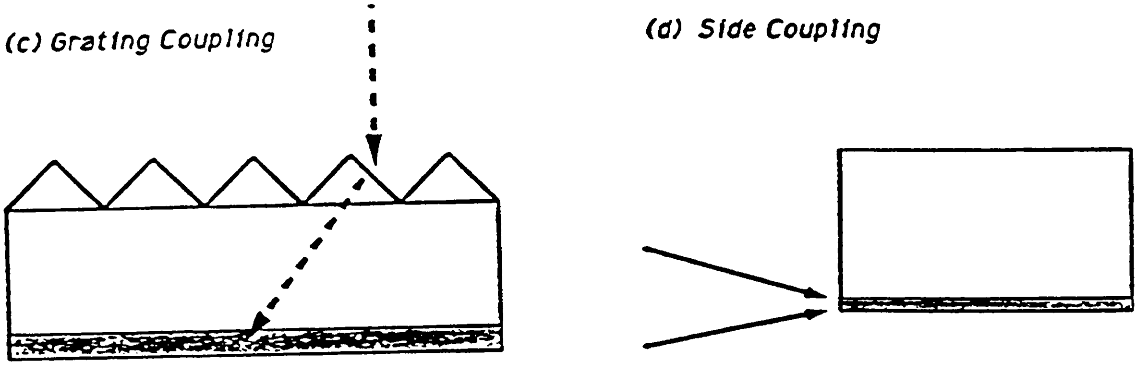

(c) Grating Coupling

(d) Side Coupling

Figure 3.1. Different geometries used to couple light to a multi-quantum well sample and to measure intersubband absorption.

waveguide geometry was the one used in most of our measurements.

A third technique is the one used for situations in which normal incidence from the top or bottom is strongly desired, in spite of the selection rules. Such is obviously the case for two-dimensional focal staring arrays. The method uses a diffraction grating on top or bottom of the wafer, to couple the incident light to the absorbing quantum well region at an efficient angle [12]. Performances of this coupling scheme have been shown to be very good [13], so that a basic deficiency of these detectors, deriving from the basic dipole selection rules, is readily bypassed with not too heavy a technologic effort.

Finally there is always the possibility of a side-entrance geometry, even though the wavelength around 10 μm is roughly five to ten times the thickness of the superlattice, and this means only part of the spatial extent of the beam will interact with the quantum well region.

The absorption data are generally presented in transmittance or absorption percentage or in absorbance units; the latter are dimensionless units, defined as:

$$A = -\log_{10}\frac{I_T}{I_o} \tag{3.13}$$

where I_o is the intensity of the beam incident on the sample, and I_T is the transmitted intensity.

In the multipass waveguide configuration the absorption coefficient is readily extracted from the absorbance units, using the relation:

$$\alpha_{(45^\circ)} = \frac{(\ln 10)\ A}{L_{MQW}} \tag{3.14}$$

where L_{MQW} is the total optical path in the multi-quantum well region.

Our absorption measurements were mostly performed using a Fourier Transform Infrared Spectrometer. Figure 3.2 schematically displays the Michelson Interferometer Optical System which is at the core of the operation of the spectrometer. The interferometer consists of two mirrors, an infrared light source, an infrared detector and a beamsplitter. The beamsplitter reflects about 50% of the incident light beam and transmits the remaining 50%. One part of the split light beam goes into the branch with the moving interferometer mirror, while the second part travels to the interferometer's stationary mirror. The reflection from both mirrors recombine at the beamsplitter. Here, half of the recombined light is transmitted to the detector while the other half is reflected towards the infrared source. When the two light beams recombine at the beamsplitter, an interference pattern is generated. This pattern varies with the displacement of the moving mirror along its axis, and is detected by the infrared detector as variation in infrared power. To scan from constructive to destructive interference for a specific wavelength, requires moving the scanning mirror one quarter of that particular wavelength. With a broad band infrared source, the resulting interferogram represents the sum of each cosine wave generated by each individual frequency component of the incident light. From the time domain interferogram, a Fourier transform is used to spectrally

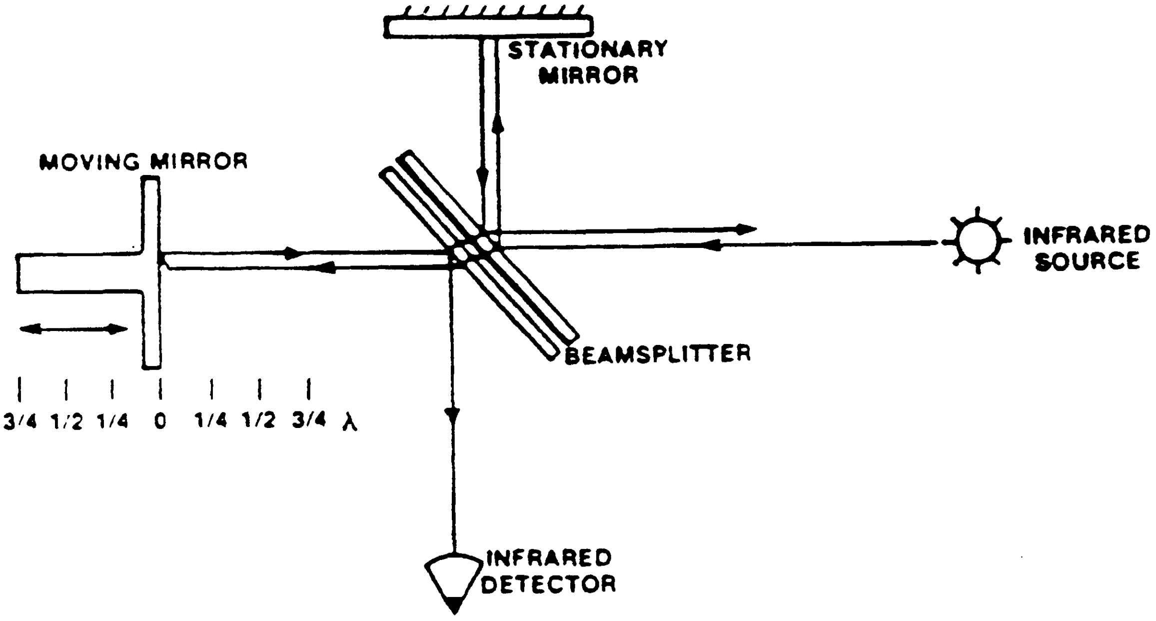

Figure 3.2. Michelson interferometer optical system at the core of an FTIR spectrometer. The beamsplitter reflects about 50% of an incident light beam and transmits the remaining 50% . One part of this split light beam travels to a moving interferometer mirror while the other part travels to the interferometer's stationary mirror. Both beams are reflected back to the the beamsplitter where they recombine. Half of the recombined light is transmitted to the detector.

resolve the intensity for each component in the frequency domain.

Measurements were taken at JPL, during the first period of our research; we used an old Mattson FTIR kindly made available to us. Subsequently, we purchased our own instrument from Mattson, model "Galaxy 2000," that includes a broadband, water-cooled black-body source , a 6X beam condenser and a number of detector options including a high D*, wide-band, Mercury-Cadmium-Telluride detector. A polarizer appropriate to the wavelength range of operation was also available. In this way transmittance spectral measurements were performed on the sample while the polarization was set perpendicular to the selection rules requirement, i.e., no intersubband absorption taking place. These data were stored and used as a calibrating or "background" measurement for the next run, in which the polarizer was set to have a strong component for the absorbing polarization. In this way, we could get a direct measure of the intersubband absorption, the results being already normalized to exclude eventual additional parasitic absorptions. These additional, small, unwanted absorption come from bulk GaAs absorption or from free electron absorption in the top and bottom contact layers, which are heavily doped. To a good approximation, these parasitic effects are polarization-independent. In addition, by measuring the absorption at different angles of polarization Φ , one can check the $\sin^2 \Phi$ dependence (for intensity), consistent with intersubband selection rules. An example of such a set of measurements is presented later on together with the experimental results on detector characterizations.

Examples of intersubband bound-to-bound and bound-to-continuum absorption graphs are shown in Figure 3.3 and Figure 3.4. Bound-to-bound transitions and bound-to-extended transitions reveal some subtle differences. Bound-to-bound transitions have a narrower linewidth and a Lorentzian shape [14]. Bound-to-extended spectra display a tail at higher energies [5,15]. Contrary to bound-to-bound or "pure" intersubband transitions, where the broadening is due to natural linewidth of two confined subbands, (and, in addition, to nonparabolicity [4], effective barrier height [5] and other smaller effects), bound-to-extended transitions involve a continuum of states on top of the barrier, all allowed, as long as they have the correct parity (in symmetric configurations). However, the higher energies these continuum states have, and the farther they are pushed into the continuum, the less localized they become, and the weaker the overlap integral with the ground state comes out to be. This is the reason for the tail at higher energies in the spectra; the whole picture is also consistent with the fact that, similar to many other quantum systems, these states have to obey oscillator strength sum rules.

Next let us show some experimental evidence of the subtle differences in the absorption spectra that can be obtained when the second subband is located deeper inside the well, or pushed higher towards the continuum.

Figure 3.3 displays the absorption spectra of two samples, obtained from the same growth; one was cut from the centerpiece of the wafer, the other from the edge of the wafer. Due to the different positions with respects to the material cells in the MBE growth chamber, well widths and barrier heights (or Al content) are slightly different for the two samples, differences being of the order of one monolayer deposition. The

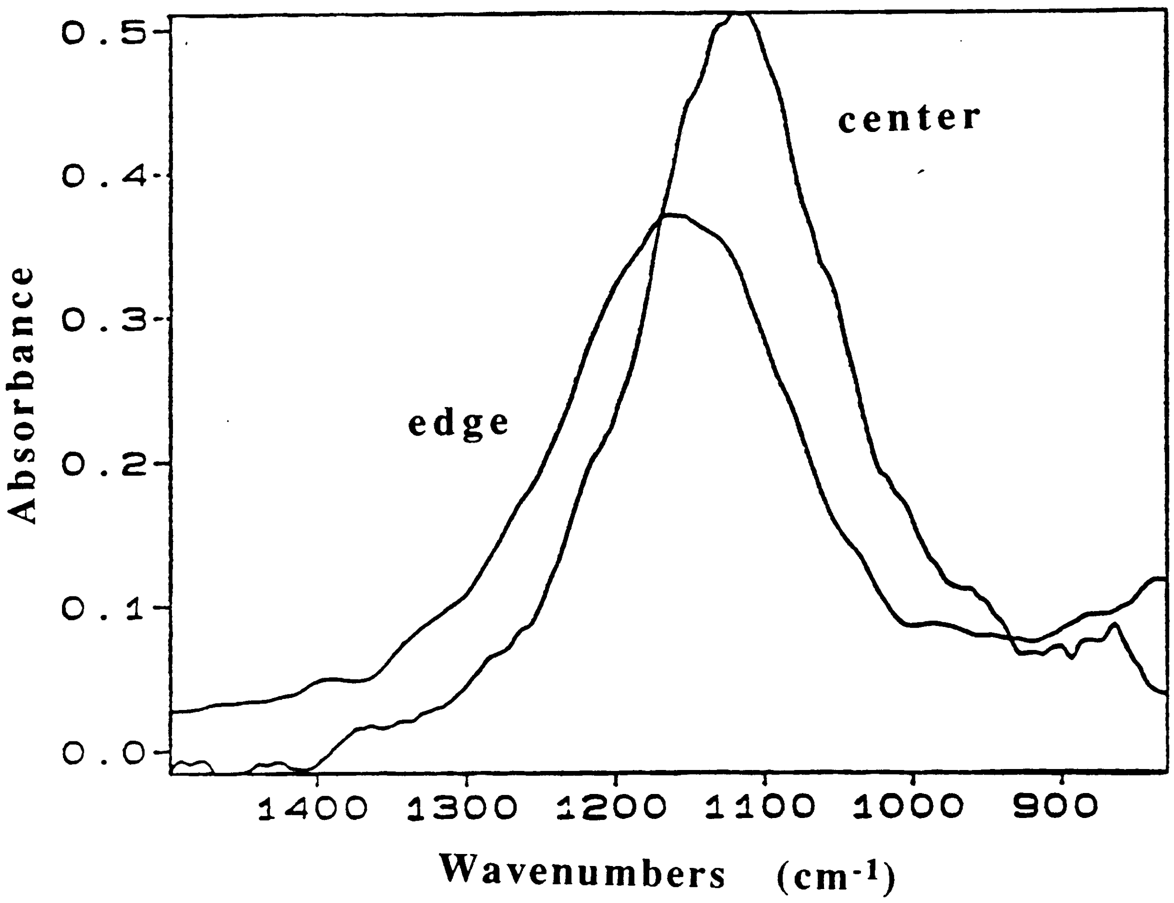

Figure 3.3. Absorption measurements performed on two samples cut out of the same wafer, one in the central part of the growth, the other toward the edge of the wafer. The growth was designed in such a way that at the center of the wafer the second subband was just inside the well, so that the absorption has a bound-to - bound character. Due to slightly different parameters for the growth at the edge of the wafer, the width of the well and/or the height of the barrier are slightly changed for the second sample; the second subband is pushed higher, towards the continuum. One can see that the absorption spectrum becomes weaker and broader with a pronounced tail at higher energies.

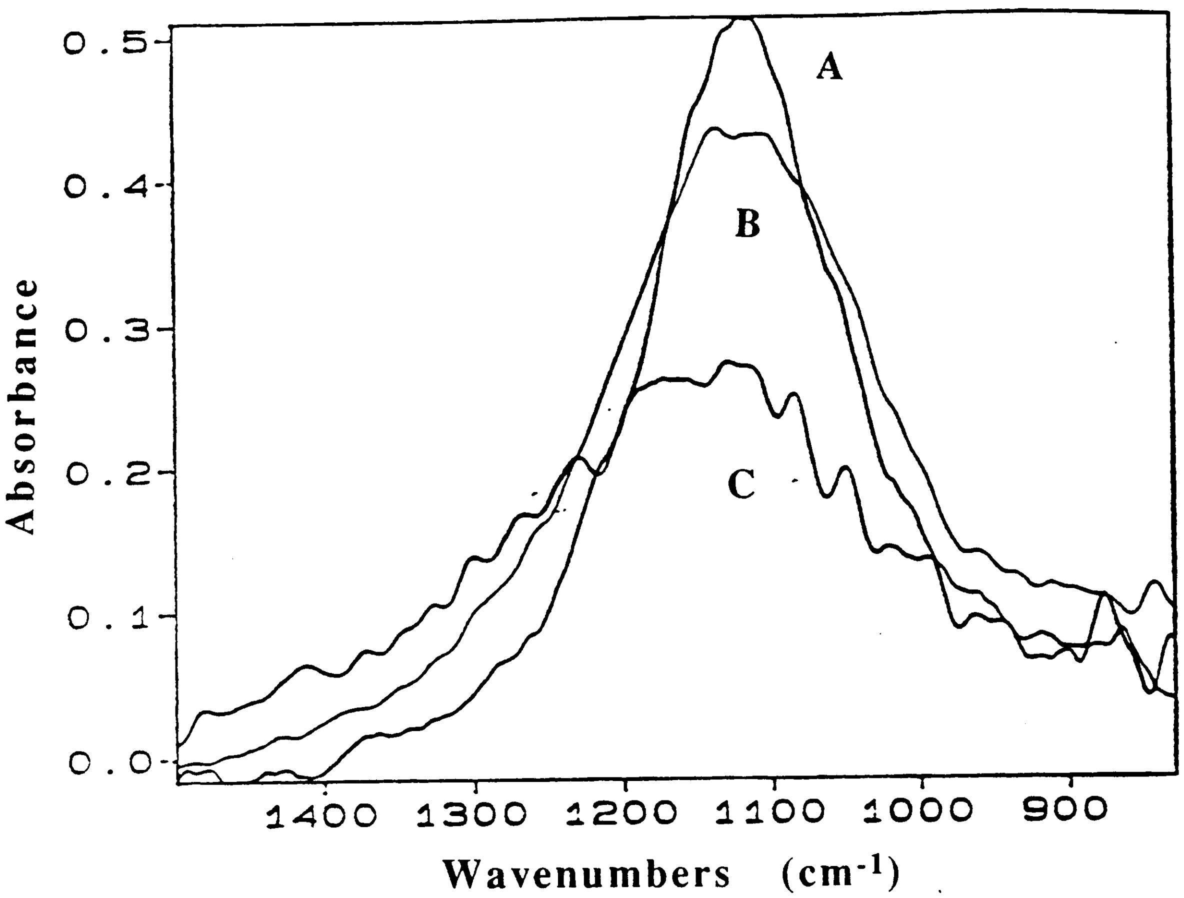

Figure 3.4. Intersubband absorption of three samples, cut from the center of three different wafers grown in the same batch. The stronger and narrower spectrum belongs to the sample designed to have a second subband just inside the well. The two additional samples were grown identical in any aspect, but for the quantum well width, which was designed to be narrower, respectively by one or two monolayers. The two additional spectra display a weaker absorption, spread to a larger bandwidth, with a significant tail for higher energies.

design was such to have the second subband located very close to the top of the well, for the center sample. The variations in growth parameters, for the sample from the edge, were such to push the second subband towards the continuum to a more extended nature. This is reflected in the different absorption spectra: we see that the edge sample displays a weaker yet broader absorption with a pronounced tail at higher energies. Figure 3.4 displays results of absorptions from three different samples, grown in separate runs, but in the same batch of MBE operation. All samples were cut from the center pieces of their respective wafers. The samples were designed to have the width of the quantum well shrinking progressively by one (sample B) and then two (sample C) monolayers, with respect to sample A. The results should be that the excited subband is pushed toward the continuum in sample B, and even more so in sample C, while the parameters of sample A had been designed so as to locate the second subband just close to the top of the well. Again one can see the same trend in the absorption spectra of the three samples, as the nature of the transition changes towards the bound-to-extended type.

3.3.2 Photocurrent measurements

Once absorption measurements and/or some complimentary techniques were performed on a grown MBE wafer, the accuracy of the design and the quality of the growth were determined. For wafers presenting acceptable results, the next step was to prepare samples for actual devices. This was done by using standard processing techniques such as photolitography, wet chemical etching , metallization, preparation of Ohmic contacts and wire-bonding for external leads.

Devices were generally prepared into mesa 100 or 200 µm in diameter, etched from the top n^+ cap layer a few microns so as to reach the bottom n^+ layer below the multi quantum well active region. Au-Ge/Ni/Au Ohmic contacts were provided by evaporation and subsequent alloying at 380 ^{0}C. The edge of the wafer was then lapped to 45^0 , leaving the mesa sitting on the edge. The infrared light to be detected enters the substrate side at normal incidence to the oblique lapped edge. The light usually performs two passes through the active multi quantum well region, as it is reflected from the gold contact layer on top of the device. This scheme for device preparation and measurement geometry is shown in Figure 3.5.

Devices complete with external contacts were then mounted on the cold finger of a cryogenic system. A "SuperTran" cryostat was purchased from the Janis Research Company and adapted to our needs. This continuous flow cryostat combines a flexible transfer line with a cold finger head and provides adjustable refrigeration from a few degrees Kelvin up to room temperature. Liquid helium is continuously transferred through a superinsulated line to the copper sample mount in the vacuum jacket (shroud). The temperature of operation is set by a needle valve located at the bottom of the transfer line, which controls the cryogenic flow to the sample mount and by a heater element located on the sample mount itself. A calibrated Si diode resistance sensor is inserted on the sample mount for accurate temperature reading

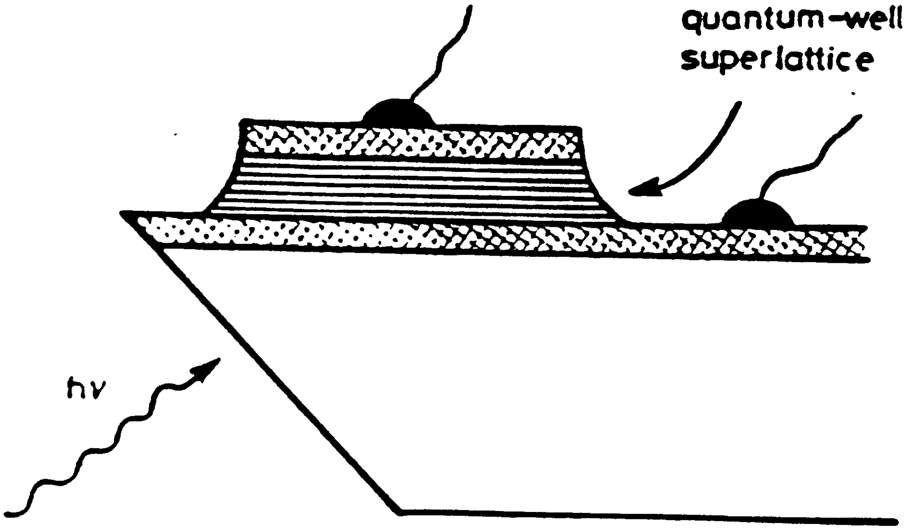

Figure 3.5. Geometry of illumination for detector operation. The sample is lapped on the side by 45° . Mesas of diameter 50 - 200 μm are defined by standard photolithographic techniques. Wire bonding to Ohmic contacts is provided. The incident light is reflected from the top of the mesa and makes two passes in the superlattice.

and control. A radiation shield is connected to the cooling stages to ensure minimum background radiation. The entrance window is made of ZnSe and has been anti-reflection coated for the wavelengths of interest. The arrangement allows for an infrared filter of our choice to be positioned between the entrance window and the detector sample while refrigerated to the lowest temperatures available in the experiment.

Photocurrent measurements were performed in two complimentary modes. First a spectral distribution of the photocurrent was measured with the FTIR. In this mode of operation, our device under test is connected as the detector of the FTIR system, replacing the other options provided by the manufacturer, such as the HgCdTe detector used for absorption measurements. The transfer function and relative spectral response of the FTIR to the whole range of wavelength of interest, include the blackbody source and the various optical components (beamsplitters, mirrors, filters etc.). This system spectral response can be separated from the bare detector spectral response, in which we are interested. This can be done by monitoring the response of the system using another detector, provided by the manufacturer, and known to be flat in response over the whole spectral range of interest (DTGS detector). This measurement provides the spectral relative response within the wavelength range of interest. An additional measurement is needed to obtain an absolute calibration of the responsivity or quantum efficiency of the detector. For this purpose a second setup is used, in which a calibrated blackbody source is used together with a set of cooled filters of known characteristics; the setup includes some simple yet accurate electronic amplification stages; the geometry of the setup has also to be recorded with care for the compelling radiometric calculations. Working with a narrow filter allows us to obtain a calibrated value of the responsivity for one point on the spectral response; this, combined with the FTIR measurements, yields the complete and calibrated spectral response. In general, more than one point on the spectral curve was calibrated, using different narrow-band filters. This served also as an independent check for the scaling of the FTIR spectral response data. In many instances, including results presented in chapters 3 and 4, our results were confirmed and complemented by independent measurement performed on our samples at JPL in the infrared focal arrays laboratory.

3.3.3 Dark current and noise measurements

Another essential parameter which has to be measured for full detector characterization is the noise equivalent power, or more generally the noise characteristics of the detector [16]. This measurement, combined with the responsivity measurements described above, eventually yield the detectivity of the detector, which is the ultimate figure of merit for such devices and has been defined in chapter 2. Information on the noise performance of our detectors were obtained both from a direct measurement of the spectral noise (with the help of a spectral analyzer) , and from the monitoring of the dark I-V curves. These measurements, as the previously described responsivity measurements, were performed for the temperature range of interest, from a few degrees Kelvin, to higher temperatures for which the performances of the detectors were still acceptable; usually this limit is not much higher than the liquid nitrogen temperature of 77 ^{O}K.

For these measurements, the sample is attached to the cold finger of the cryostat and the entrance window is covered with an opaque element held at the cold shield temperature. In this way the background radiation is provided by the cool shield only and is quite low, the noise reflecting mostly thermal excitations or generation-recombination processes involving the tunneling dark currents. Additional measurement for dark currents and spectral noise can be performed in the open window configuration, allowing for the background radiation, dictated by the background temperature and the angle of view, to be much larger. A comparison between the open window and dark configurations is also quite a simple and accurate method to determine the BLIP temperature of the detector, for which the noise current associated with the generation-recombination processes originating from the background radiation is equal to the noise current generated by the thermal fluctuations and the tunneling effects, as defined in chapter 2.

3.4 Intersubband detectors: experimental results

During the first period of the research presented in this thesis, our efforts were

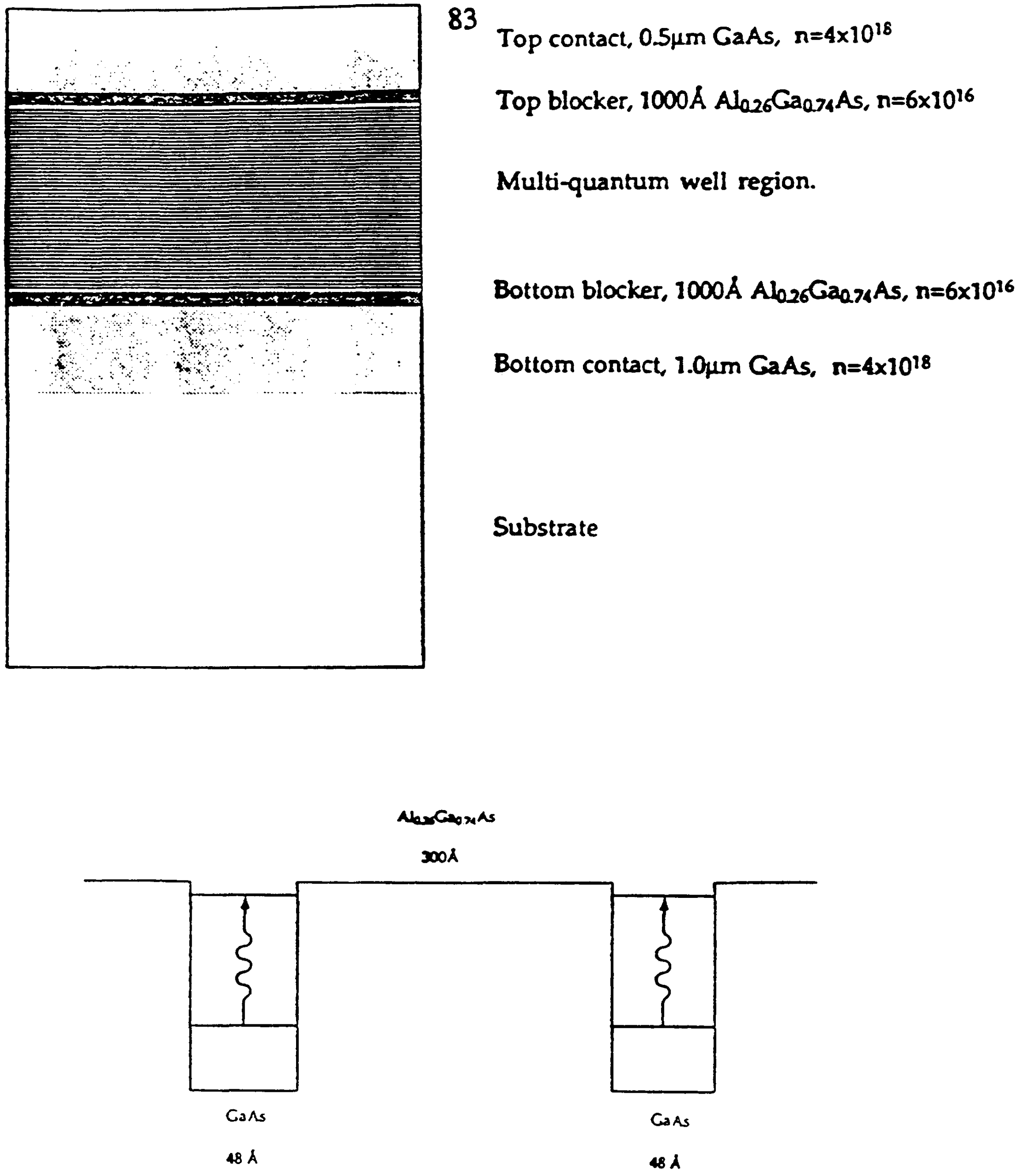

Figure 3.6. Design and growth parameters for a detector devised for operation around 8 μm. On the top the general structure, as grown by MBE. On the bottom the relevant parameters of the quantum wells and the barriers. The MQW region included 50 quantum wells, all doped in their central 38 Å to n= 4x10^{18} cm^{-3}.

devoted to the understanding of the basic limits of intersubband detection; at the same time we were building up all the laboratory facilities, and developing the experimental techniques needed for the study of intersubband physics and applications. This was followed by an effort to design and grow standard intersubband detectors, and eventually to optimize their performances. We call "standard" detectors those designed in a simple square well configuration, with one ground subband inside the well and one excited subband located very close to the top of the well, or even above the AlGaAs barrier Γ point, in the continuum.

Very good detectors were eventually obtained. This required some optimization of growth parameters and some improvements in the design, to limit dark currents.

Figure 3.6 displays the layout of a sample, designed for detection around 8 μm and grown by MBE. Calculations according to the simple finite square-well model, including nonparabolicity, including material parameters as presented above, anticipated an intersubband absorption spectrum peaked at 8.0 μm, corresponding to a transition between the ground subband and the first excited subband located just a few meV below the top of the well. Note that the barriers separating quantum wells are 300 Å long, and that the design includes two longer blocking barriers at the edge of the superlattice. This design attempts to substantially limit the dark current through the device, which is necessary for good noise performance of the detectors.

Figure 3.7 displays a set of absorption measurements, as performed on the sample, for different polarization angles of the incident infrared light; note that all baselines have been slightly offset one from the other, for better visual

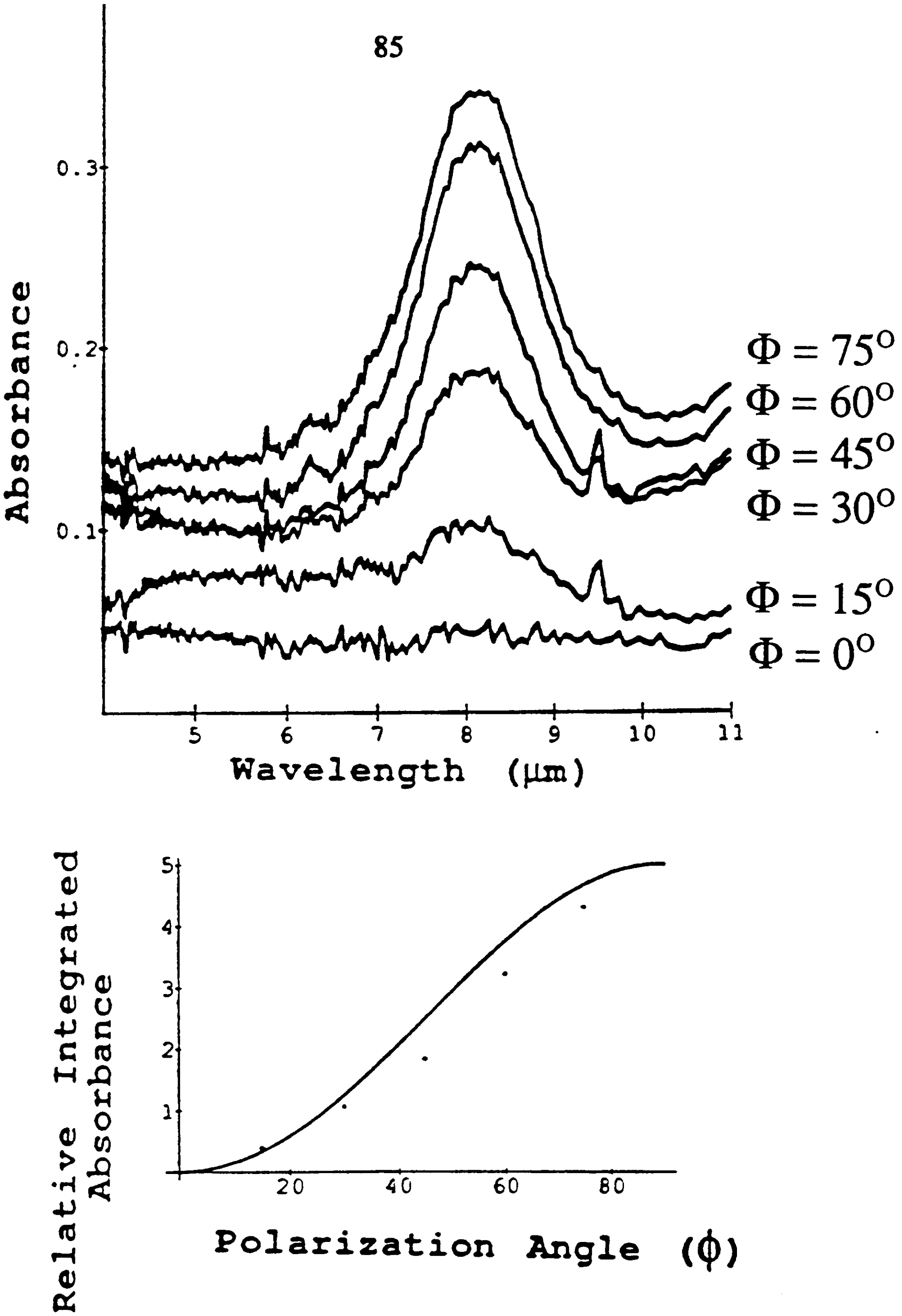

Figure 3.7. Intersubband absorption measurements for different settings of the entrance polarizer, for the 8 μm detector wafer (upper); and the check of the correct square-sinuisoidal law for absorbed intensity as a function of polarization angle, to verify that the absortions follow the intersubband selection rules (lower).

1045.IR-Photoresponse

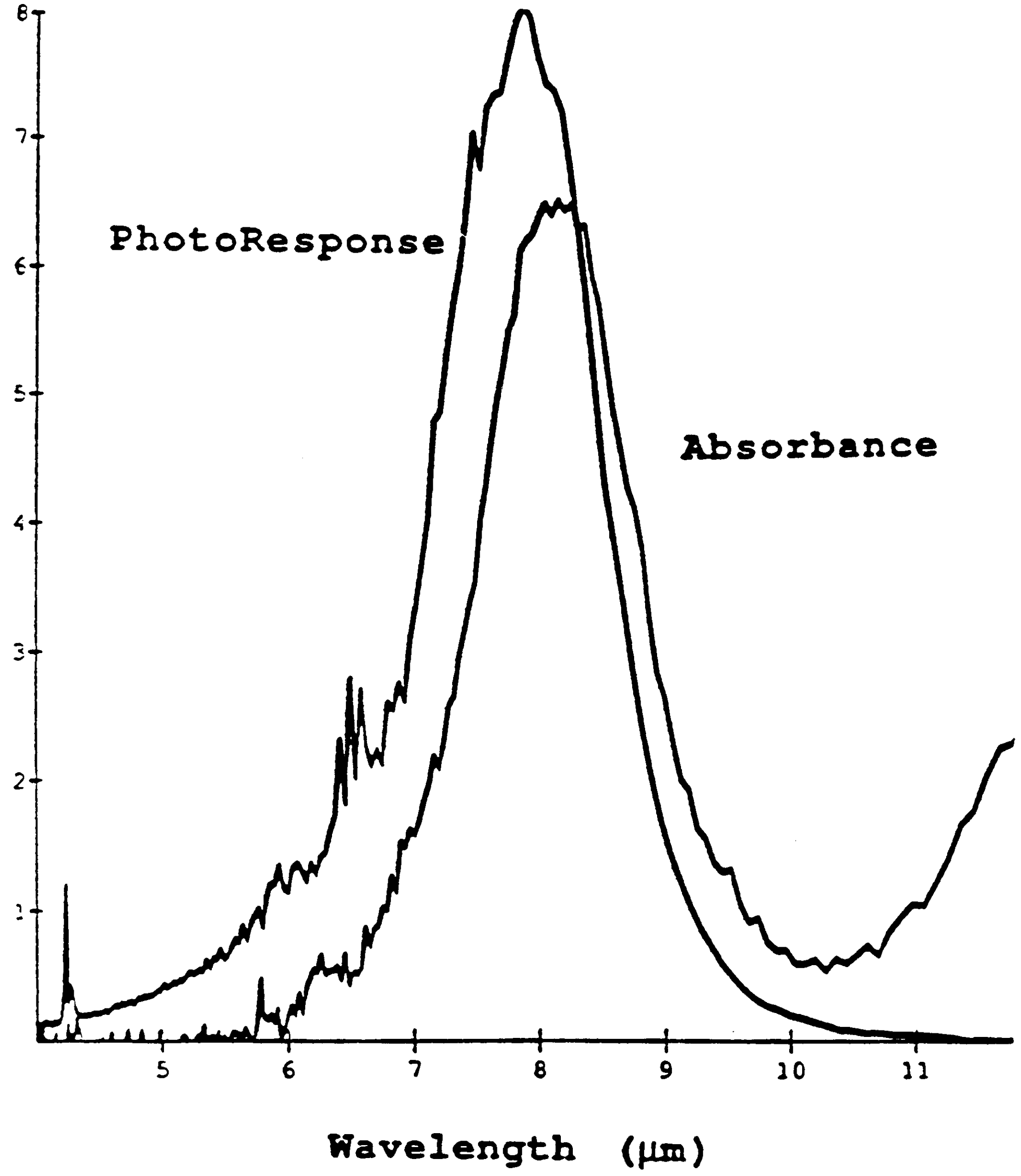

Figure 3.8. Absorption and photocurrent spectroscopies of the 8 μm detector. Arbitrary units are used on the ordinate axis. Note the small shift in the peak center wavelength.

differentiation; the scale on the left, in absorbance units, refers to the measurement at the smallest polarization angle. In addition, Figure 3.7 displays the dependence of the absorption on the polarization angle, which should follow a $\sin^2\Phi$ law, as can be inferred from application of the intersubband selection rules. These kinds of measurements are used to verify that the absorption is due to intersubband transitions, and not to other parasitic bulk absorptions.

Figure 3.8 displays the absorption spectroscopy performed at room temperature together with the photocurrent spectroscopy performed at the lower temperature. On the ordinate axis arbitrary units are displayed. The small blue shift of the photoresponse peak with respect to the absorption peak is due in part to the different temperatures at which the measurements have been done (room temperature for absorption and liquid nitrogen temperature for photoresponse), and to the small Stark shift for the applied bias in the photoresponse measurement.

These set of spectral measurements, obtained using the FTIR, were completed by responsivity measurements performed in a setup including a calibrated blackbody source and a set of narrow-band cooled filters .

Figure 3.9 displays the integrated response as recorded when illuminating with a blackbody source. The best integrated response was obtained at a bias of around -5V. Note that the response starts at a voltage slightly larger than -1V; this is due partly to the powerful blocking barriers at the edge of the superlattice, and partly to the fact that the second subband is located a few meV inside the well.

Every detector characterization includes, together with responsivity, also noise

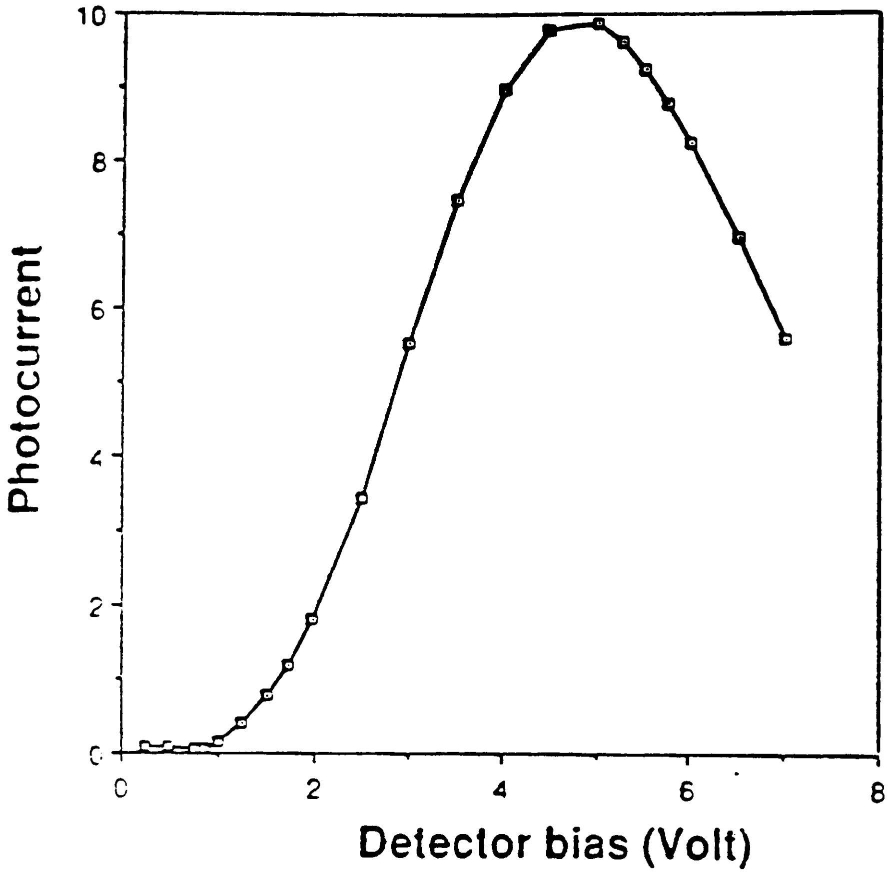

Figure 3.9. Integrated photocurrent as a function of bias for the 8 μm detector.

measurements. We measured the noise equivalent power directly with a spctrum analyzer. The order of magnitude of the noise equivalent current for 1 Hz bandwidth was 0.2 pA.

It is also very important to measure the dark currents, which can limit the performances due to the generation-recombination limit. Example of dark current measurements for this 8 µm sample are presented in Figure 7.10 and Figure 7.11.

From our measurements, for the liquid nitrogen temperature of 77 ^{O}K, peak responsivities of 0.30 A/W (at an applied bias V_b = -4V) and) 0.38 A/W (at an applied bias V_b = -5V) were measured for the peak wavelength around 7.8 µm. These values are not corrected for substrate reflection, light polarization, or area renormalization due to incidence. For Vb = -4V we calculated D^*(peak) = 2.35×10^{10} cm $Hz^{-1/2}W^{-1}$ from the responsivity and noise measurements combined. The differential resistance of the device is very high, and thus measurements can be performed with large load resistors (Megaohm ranges); this yields extremely large voltage responsivities of more than 10^5 V/W.

The values reported above for our 8µm detector are very good, comparable to state-of-the-art performances reported to-date for best intersubband detectors [17,18].

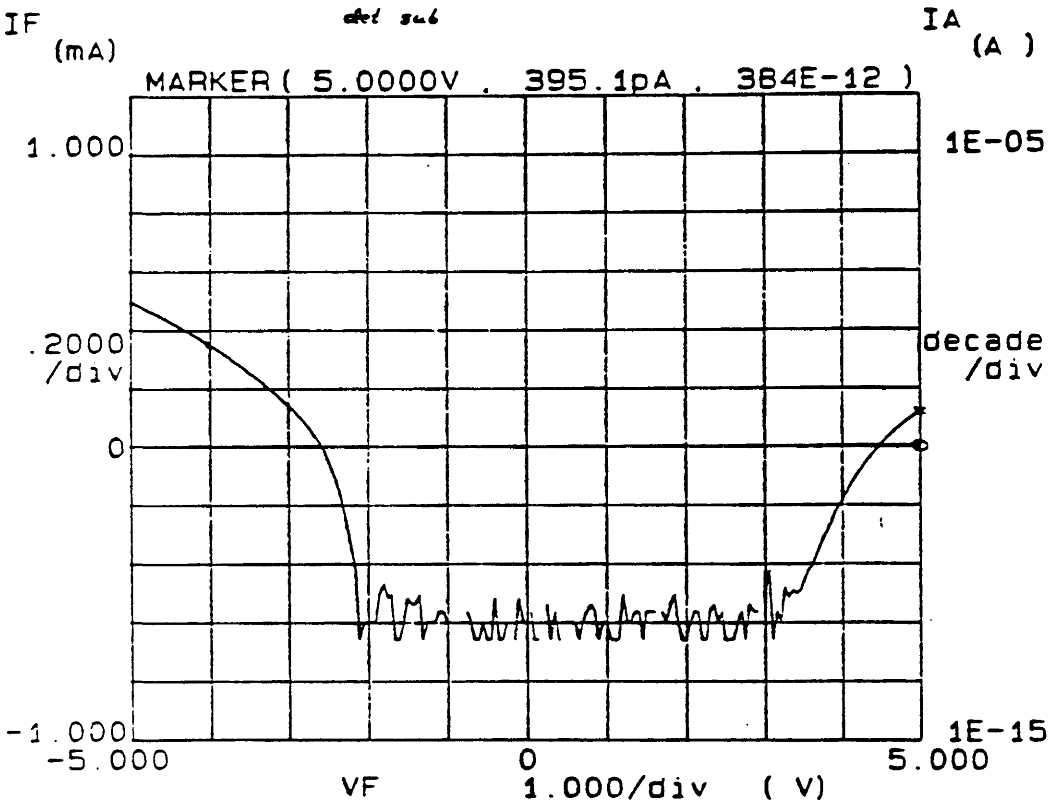

Figure 3.10. Dark current characteristics of the 8 μm detector at 77°K.

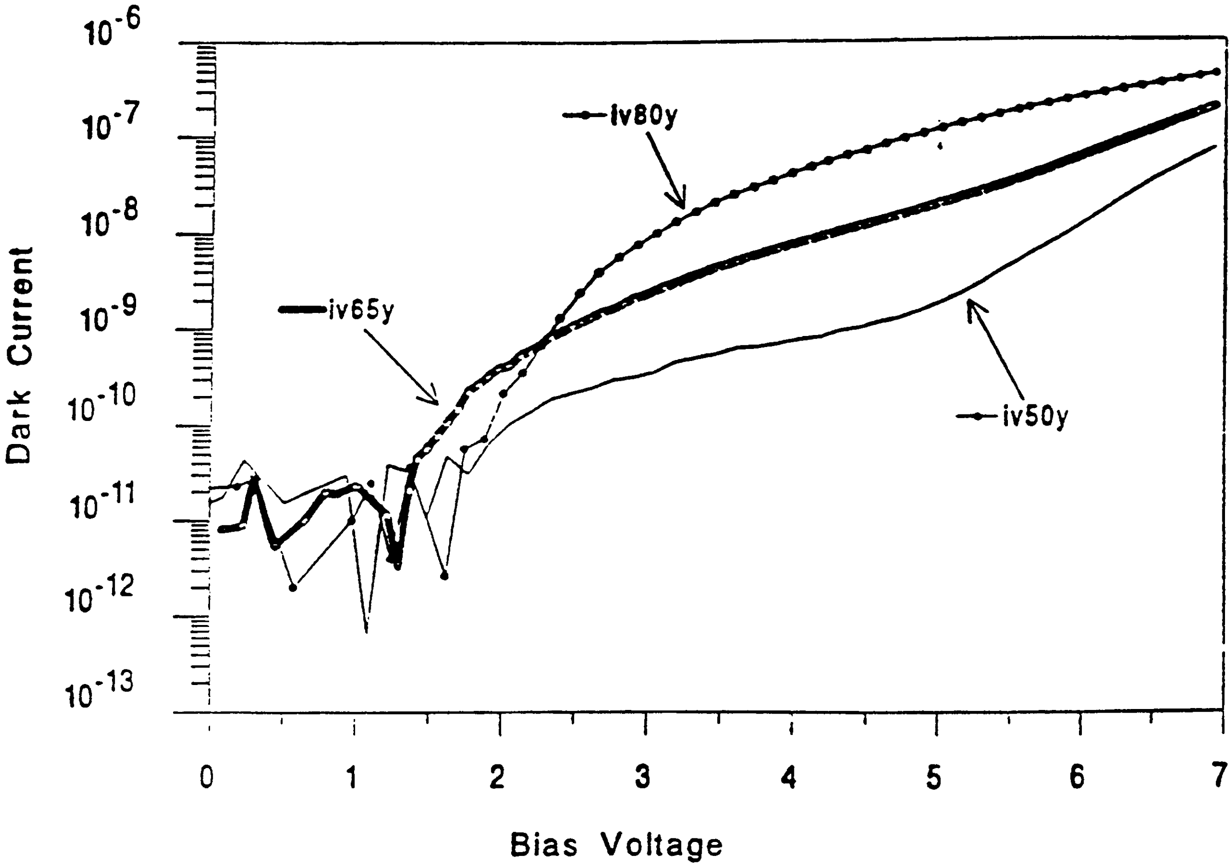

Figure 3.11. The negative branch of the dark I-V characteristics of the 8 μm detector as measured at different temperatures.

3.5 Conclusions

We have presented in this chapter an overview of the design, growth, preparation and characterization of intersubband devices. During the first period of the research, all techniques needed for the design, growth and characterization of detector samples were developed and established in our laboratories. These included MBE growth of intersubband samples, and the optimization of growth parameters , infrared absorption and photocurrent spectroscopies, together with noise and dark current measurements. Our results, presented here for an 8-μm intersubband detector, are comparable to state-of-the-art performances of these devices.

References

[1] S. Adachi, J. Appl. Phys. 58, R1 (1985).

[2] J.S. Blakemore, J. Appl. Phys. 53, R123 (1982).

[3] H.C. Casey and M.B. Panish, "Heterostructure lasers". Academic Press (1978).

[4] Z.Y. Xu, V.G. Kreismanis, and C.L. Tang, Appl. Phys. Lett. 43, 415 (1983).

[5] Z. Ikonic, V. Milanovic, and D. Tjapkin, Appl. Phys. Lett. 54, 247 (1989)

[6] S.D. Gunapala, B.F. Levine, L. Pfeiffer, and K. West, J. Appl. Phys. 69,6517 (1991).

[7] K.M.S.V. Bandara, D.D. Coon, Byungsung O, Y.F. Lin, and M.H. Francombe, Appl. Phys. Lett. 53, 1931 (1988)

[8] J.W. Choe, Byungsung O, K.M.S.V. Bandara, D.D. Coon, Appl. Phys. Lett 56, 1679 (1990).

[9] G.M. Williams, R.E. DeWames, C.W. Farley, and R.J. Anderson, Appl. Phys. Lett. 60, 1324 (1992).

[10] L.C. West and S.J. Englash, Appl. Phys. Lett. 46, 1156 (1985).

[11] B.F. Levine, R.J. Malik, J. Walker, K.K. Choi, C.G. Bethea, D.A. Kleinman, and J.M. Vandenberg, Appl. Phys. Lett. 50, 273 (1987).

[12] K.W. Goossen, S.A. Lyon, and K. Alavi, Appl. Phys. Lett. 53, 1027 (1988).

[13] G. Hasnain, B.F. Levine, C.G. Bethea, R.A. Logan, J. Walker, and R.J. Malik, Appl. Phys. Lett. 54, 2515 (1989).

[14] M.O. Manasreh, F. Szmulovic, D.W. Fischer, K.R. Evans, and C.E. Stutz, Appl. Phys. Lett. 57, 1790 (1990).

[15] B.F. Levine, C.G. Bethea, K.K. Choi, J Walker, and R.J. Malik, J. Appl. Phys. 64, 1591 (1988).

[16] E. Pelvé, F. Beltram, C.G. Bethea, B.F. Levine, V.O. Shen, S.J. Hsieh, and R.R. Abbott, J. Appl. Phys. 66, 5656 (1989).

[17] B.F. Levine, C.G. Bethea, G. Hasnain, V.O. Shen, E. Pelve, R.R. Abbott, S.J. Hsieh, Appl. Phys. Lett. 56, 851 (1990).

[18] B.K. Janousek, M.J. Daugherty, M.L. Bloss, M.L. Rosenbluth, M.J. O'Loughlin, H. Kanter, F.J. De Luccia, and L.E. Perry, J. Appl. Phys. 67, 7608 (1990).

Chapter 4

Multi-spectral infrared detectors

4.1 Introduction

Among the features of MQW infrared detectors, we pointed out previously a narrow spectral range of detection ranging in width around 10-20% of the peak wavelength. A bound-to-continuum detector designed for peak responsivity at - say - 10 μm, would typically have the response larger than half the peak value between 9.5 μm and 10.5 μm [1]. In some applications this could be considered an advantage; in many other situations one would like to achieve as broad a range of detection as possible. Attempts have been made to address this issue. For example, Levine et al. noted that by designing a detector in which the excited subband is "pushed deep in the continuum" the spectral bandwidth is enlarged to cover the important atmospheric window 8-12 μm. This came, however, at the expense of responsivity and of a lower temperature of operation for acceptable performances [2].

A second issue which can be seen as limiting in many applications is the lack of flexibility, as for the peak wavelength and the whole spectral range, once the device has been designed and grown. During the design stage one can choose and tune the detector 's spectral parameters to his/her own needs. Once grown and prepared as an operating device very little can be made to change, tune or adjust the active spectral range. Few attempts to obtain a MQW tunable detector have been made, mainly using Stark shift effects in various configurations [3-5]. However, these attempts suffered from either a low responsivity or too small a tunability range.

Last, but not least, future needs in the use of thermal imaging systems in the mid infrared, will undoubtedly include a multispectral capability for the system and/or the device. This projection can hinge on the history and the trends observed in the much more developed visible and near infrared range.

Following these considerations we designed a multi-color detector based on the serial integration of different quantum wells, or stacks of quantum wells, each stack designed for response at a different peak wavelength. As we will show in this chapter, the results of our measurements not only achieved, in principle, the goals outlined above, but also revealed some new basic physical effects linked to the formation, propagation and readjustment of electric field domains in superlattices [6]. There is hope that these effects could be used, in the future, not only for the design of efficient multispectra detectors, but for an even larger class of general optoelectronic devices.

4.2 Design and characterization of the multi-stack infrared detector

This new type of bound-to-continuum GaAs infrared detector consists of three different stacks of quantum wells arranged in series. All the wells in a given stack are identical, but each stack is designed for absorption and detection at a different wavelength, featuring distinct well widths and barrier heights.

The structure was grown by molecular beam epitaxy on a semi-insulating GaAs substrate. The multi quantum well region, clad by two n-doped contact layers, consisted of 3 stacks of 25 quantum wells each; the first 25 wells were 3.9 nm wide and were separated by $Al_{0.38}Ga_{0.62}As$ barriers; the second stack consisted of 25 quantum wells 4.4 nm wide with $Al_{0.30}Ga_{0.70}As$ barriers; the last stack had 25 wells 5.0 nm wide and $Al_{0.24}Ga_{0.76}As$ barriers. All the barriers were 44 nm long; the wells and the contacts were uniformly doped with Si to $n=4\text{x}10^{18}$ cm^{-3}. The schematic conduction band diagram is shown in Figure 4.1.

The calculations used in our design follow the data, the parameters, and the schemes outlined in Chapter 3. They include band nonparabolicity [7], and a band offset value of 0.60. The structure was thus designed to display peaks of absorption at 1335, 1052 and 880 cm^{-1}. Each peak corresponds to absorption from one stack, starting from the one grown close to the substrate designed for shorter wavelength detection, up to the stack grown last, designed for the longer wavelengths.

At first we were interested in analyzing the absorption and photocurrent spectral properties of the whole structure. Eventually, one can incorporate in the

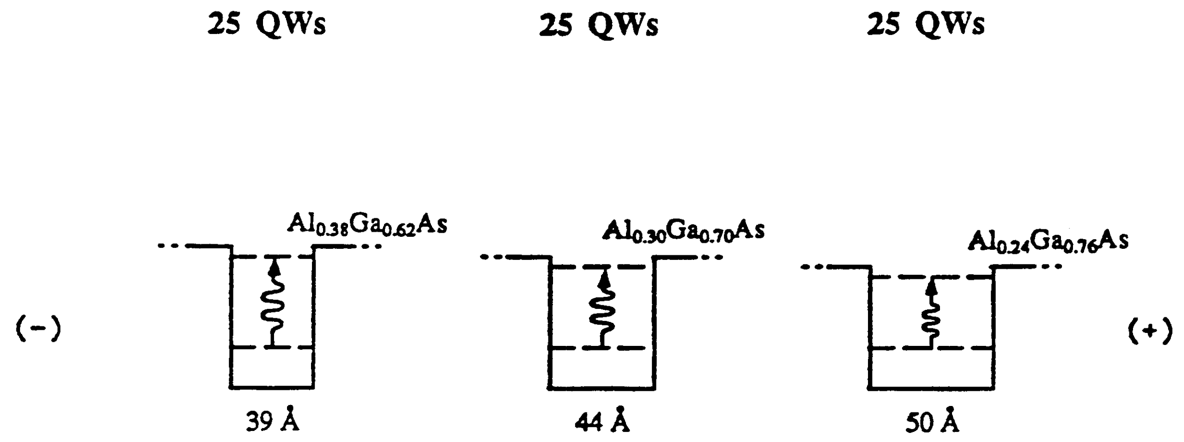

Figure 4.1. The conduction band profile of the multistack detector. Starting from the semi-insulating substrate, there are three stacks of quantum wells. Each stack consists of 25 identical quantum wells. Each stack is designed to yield a peak photoresponse at a different wavelength. This is achieved by changing the width of the wells and the Al percentage in the composition of the barriers, among the different stacks. The shortest wavelengths are detected by the stack closer to the substrate and the longest ones by the stack on top of the device.

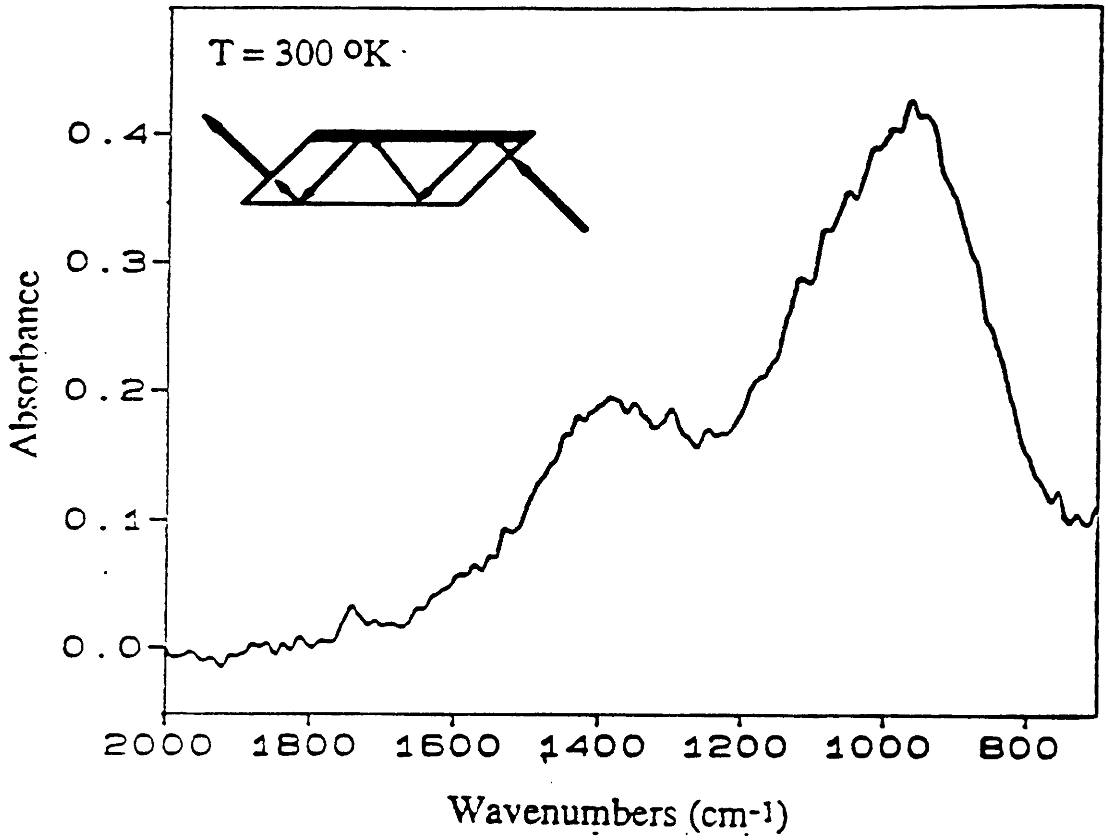

Figure 4.2. Absorption spectrum at room temperature. The measurement was performed with a Fourier transform spectrometer using a waveguide geometry as shown in the inset; the spectrum is normalized to reflect the contribution of the intersubband absorption alone. An absorption coefficient $\alpha_{45} = 600\ \mathrm{cm^{-1}}$ for the peak at 1364 $\mathrm{cm^{-1}}$ was derived.

design contact layers straddling each different group of quantum wells, thus allowing separate access and bias to each stack.

The absorption at zero field and room temperature is shown in Fig. 4.2. The measurement was taken with our Fourier transform infrared spectrometer in the usual waveguide geometry; the absorption of light polarized in compliance with the selection rules was normalized by the absorption of light polarized in the perpendicular direction, to allow for only the intersubband contribution. The absorption peak at 1364 cm^{-1} is due to the 3.9 nm wells while the stronger absorption centered at 964 cm^{-1} is the composite contribution of the two other species of quantum wells, which, individually, have absorption peaking at 1080 and 920 cm^{-1}. These results agree well with our design values. We see that in each of the 3 different types of wells, light is absorbed by electrons excited from the first subband to a second subband which is located close to the top of the well. The blue shift in the experimental values versus the calculated ones can be accounted for with the inclusion of the exchange interaction [8] in the calculated values; in these heavily doped samples, the correction supplied by many-body effects is noticeable. The existence of two absorption peaks that merge into a wide and strong peak was also experimentally verified by analyzing the absorption of a few additional MBE grown control wafers, which were designed to include, each time, only two of the stacks described above.

Devices were processed out of the grown wafer and prepared as etched mesa, 200 μm in diameter. Fig. 4.3(a) displays the smoothed photocurrent spectroscopy of

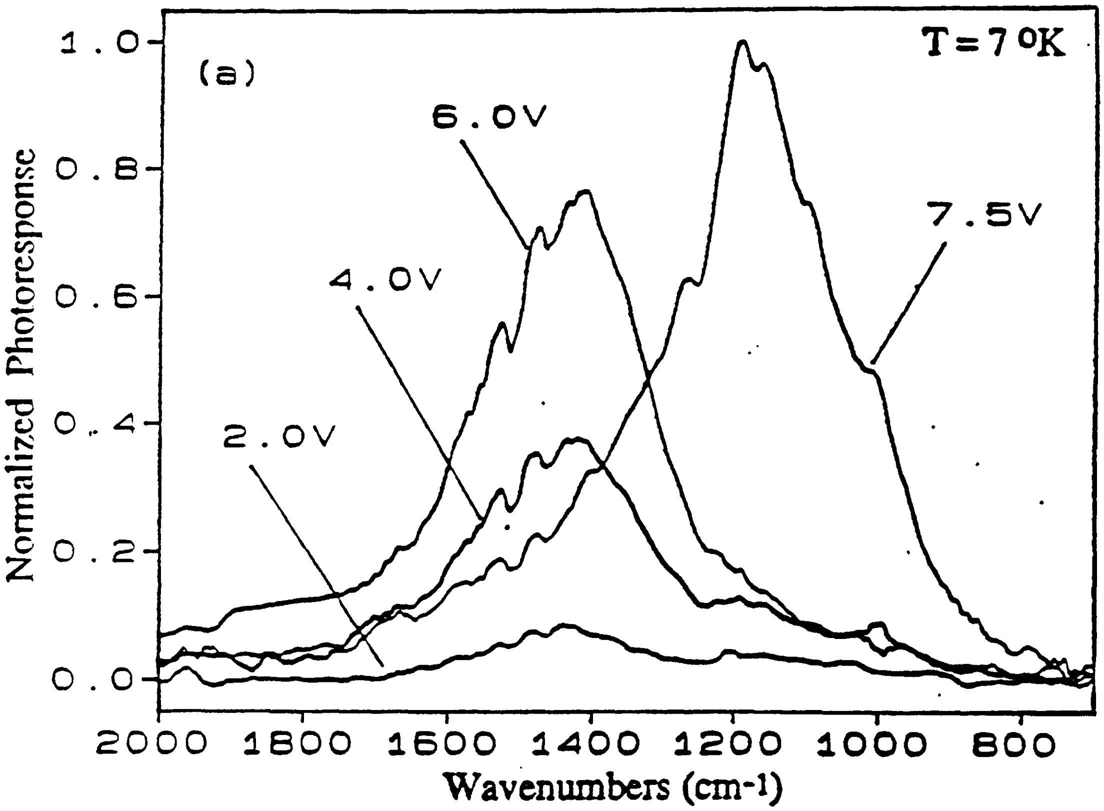

Figure 4.3. (a) Spectral photoresponse for few value of applied positive voltage. Note the switching in peaks at an applied voltage around 6.5 V. The responsivity at the peak of 1140 cm and the applied voltage of 7.5 V is 0.75 A/W.

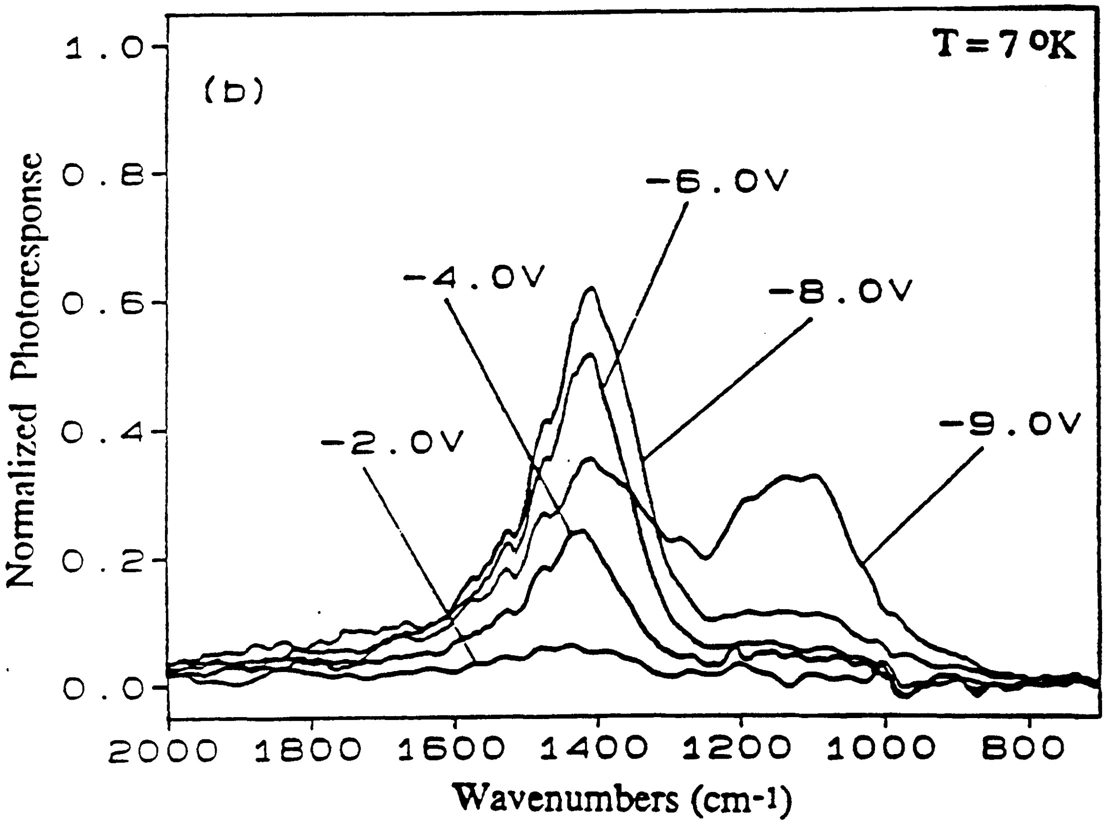

Figure 4.3. (b) Spectral photoresponse for few values of applied negative voltage. Note the broadening in the spectral response below -8.0 V. For still lower voltages (around -13 V), the third peak begins to contribute (not shown in the figure). The units are the same for both figures 4.3 (a) and (b).

a device at a temperature of 7 ^{0}K, for different values of the applied voltage; the polarity is defined here as positive when the higher potential is applied to the cap layer on top of the mesa. It is seen that, for low applied field, the first stack of 3.9 nm wells, closer to the substrate, provides most of the photocurrent at the appropriate excitation energies around the peak of 1411 cm^{-1}. When the bias is increased above a threshold of 6.5 volts, a sharp transition takes place and the responsivity peak switches to 1140 cm^{-1}; it is apparent that the second stack of quantum wells is now responsible for most of the photocurrent, while the contribution from the first stack has sensibly decreased. Note that the small shifts of the photocurrent peaks with regard to the absorption peaks are due to the different experimental temperatures [9] and to the applied electric field [10]. If we apply a negative bias to the detector [Fig. 4.3(b)], again, at low voltages, the photocurrent is due mostly to electrons excited in the first stack of wells; the responsivity increases with the applied voltage , but its magnitude is always less than that corresponding to the same forward bias; in addition one observes that the photocurrent peak around 1400 cm^{-1} is much broader in the forward bias mode. When the bias is increased to more negative values, the responsivity extends to lower energies, showing increasing contributions from the second stack: the first stack continues to contribute a constant value to the photocurrent, in contrast to the reduction in response experienced in the opposite polarity of the applied electric field. For still more negative voltages, it is apparent from our results that the spectral domain of significant response expands to still lower energies, to include contributions from the third stack of wells, around

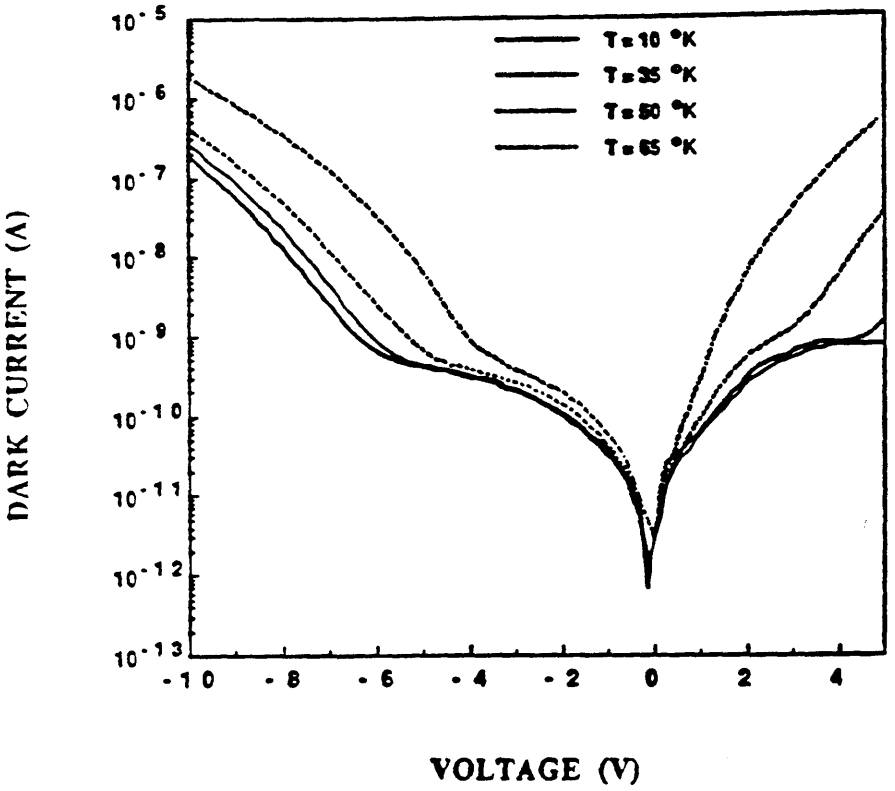

Figure 4.4. Dark currents at different temperatures as measured in the shielded, cold window configuration.

900 cm^{-1}.

From these results it is apparent that the detector can operate in one of a number of modes. At forward and low bias voltages, the response peaks at a single wavelength (~ 1400 cm^{-1}) and the device functions as a standard bound-to-continuum infrared detector [1]. When exceeding a critical applied voltage, the detector's spectral response switches to a different peak wavelength (~1140 cm^{-1}), while the detection at the previous peak is significantly reduced. Thus the detector can operate as a two-color, voltage controlled switching device. At a reverse bias the detection is again centered on the higher energy peak (~ 1400 cm^{-1}) up to a specific applied voltage; for moderately higher voltages, two peaks yield a significant photoresponse. At still higher values of the reverse voltage a third response peak appears, which results in operation as a wide-band detector. Here the detector works as a voltage-controlled, adjustable-spectral-domain detector. And finally, at large negative bias, the detector has a wide spectral range of response.

The dark current, measured with a cold shielded window is shown at different temperatures in Figure 4.4. One can note a strong asymmetry between the two polarities. A fine structure in the plateaux of the I-V curves (not resolved in Figure 4.4), corresponding to regions of negative differential resistance, was observed and is shown in Figure 4.5. This measurement gives a most important clue to the origin of the switching phenomena, since these negative differential resistance oscillations are the signature of the formation and expansion of high field domain along the sample multi-quantum well region [11-20].

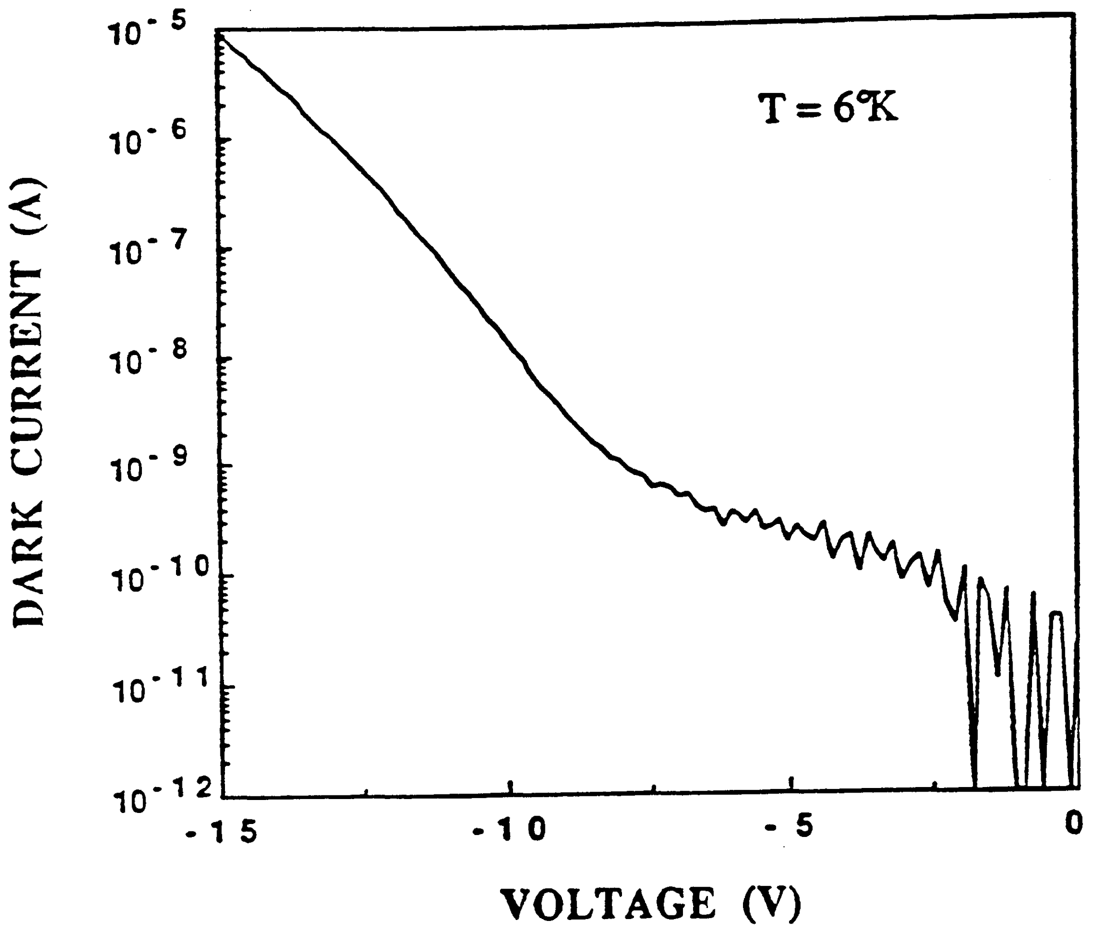

Figure 4.5. The fine structure in the I-V characteristic at low temperatures reveals regions of negative differential resistance. This is an indication of the formation and expansion of a high-field domain in the sample.

The data of the photocurrent spectral measurements were taken with a Fourier transform spectrometer, complemented by a set-up including a calibrated black-body source and a set of cooled filters at different wavelength. The noise equivalent voltage was measured directly with a spectrum analyzer in the cold, shielded window configuration.

One should also note the very low values of the dark current, which, combined with a responsivity ranging up to 0.75A/W, ultimately yield high D* for this detector; the figures here are of the order of magnitude of the best performances as known and published for MQW infrared detectors. Table 4.1 displays figures of detectivities as measured at 40 ^{O}K. The noise characteristics were measured directly with a spectrum analyzer.

Wavelength [μm]	7.2	8.0	9.0	9.8	11.6
Measured D^*_λ [cmHz$^{1/2}$/W]	$7.9\text{x}10^{11}$	$4.6\text{x}10^{11}$	$4.1\text{x}10^{11}$	$2.6\text{x}10^{11}$	$7.0\text{x}10^{10}$

Table 4.1. Measured Detectivity at 40 ^{O}K for different wavelengths.

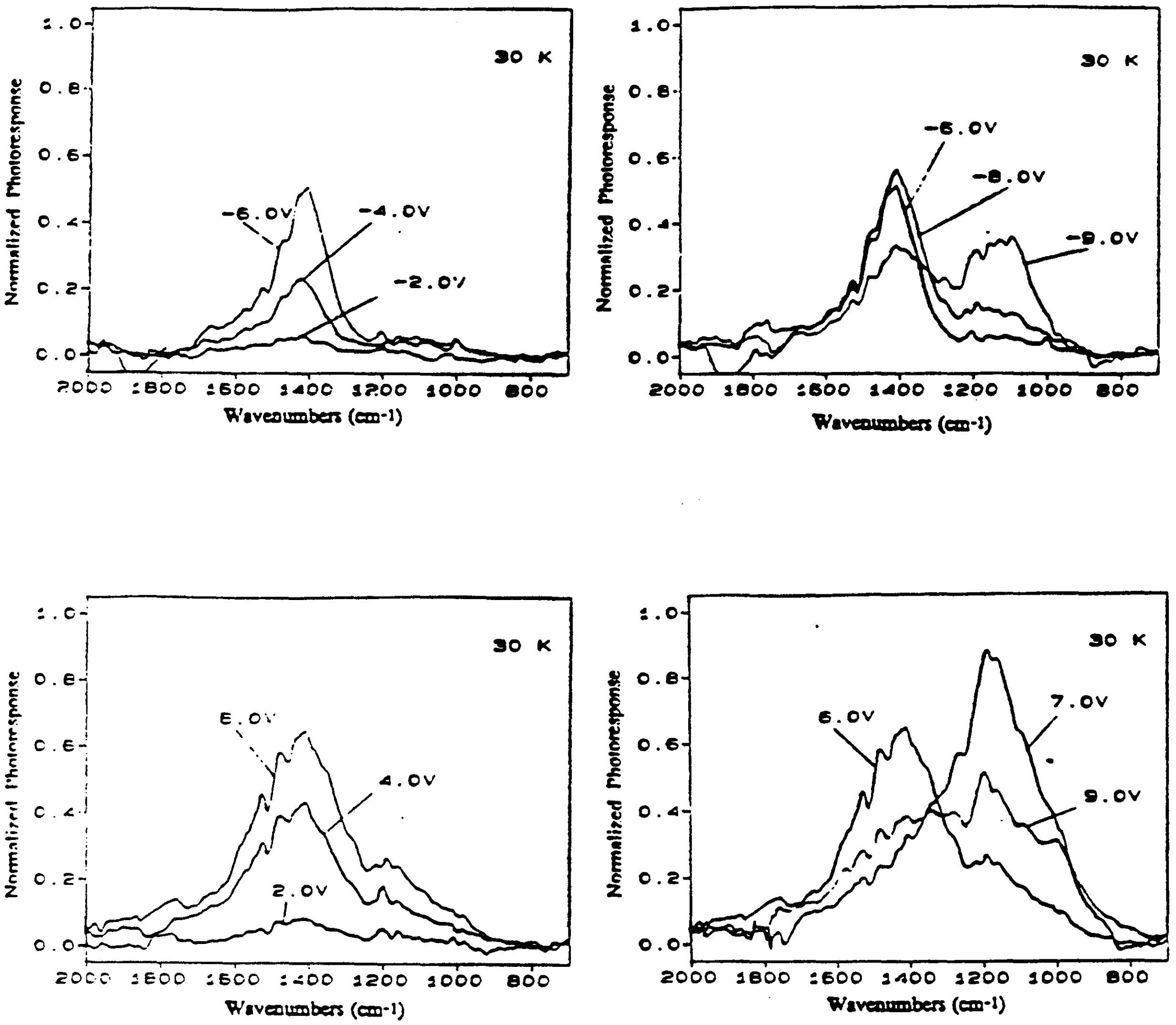

Figure 4.6. (a) Photocurrent spectra at T = 30 °K, for different applied voltages.

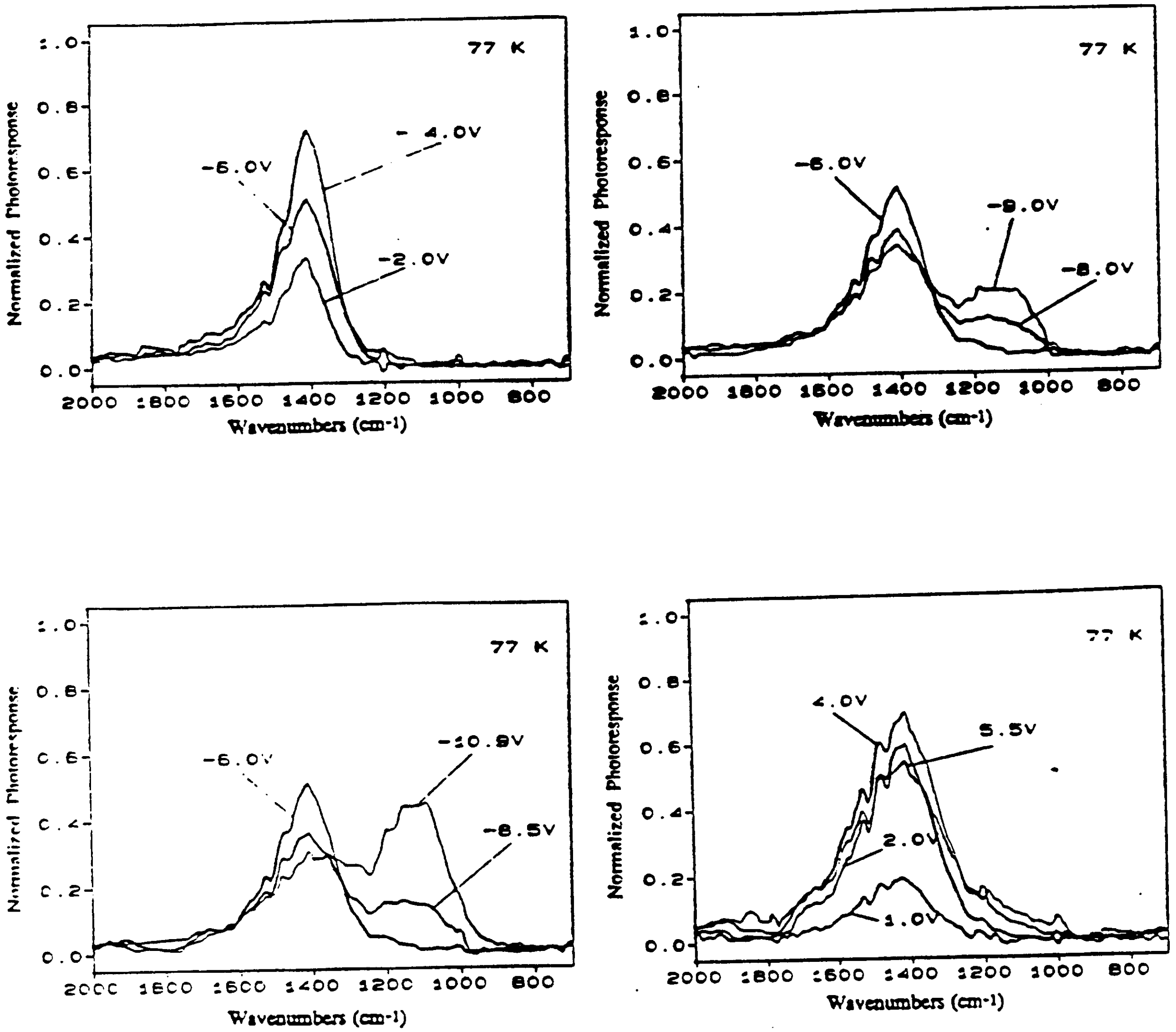

Figure 4.6. (b) Photocurrent spectra at T = 77 °K, for different applied voltages.

The switching behavior, as observed at the temperature of 7 ^{o}K in Fig. 4.3, persists at higher temperatures. In the reverse bias direction, one observes the same general features also at 77 ^{o}K. In the forward polarity, the switching of the photoresponse from the higher energy peak to the lower one is observed up to a temperature of 60 ^{o}K; the critical voltage at which the switching occurs slightly increases with temperature; at still higher temperatures, the dark current at the required voltages becomes too large for practical detection purposes. Examples of photocurrent spectra at different temperatures are shown in Figure 4.6.

4.3 Interpretation of the experimental results

We can interpret the oscillations observed in the I-V characteristics (Fig. 4.5) and the features observed in the photocurrent spectral measurements (Fig.4.3) as evidence for a rich pattern of high and low electric field domains in the sample [11-20]. When the device is biased with a positive polarity, a high-field domain is created in the region close to the cathode within the first stack of quantum wells; as the applied voltage is increased, the domain spreads to include more and more of the 25 wells in the stack, while a complementary low-field domain in the same stack shrinks progressively. At the same time the remaining two stacks of quantum wells experience only low-field domains all along their extent. Thus, photons of all appropriate energies are absorbed by the correspondingly matched, highly doped quantum wells; however only electrons excited within the high-field regions are swept efficiently towards the contacts and contribute to the photocurrent. The carriers excited in the region of low field have a high probability of being recaptured by their own (or neighboring) well, contributing only negligibly to the current. Once the applied voltage reaches a value large enough to extend a high-field domain to as many of the 25 wells in the first stack as allowed, the corresponding responsivity reaches its maximum value. When the applied voltage is increased even further, a high-field domain is formed in the region of the following 25 wells of the second stack, while at the same time quenching of the high-field domain in the first stack occurs. Response from a third peak, corresponding to the third stack, was not achieved even at the highest values of the applied forward voltage, indicating that the spatial region of the last stack is always under low field domain.

When the bias is applied with the opposite negative polarity, the situation is not symmetric. The high-field domain starts expanding, as before , in the region of the first stack of quantum wells; however, for this polarity, it means that the formation of a HFD nucleates from the anode. In addition, beyond a certain magnitude of the applied voltage (~-8.5V), different high-field domains coexist in two different stacks, and ultimately, for even more negative applied bias, a third high-field domain forms also in the third stack of quantum wells.

The pattern of high-field domain formation in our sample display new features, not observed or predicted before, to our best knowledge. For example, for the positive bias case and after the switching-peak voltage of +6.5V, we observe that the set-up (in strength) of electric field domains within the sample is not spatially ordered. It has been thought and always observed, that all possible configurations of electric field domains along a superlattice tend to be spatially ordered, meaning that, from one electrode to the other, along the sample, the strengths of the various domains follow a monotonic order. This is not the case in our sample, for voltages larger than 6.5V, where a low-field domain in stack #1 is followed by a high-field domain in stack #2 and by another low-field domain in stack #3. Second, a region which can be recognized to be under high-field domain for one value of the applied bias, has not been observed to undergo a transition to a lower field domain for a larger value of the applied bias; while in our experiment we observed the quenching of the high-field domain in stack #1 for voltages above 6.5V. We can conclude that we have seen a pattern of electric field domains in a multi-quantum well structure, with features and characteristics much more complex than those observed previously. We have witnessed not only the formation and the expansion of electric field domains in the superlattice, as a function of increasing applied voltage; but also the subsequent readjustment of these domains to a totally new configuration.

4.4 Conclusions

In this chapter we have presented the design and implementation of a new multi-stack intersubband detector. From the device aspect, this design addresses a number of issues recognized as problematic or limiting in intersubband detection, such as a narrow bandwidth and the lack of tunability. Our detector can be used in a number of modes, with extended versatility, to address and solve these issues. Options include a voltage-controlled spectral range of detection and a multicolor, switching peak operation.

From the performance aspect, very large responsivities and detectivities have been measured, comparable to the state-of-the-art results in intersubband detectors.

The complex switching behavior of the sample has been attributed to the formation, expansion and readjustment of electric field domains along the sample. New and more involved phenomena have been observed in the interplay of these domains. We have shown that intersubband photocurrent spectroscopy is a natural tool to study the structure and the dynamics of such domains in carrier-rich superlattices.

References

[1] B.F. Levine, C.G. Bethea, G. Hasnain, J. Walker, R.J. Malik, Appl. Phys. Lett. 53, 296 (1988).

[2] B.F. Levine, G. Hasnain, C.G. Bethea, N. Chand, Appl. Phys. Lett. 54, 2704 (1989).

[3] K.K. Choi, B.F. Levine, C.G. Bethea, J. Walker and R.J. Malik, Phys. Rev. B 39, 8029 (1989).

[4] S.R. Parihar, S.A. Lyon, M. Santos and M. Shayegan, Appl. Phys. Lett. 55, 2417, (1989).

[5] B.F. Levine, C.G. Bethea, V.O. Shen, R.J. Malik, Appl. Phys. Lett. 57, 383 (1990).

[6] I. Gravé, A. Shakouri, N. Kuze and A. Yariv, Appl. Phys. Lett.60, 2362 (1992).

[7] Z.Y. Xu, V.G. Kreismanis and C.L. Tang, Appl. Phys. Lett. 43, 415 (1983).

[8] J.W. Choe, Byungsung O, K.M.S.V. Bandara, D.D. Coon, Appl. Phys. Lett. 56, 1679 (1990).

[9] G. Hasnain, B.F. Levine, C.G. Bethea, R.R. Abbott and S.J. Hseih, J. Appl. Phys. 67, 4361 (1990).

[10] A.Harwit, J.S. Harris, Jr., Appl. Phys. Lett. 50, 685 (1987).

[11] L. Esaki and L.L. Chang, Phys. Rev. Lett. 33, 495 (1974).

[12] K.K. Choi, B.F. Levine, R.J. Malik, J. Walker and C.G. Bethea, Phys. Rev. B 35, 4172 (1987); K.K.Choi, B.F.Levine, C.G.Bethea, J.Walker and R.J.Malik, Appl. Phys. Lett. 50, 1814 (1987).

[13] Y. Kawamura, K. Wakita, H. Asahi and K. Kurumada, Jpn. J. Appl. Phys. .25, L928 (1986); Y. Kamamura, K. Wakita and K. Oe, ibid. 26, L1603 (1987).

[14] H.S. Newman and S.W. Kirchoefer, J. Appl. Phys. 62, 706 (1987).

[15] M. Helm, P. England, E. Colas, F. DeRosa, and S.J. Allen, Jr., Phys. Rev. Lett. 63, 74 (1989).

[16] T.H.H. Vuong, D.C. Tsui, and W.T. Tsang, Appl. Phys. Lett. 52, 981 (1988).

[17] R.E. Cavicchi, D.V. Lang, D. Gershoni, A.M. Sergent, H. Temkin, and M.B. Panish, Phys. Rev. B 38, 13474 (1988).

[18] R.F. Kazarinov and R.A. Suris, Sov. Phys. Semicond. 6, 120 (1972).

[19] H.T. Grahn, H. Schneider, and K. von Klitzing, Appl. Phys. Lett. 54, 1757 (1989).

[20] H.T. Grahn, H. Schneider, and K. von Klitzing, Phys. Rev. B 41, 2890 (1990).

Chapter 5

Infrared spectroscopy of a variably spaced superlattice structure.

5.1 Introduction

We investigate in this chapter the properties of a multi quantum well structure, where the doped quantum wells are clad by variably spaced superlattices. These types of barriers were originally proposed for use as electron filters, to provide novel means of injecting high energy electrons and they were called variably spaced superlattice energy filters (VSSEF) [1]. The conduction band energy diagram of such a variably spaced superlattice barrier, as originally proposed, is shown in Figure 5.1. The VSSEF structure is composed of a number of quantum wells, of different widths, separated by short barriers of the same height and length. The idea is to design the structure so that all the quasibound states in the different quantum wells will be aligned for one particular applied voltage, thus inducing a resonant transmission path; hence the operation as an electron filter. The structure was analyzed with a model that solves the Schroedinger equation exactly in the presence of an electric field, using an Airy

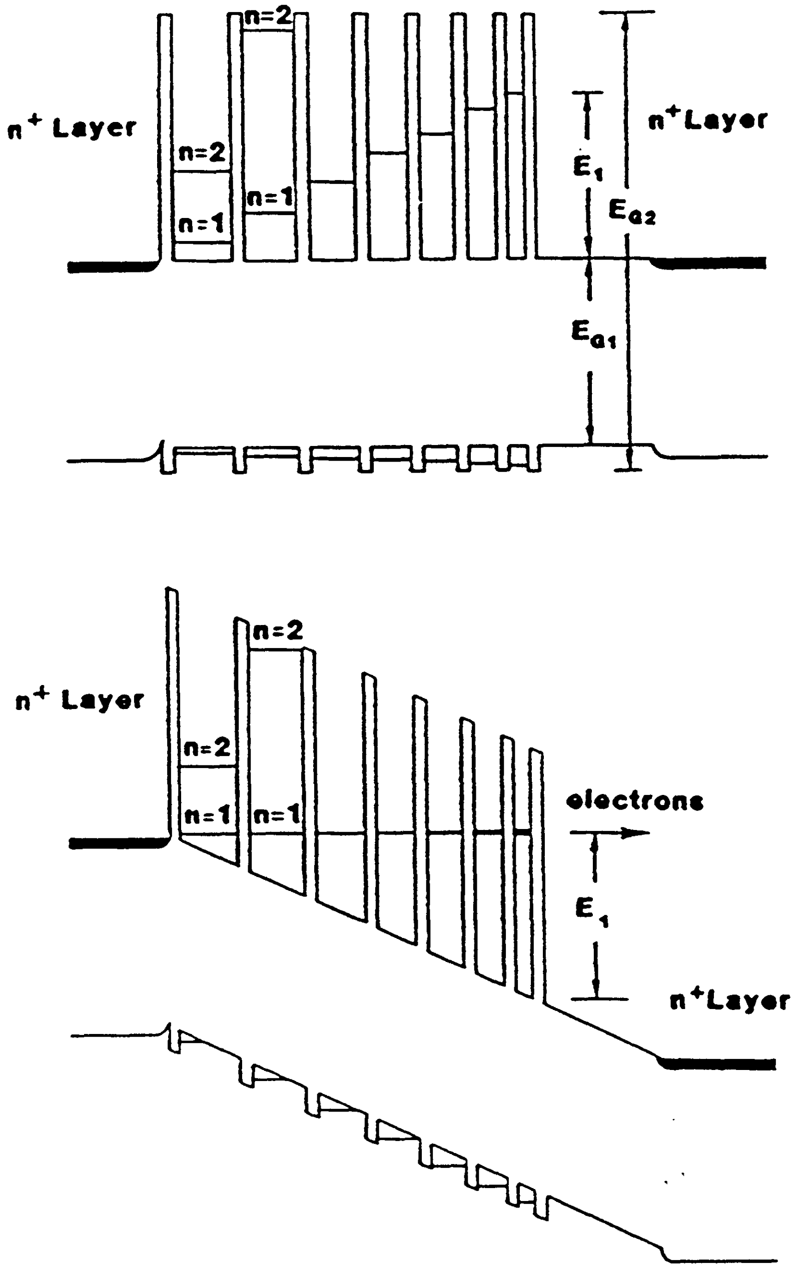

Figure 5.1. The conduction band profile of a variably spaced superlattice electron filter (VSSEF) barrier. The alignment of the quasibound states in the different field is achieved, with proper design, for one specific applied electric field.

function basis, together with the transfer matrix method [2].

This type of VSSEF structures were used as barriers cladding a doped quantum well, and the design of the energy levels inside the doped quantum well was such that under a particular applied bias the second subband would be aligned with the variably spaced superlattice resonant transmission path. In this way, under proper infrared illumination and the correct applied bias, the conditions were set for the observation of photon-assisted resonant tunneling [3].

Additional unique observations were made when performing long wavelength infrared spectroscopy of the structure [4]; the experimental results reflected the asymmetry insit in the sample design and the fact that a third subband was located at an energy close to the top of the quantum well. We were able to observe both a breakdown of the parity selection rules and the operation of the structure as an infrared detector around 5 μm.

5.2 Infrared spectroscopy of the VSSEF structure

The conduction band diagram of the structure, including the quantum well and the VSSEF barriers is shown in Figure 5.2. The sample was designed so that under an applied bias of 5.4 Volts the second subband in the quantum well is aligned with the quasibound states in the barrier. The energy difference between the first and second subband were designed to correspond to a wavelength of 9.6 μm, to allow for

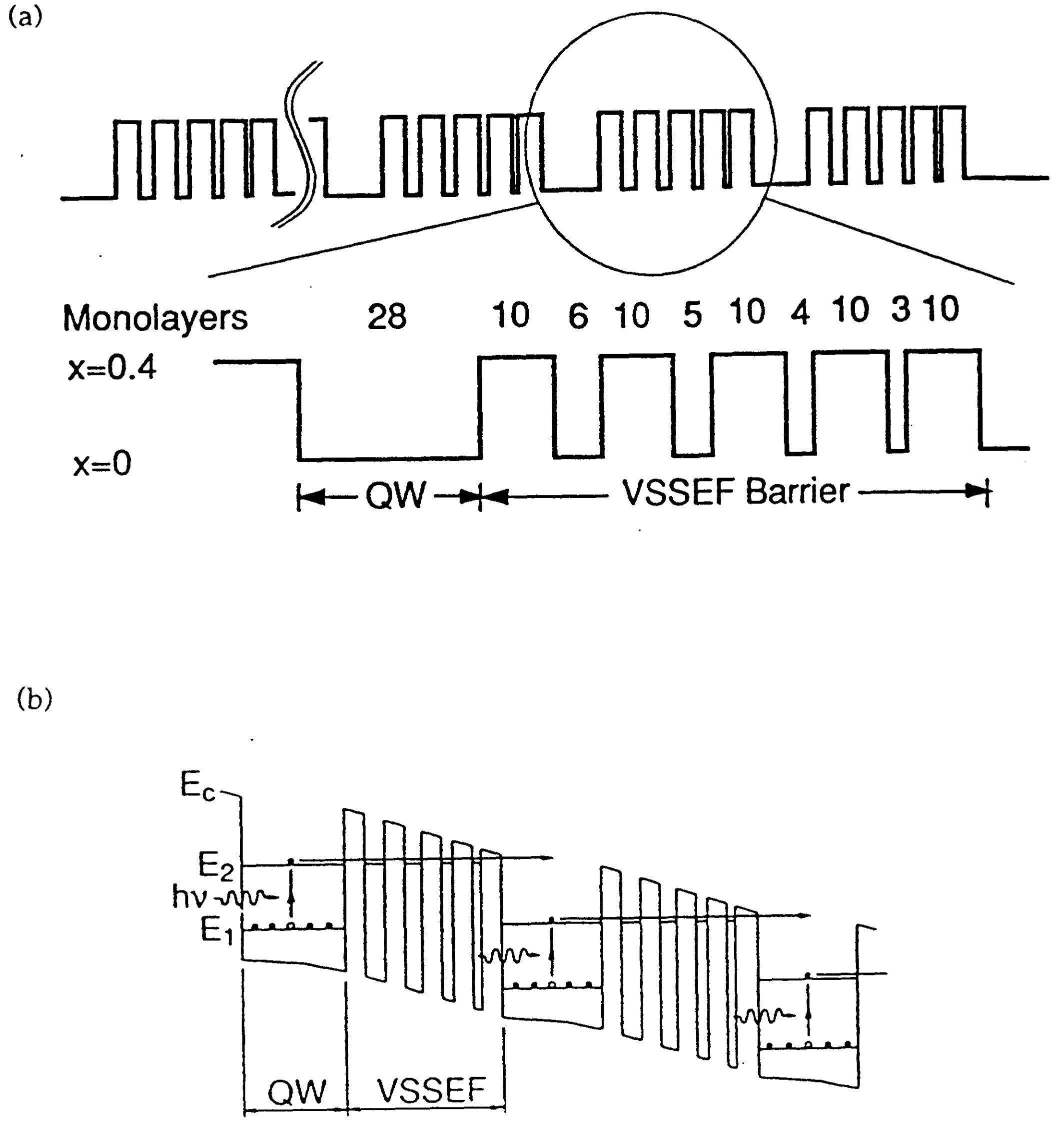

Figure 5.2. Conduction-band diagram of the asymmetrically structured $Ga_{0.6}Al_{0.4}As$/GaAs superlattice (a) at zero bias. Enlarged is one period of the structure with the number of monolayers grown. (b) for the applied voltage which aligns all the quasibound levels in the wells.

excitation by a CO_2 laser.

The structure, grown by molecular beam epitaxy on a GaAs substrate, consisted of 30 quantum wells separated by VSSEF barriers. The entire superlattice was clad on top and bottom by n-doped GaAs contact layers. The center of each of the 28 monolayer thick (=78Å) quantum wells was doped with Si donors, leaving 10 Å undoped next to the adjacent barriers. The average doping in the wells was 1.5x 10^{18} cm^{-3}.
The calculated Fermi energy at 0 ^{O}K is ~44meV from the ground state of the doped quantum well.

Devices were fabricated by etching 100 μm diameter mesas, 2 μm high. The edge of the device chip was polished at 45^{O} to allow light to enter the structure in compliance with polarization selection rules as explained in chapter 3.
The device chip was cemented to a copper block and the whole assembly was mounted in a cryostat for long wavelength infrared photocurrent spectroscopy; this measurement was performed with the technique describe in chapter 3, wherein our device is chosen as the front end detector of an FTIR system. The photoresponse spectrum was then normalized to the flat response of a pyroelectric detector. The absorption spectrum at room temperature was also measured on a planar waveguide, polished at 45^{O} at both ends of the slab, again as described in chapter 3. It was taken using an IR polarizer, and the absorbance value was evaluated as $\log_{10}(T_-/T_+)$ where T_- and T_+ are the transmission taken with the polarizer aligned parallel and normal to the growth direction, respectively.

In this type of room-temperature absorption measurements, the Si impurity band is not expected to introduce any additional components in the absorption spectra. At room temperature most of the donors are ionized as determined from Fermi statistics, thus the room temperature absorption is dominated by the excitation of free electrons. Furthermore, from previous intersubband absorption measurements of heavily doped multi quantum well structures with a single excited level, a single absorption peak was measured, at mid infrared wavelengths, even at low temperatures [5-8].

The experimental results are shown in Figure 5.3. Let us discuss the origin of the peaks observed in the absorption measurements [Figure 5.3(a)]. Consider first transitions to states that exist also in a flat-barrier symmetrical quantum well (FBSQW). The first of these is the allowed transitions, marked e1-e2 in Fig. 5.3(a). The state e3 exists also in a FBSQW but the transition e1-e3 is forbidden by parity selection rules; it becomes allowed here due to symmetry-breaking [9-11]. This transition is indeed dominant in the photocurrent spectrum of Fig. 5.3(b). However, it is difficult to unambiguously identify it in the absorption spectrum of Fig.5.3(a). The temperature difference between the two spectra cannot contribute to a subband energy shift of more than 4 meV or to a substantial broadening [8]. Also our photoresponse data show that this transition is relatively insensitive to the applied bias, in agreement with our calculations. Therefore, the electric field difference cannot account for an energy shift of the e1-e3 transition. Instead, transition e1-e3 in the absorption spectrum is obscured by a broad shoulder which originates from e1 electrons undergoing transitions into the Γ continuum of the $Ga_{0.6}Al_{0.4}As$ barrier.

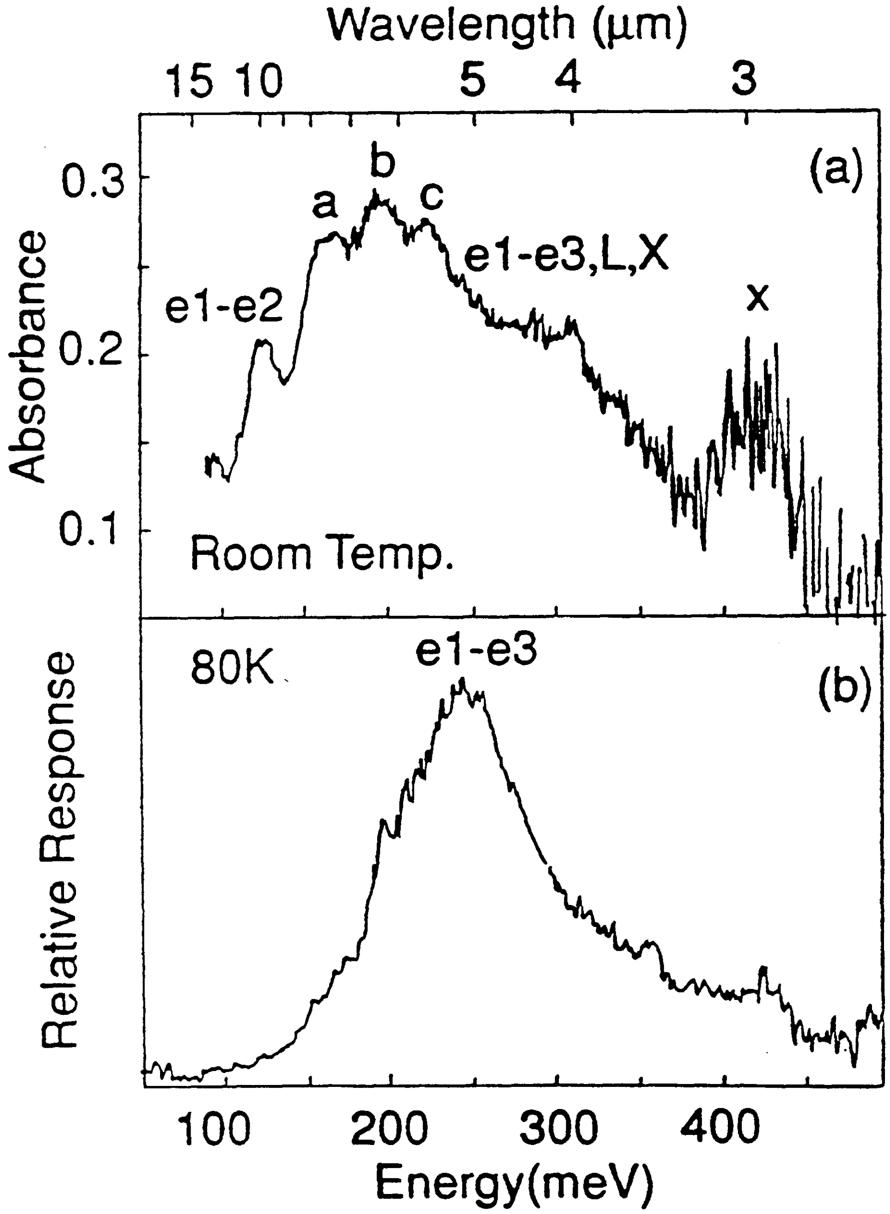

Figure 5.3. (a) Measured absorbance vs photon energy taken at room temperature using the planar waveguide slab geometry. (b) Measured photocurrent spectral response at a bias of 4V, at 80 K.

The fact that the e1-e3 transition dominates the photocurrent spectrum is explained as follows. State e3 is loosely bound and with an electric field it is "pushed" into the continuum. Therefore, only electrons excited to e3 can propagate toward the positive electrode without tunneling hindrance. (Only at the resonant aligning voltage of 5.4 Volts is the tunneling transport path resonant). Similar elimination of tunneling in FBSQW detectors produces high D* detectors [12]. Our results, therefore, suggest that when using an asymmetrical structure, it is possible to achieve 5 μm detection with GaAs/AlGaAs multi quantum well structures, thus expanding to lower wavelengths the useful range. This was only a demonstration of principle, since the design and the growth was not optimized for detector action and the dark currents at 4 V ranged from 50 μå at 20 K to ~1 mA at 80 K, which is too high for the detector to be considered practical.

Continuing our review of the peaks in the absorption spectrum of Fig. 5.3(a) we note transitions marked a, b, c. They are unique to this structure and can be explained with the model described below; they represent the excitation of electrons from the ground e1 subband to special new subbands whose wavefunctions are localized mainly in the superlattice barriers.

5.3 Model and calculations of energy levels

We have used Airy functions in the transfer matrix formalism to calculate the wave functions and energy levels of the structure under electric field [13]. In the calculation we used an energy-dependent effective mass to account for the non-parabolic effective mass in the quantum wells (as described in chapter 3):

$$m^*_{w,np}(E) = m_w + 0.0436\,E + 0.236\,E^2 - 0.147\,E^3 \qquad (5.1)$$

where m_o and m^*_{QW} are the free-electron mass and the energy-dependent effective mass in the quantum well respectively. Here the electron energy E is measured from the bottom of a particular QW and not from a fixed point of reference of the structure. The electron effective mass in the barrier is given by

$$m^*_b = m^*_w + 0.083\,x \qquad (5.2)$$

where x is the barrier Al percentage content. We have used here a conduction-band offset of $\Delta E_C = 323\ meV$ for $x = 0.4$. In order to take screening into account, we used a layer dependent electric field such that the bias potential is dropped equally across all layers except for the doped layers, where the field is minimal. Using this approach, we calculated states confined to a 19-layer structure as shown in Figure 5.4; i.e., we required the decay of the electron wave-function to the left and to the right of one barrier- quantum well- barrier composition as boundary conditions, thus ignoring the periodicity of the test structure.

In general, the Schroedinger equation for the motion of electrons perpendicular to

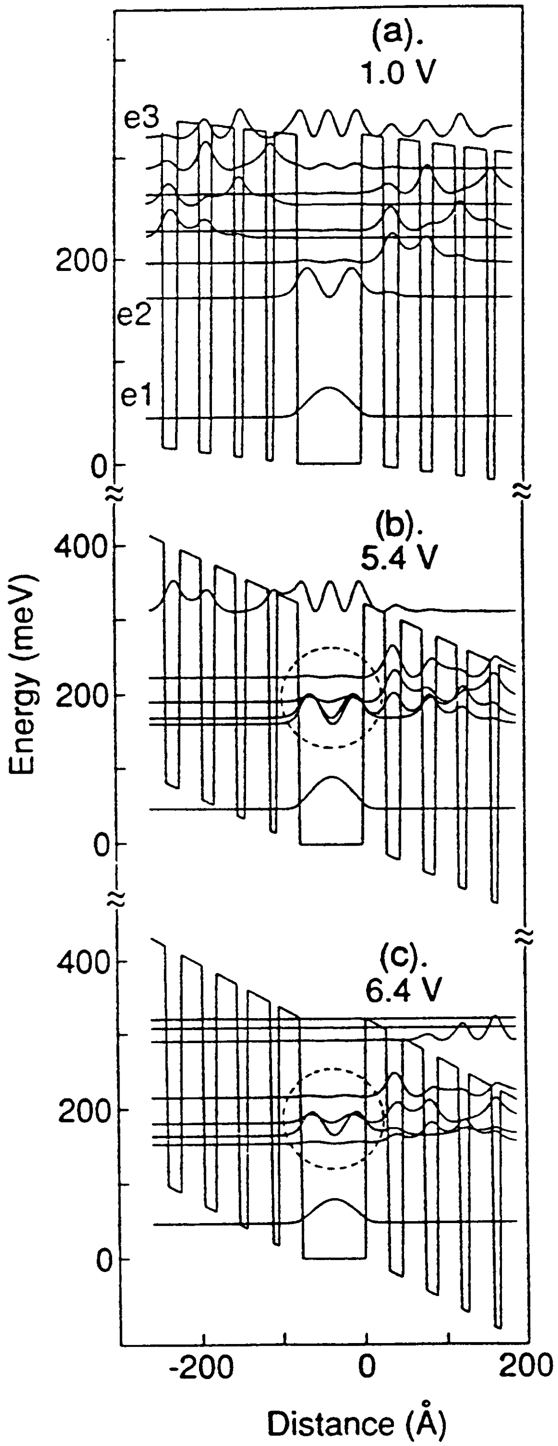

Figure 5.4. Band diagram of a section of the multi-quantum well structure, and its squared wave functions as calculated for 3 different bias voltages.

the layers in the presence of an electric field F is, for layer j with a potential V_j , is [13]

$$-\frac{\hbar^2}{2m_j}\frac{d^2}{dz^2}\Psi - (E - V_j - eFz)\Psi = 0 \tag{5.3}$$

(for holes the field term has a reverse sign). Upon transformation to a dimensionless coordinate Z_j , defined as

$$Z_j = -\left[\frac{2m_j}{(e\hbar F)^2}\right]^{1/3}(E - V_j - eFz) \tag{5.4}$$

one can recast eq. 5.3 in the form

$$-\frac{d^2}{dz^2}\Psi(Z) - Z\Psi(Z) = 0 \tag{5.5}$$

which is the Airy equation with solutions

$$\Psi(Z) = aAi(Z) + bBi(Z) \tag{5.6}$$

where $Ai(Z)$ and $Bi(Z)$ are the Airy functions. The matching conditions at each interface, taken as the continuity of Ψ and $m^{-1}(d\Psi/dZ)$, lead to the matrix relation

$$\begin{pmatrix} \mathrm{Ai}(Z_j^+) & \mathrm{Bi}(Z_j^+) \\ m_j^{-2/3}\,\mathrm{Ai}'(Z_j^+) & m_j^{-2/3}\,\mathrm{Bi}'(Z_j^+) \end{pmatrix} \begin{pmatrix} a_j \\ b_j \end{pmatrix} = \begin{pmatrix} \mathrm{Ai}(Z_{j+1}^-) & \mathrm{Bi}(Z_{j+1}^-) \\ m_{j+1}^{-2/3}\,\mathrm{Ai}'(Z_{j+1}^-) & m_{j+1}^{-2/3}\,\mathrm{Bi}'(Z_{j+1}^-) \end{pmatrix} \begin{pmatrix} a_{j+1} \\ b_{j+1} \end{pmatrix} \tag{5.7}$$

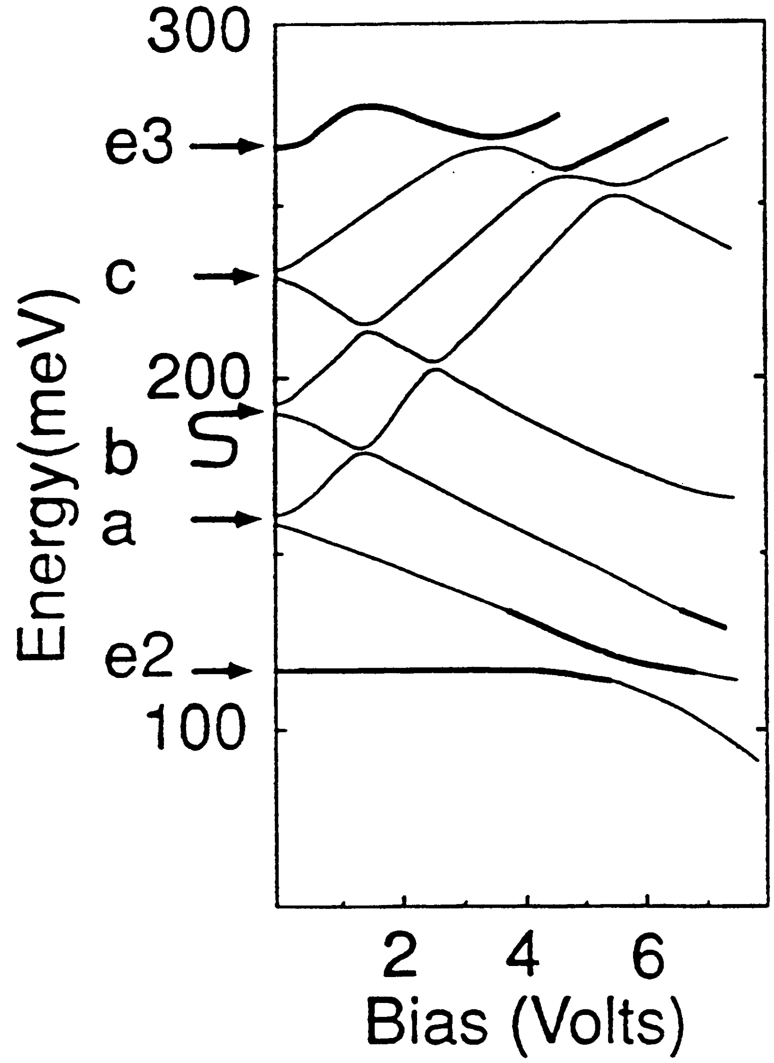

Figure 5.5. The dependance of the calculated confined states on the electric field expressed as the bias voltage across the device. Energy is measured relative to the ground state e1. States with significant dipole moment with the ground state are marked with thick lines.

Z_j , and Z_{j+1} are the coordinate Z evaluated for the j-th and (j+1)-th layers, respectively, at the boundary between them.

There are two means of determining the energies in a quantum well structure: a direct Airy function solution, which becomes exact only for an infinite square well, and a transmission resonance calculation. It has been shown that a very close agreement exist between the two models, when an effective width is chosen for the infinite square well, such that the correct finite square well energies at zero field result [14].

The calculated energies as a function of the external bias (applied across a 30 period structure) are presented in Figure 5.5.

Analyzing the results from Figures 5.4 and 5.5, we find three states that are localized to the thick QW: the ground subband of the system, e1, and two excited subbands, e2 and e3. We also find three pairs of additional subband states, marked at zero bias as a, b, and c. The wave functions of the states which comprise these pairs, for low applied bias (0.1V < Vb < 2.0V), are located either to the left or to the right variably spaced barrier, as depicted in Figure 5.5(a). However, at zero bias the wave function on the left state overlaps the state on the right of the same pair, and due to degeneracy of the left and right VSSEF energies, they split to form a two-state "band." In the test structure there are 30 periods and therefore it should give rise to a 30-state band. Despite the simplicity of the model, it explains the experimental data without adjustable parameters. When compared to the absorption experimental data, the calculated energy difference from the ground subband e1 to subbands a, b, c, e2 and e3 produce an excellent fit to the observed values, as summarized in Table 5.1.

Transition	e1-e2	a	b	c	e1-e3
Observed absorption energy (meV)	124	164	195	225	250-310
Observed photocurrent energy (meV)	...	...	...	...	250
Calculated energy (meV)	117	160	195	232	268

Table 5.1. Calculated and observed long-wavelength infrared transitions

5.4 Photon-assisted resonant tunneling through the VSSEF structure

In order to examine the electronic energy filtering properties of the VSSEF structure, the following experiment was performed by our collaborators. They measured the photocurrent response as a function of the detector bias voltage while exposed to a 1 mW, 9.5-μm CO_2 laser radiation. We can see that, in the framework of our model, such monochromatic illumination assures selective excitation of state e2 up to the crossing voltage, and of the next excited state after crossing (Fig. 5.5). The results,

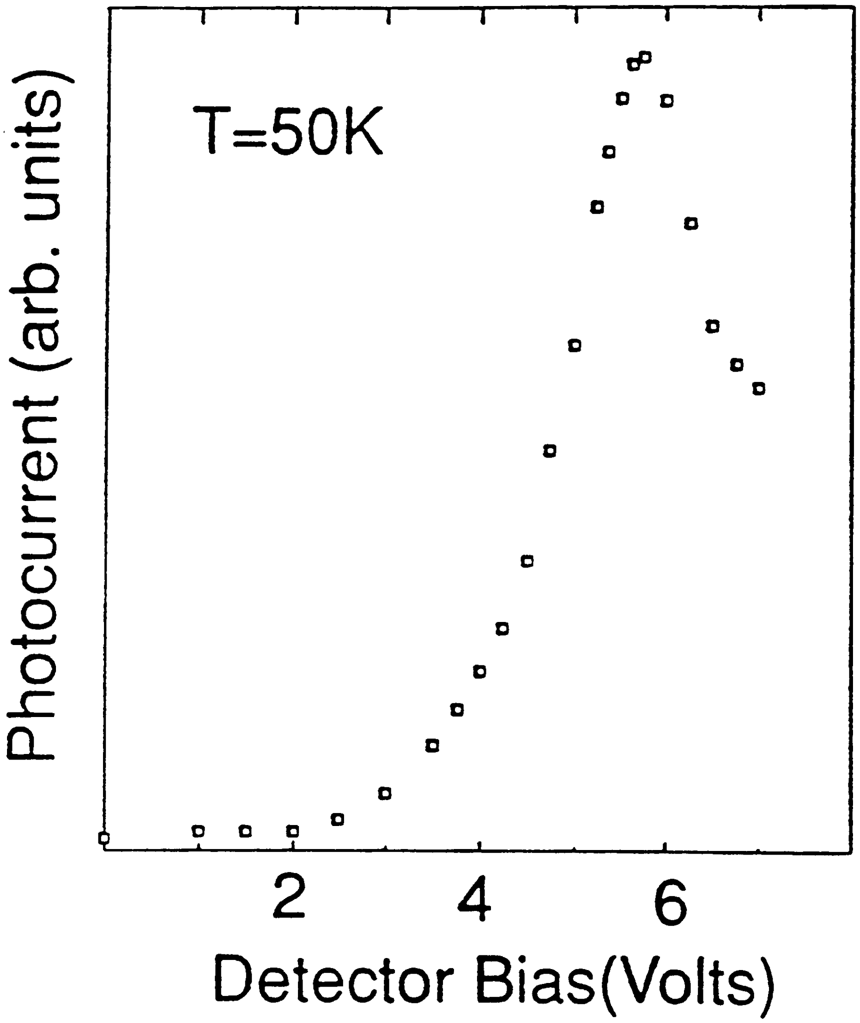

Figure 5.6. Photocurrent response of the device with 9.5 µm CO_2 laser illumination which shows a peak and negative differential conductance of the photon-assisted resonant tunneling.

shown in Fig. 5.6 show a distinct resonance at 5.7 Volts followed by a region of negative differential conductance. This response is qualitatively preserved from low temperatures (~ 10 ^{O}K) to 90 ^{O}K where it smears out. This photoinduced resonant effect stems from the crossing of the first excited state e2 with the second (Fig. 5.5), calculated to occur at ~5.4 V, and is explained as follows.

The photocurrent signal may be viewed as proportional to the electron photoexcitation probability (or oscillator strength) from e1 to e2 and to the probability of an electron to tunnel from e2 to the continuum. In Figures 5.4(b)and 5.4(c) we encircled the wave functions of the states involved at and after the resonance. At low bias, before the onset of a resonant channel [see Fig. 3(a)], the interaction between the excited electron in e2, which is completely localized to the thick QW, and the next excited state, which has a substantial component in the barrier and the continuum, is small. Therefore, a small photocurrent is expected. At the resonance [see Fig.5.4(b)], where the states cross, the mixing becomes large and both have high oscillator strengths for transitions from the ground subband, associated with high tunneling probability to the continuum, and therefore a large photocurrent signal is achieved. After resonance [see Fig. 5.4(c)], e2 becomes a tunneling state but has diminished oscillator strength, whereas the next excited state has high oscillator strength for transition from e1, but has also low tunneling probability, and therefore the photocurrent signal is small again. This result is a direct observation of photon assisted resonant tunneling, and it shows that electrons can be filtered to create a somewhat monochromatic beam.

5.5 Summary and conclusions

We have described in this chapter the experimental study of a multi quantum well structure with variably spaced superlattice barriers. This study included the following:

(i) The observation of photon-assisted resonant tunneling.

(ii) The confirmation of the energy filtering properties of a VSSEF structure.

(iii) The observation of a rich structure of multiple peaks in the infrared absorption measurements, interpreted as transitions from the ground subbands to a set of subbands peculiar to the VSSEF structure; the wavefunctions of these states are mostly localized in the superlattice barrier regions. The wavefunctions and energies of these subbands were calculated with a simple model, and a good fit was found with respect to the experimental results.

(iv) The photocurrent spectroscopy of the sample revealed the dominance of the transition from the ground subband (e1) to the second excited subband (e3). This implies that the parity selection rules are violated; this is not surprising after the realization that each large quantum well, where the carriers are stored, is clad asymmetrically by the superlattice barriers on each side. This asymmetry adds to the one induced by the applied electric field.

(v) The photocurrent spectrum peaked around 5 µm, showing that, in principle, photodetection at lower wavelengths than usually realized can be achieved in the

GaAs/AlGaAs system.

References

[1] C.J. Summers and K.F. Brennan, Appl. Phys. Lett. 48, 806 (1986).

[2] K.F. Brennan and C.J. Summers, J. Appl. Phys. 61, 614 (1987).

[3] A. Larsson, S.J. Borenstain, B. Jonsson, I. Andersson, J. Westin, T.G. Andersson, Appl. Phys. Lett. 58, 1297 (1991).

[4] S.I. Borenstain, I. Gravé, A. Larsson, D.H. Rich, B. Jonsson, I. Andersson, J. Westin, T. Andersson, Phys. Rev. B 43, 9320 (1991).

[5] L.C. West and S.J. Englash, Appl. Phys. Lett. 46, 1156 (1985).

[6] B.F. Levine, R.J. Malik, J. Walker, K.K. Choi, C.G. Bethea, D.A. Kleinman, and J.M. Vandenberg, Appl. Phys. Lett. 50, 273 (1987).

[7] A. Harwit and J.S. Harris, Jr., Appl. Physd. Lett. 50, 685 (1987).

[8] B.C. Covington, C.C. Lee, B.H. Hu, H.F. Taylor, and D.C. Streit, Appl. Phys. Lett. 54, 2145 (1989).

[9] Y.J. Mii, R.P.G. Karunasuri, K.L. Wang, M. Chen, and P.F. Yuh, Appl. Phys. Lett. 56, 1986 (1990).

[10] J.L. Pan, L.C. West, S.J. Walker, R.J. Malik, and J.F. Walker, Appl. Phys. Lett. 57, 1366 (1990).

[11] B.F. Levine, C.G. Bethea, V.O. Shen, and R.J. Malik, Appl. Phys. Lett. 57, 383 (1990).

[12] B.F. Levine, G. Hasnain, C.G. Bethea, N. Chand, Appl. Phys. Lett. 54, 2704 (1989).

[13] D. Campi and C. Alibert, Appl. Phys. Lett. 55, 454 (1989); D.C. Hutchings, Appl. Phys. Lett. 55, 1082 (1989).

[14] D.A.B. Miller, D.S. Chemla, T.C. Damen, A.C. Gossard, W. Wiegmann, T.H. Wood, and C.A. Burrus, Phys. Rev. B 32, 1043 (1985).

Chapter 6

Second-harmonic generation via intersubband transitions

6.1 Introduction

In the last few years there has been an increasing interest in the physics and applications of intersubband transitions in quantum well systems. The main applied research effort has been the understanding and development of intersubband infrared detectors; many topics concerning this subject have been reviewed in the previous chapters, along with the presentation of our work in this field . A second avenue of expanding research deals with optical nonlinearities observable when light in resonance (or close to resonance) with an intersubband transitions is shed on a multi-quantum well sample. For completeness we shall add that additional "intersubband topics" have recently been addressed by research groups around the world: examples are the quest for stimulated emission, and eventually the invention of an intersubband laser; and the study and development of optical mid-infrared modulators .

We shall begin this chapter with a brief review of optical nonlinearities linked to the transitions between the subbands in quantum well systems; then we shall present our work on second harmonic generation. In chapter 7 we shall present our work involving third-order nonlinear effects.

Nonlinear optics is the study of phenomena that occur as a consequence of the modification of the optical properties of a material system by the presence of light, beyond the regime of linear response. A general formalism to describe such phenomena is based on Maxwell's equations

$$\nabla \cdot \mathbf{D} = 4\pi\rho \tag{6.1}$$

$$\nabla \cdot \mathbf{B} = 0 \tag{6.2}$$

$$\nabla \times \mathbf{E} = -\frac{1}{c}\frac{\partial \mathbf{B}}{\partial t} \tag{6.3}$$

$$\nabla \times \mathbf{H} = \frac{1}{c}\frac{\partial \mathbf{D}}{\partial t} + \frac{4\pi}{c}\mathbf{J} \tag{6.4}$$

The fields **E** and **D** are related by

$$\mathbf{D} = \mathbf{E} + 4\pi\mathbf{P} \tag{6.5}$$

P being the polarization vector. Whenever no free charges or currents are present, i.e., $\rho = 0$ and $J = 0$, and assuming nonmagnetic materials, so that $\mathbf{B} = \mathbf{H}$, one can obtain the nonlinear wave equation in the form

$$\nabla \times \nabla \times \mathbf{E} + \frac{1}{c^2}\frac{\partial^2 \mathbf{E}}{\partial t^2} = -\frac{4\pi}{c^2}\frac{\partial^2 \mathbf{P}}{\partial t^2} \tag{6.6}$$

The dipole moment per unit volume, or polarization **P**(t) of the material system depends upon the strength **E**(t) of the applied (optical) field. In the case of conventional optics the relashionship is linear.

$$P(t) = \chi^{(1)}E(t) \tag{6.7}$$

$\chi^{(1)}$ is known as the linear susceptibility. The linear susceptibility is a second rank tensor. In many situations an analysis of the symmetry of the material will reduce and limit the number of nonvanishing tensorial components. Each component is a complex number

$$\chi = \chi' + i\chi'' \tag{6.8}$$

The linear index of refraction is determined by χ' and the linear absorption of light and its saturation are determined by χ''. The real and imaginary part of the susceptibility are related by the Kramers - Kronig relations, which insure causality [1].

Whenever the optical fields involved are strong enough, and sometimes even at moderate fields, due to special material characteristics, the linear regime represented by Eq. 6.7 does no longer represent the physical system with fidelity. The nonlinear optical response can, in many instances be expressed by writing the polarization **P**(t) as a power series in the fields amplitudes

$$\mathbf{P}(t) = \chi^{(1)}\mathbf{E}(t) + \chi^{(2)}\mathbf{E}^2(t) + \chi^{(3)}\mathbf{E}^3(t) + \ldots \tag{6.9}$$

$\chi^{(n)}$ is known as the n-th order nonlinear optical susceptibility. One has to recall that $\chi^{(n)}$ is an (n+1)th rank tensor; that the equation relating the polarizations to the field is a vectorial one, and that $\mathbf{E}^n(t)$ stands for the product of n (possibly different) field amplitudes.

6.2 Second-order susceptibility for multi-quantum well structures

The intersubband second-order susceptibility (ISOS) for second-harmonic generation, as generally with second-order processes associated with discrete states, can be determined from second-order time-dependent perturbation theory [1-3]. It is given by

$$\chi^{(2)}_{2\omega} = \frac{e^3 n}{\varepsilon_o \hbar^2} \sum_{m,n} \langle Z_{1,n} \rangle \langle Z_{n,m} \rangle \langle Z_{m,1} \rangle \left\{ \frac{1}{(\omega - \Omega_{n,1} - i\Gamma_{n,1})(2\omega - \Omega_{m,1} - i\Gamma_{m,1})} + \frac{1}{(\omega + \Omega_{n,1} - i\Gamma_{n,1})(2\omega + \Omega_{m,1} - i\Gamma_{m,1})} - \right\}$$

$$\left\{ -\frac{1}{(2\omega - \Omega_{m,n} - i\Gamma_{m,n})} \left[\frac{1}{(\omega - \Omega_{m,1} - i\Gamma_{m,1})} + \frac{1}{(\omega + \Omega_{n,1} - i\Gamma_{n,1})} \right] \right\} \tag{6.10}$$

where $\langle Z_{1,j} \rangle$ is the dipole matrix element between state i and j, $\Omega_{i,j}$ are the frequencies corresponding to the energy differences among levels i and j in the well, $1/\Gamma_{i,j}$ are the dephasing times, e is the electronic charge and n is the density of carriers; we assume that only the lowest energy level is thermally populated.

Gurnick and DeTemple were the first to note, in 1983, that the large dipole matrix element involved with intersubband transitions could be associated with large values of the nonlinear susceptibilities [4].

It is clear that, as for any centosymmetric material, the ISOS vanishes for a perfectly symmetrical quantum well. This is embedded in the formalism of Eq. 6.10, since all matrix dipole terms, linking the ground subband to another odd stubband, vanish due to parity selection rules. To observe second-order effects, one has to brake the symmetry of the material: in the case of quantum well systems this can be done with a variety of methods.

One possibility is the application of an electric field across the sample in the direction of the growth, the z direction [5]. This bends the bands and introduces the needed asymmetry. When a dc field F is present, the matrix element between states of same parity is not vanishing. For example, in the limit of an infinite quantum well, these nonvanishing matrix elements between subbands of the same parity are given, to first order in the bias Φ, by [6]

$$\langle Z_{n,m} \rangle = \frac{(-1)^{(n+m)/2}}{\pi} \frac{m^2 + n^2}{n\,m\,(m^2 - n^2)^2} \Phi d \tag{6.11}$$

where $\Phi = eFd/\pi E_0$ is the (normalized) bias and $E_0 = \pi^2 h^2 / 2 m_w d^2$ is the characteristic confinment energy; d is the width of the well; m_w is the effective mass in the well.

Second-harmonic generation via intersubband transitions, was first observed by Fejer et al. [6]; the symmetry in their multi-quantum well sample was broken by the application of a dc electric field as discussed above; from the measurements of the second harmonic at a wavelength around 5 µm, they reported a value for the second-order susceptibility of 28nm/V, which is 78 times larger than for bulk GaAs.

A more efficient method, which potentially can yield larger second-harmonic power generation, is to make use of an insit configurational, or compositional, asymmetry [7,8]. The original prediction in Ref. 5 used, for the calculations, an asymmetric Morse potential. A more practical model, easily realizable by state-of-the-art epitaxial growth techniques, is obtained by designing a stepped quantum well [9] . This kind of well is shown in Figure 6.1. The well is clad by two barriers of $Al_xGa_{1-x}As$; the well itself includes a GaAs layer a few nanometers wide, followed by an $Al_yGa_{1-y}As$ layer , with $y<x$. The doping could be in different positions in the well or in the barriers.

This configurational asymmetry insures that the $1\mapsto3$ transition has a non-vanishing dipole matrix element. Another big advantage is that, with proper design, one can have both the $1\mapsto2$ and the $2\mapsto3$ transitions resonant with the pump wavelength, a task not achievable with a symmetric quantum well, where, as well known from basic quantum mechanics, the energy level separation increases for higher levels and, in the limit of an infinite potential quantum well, the energy levels go like the square of the integer that counts the levels from the bottom of the

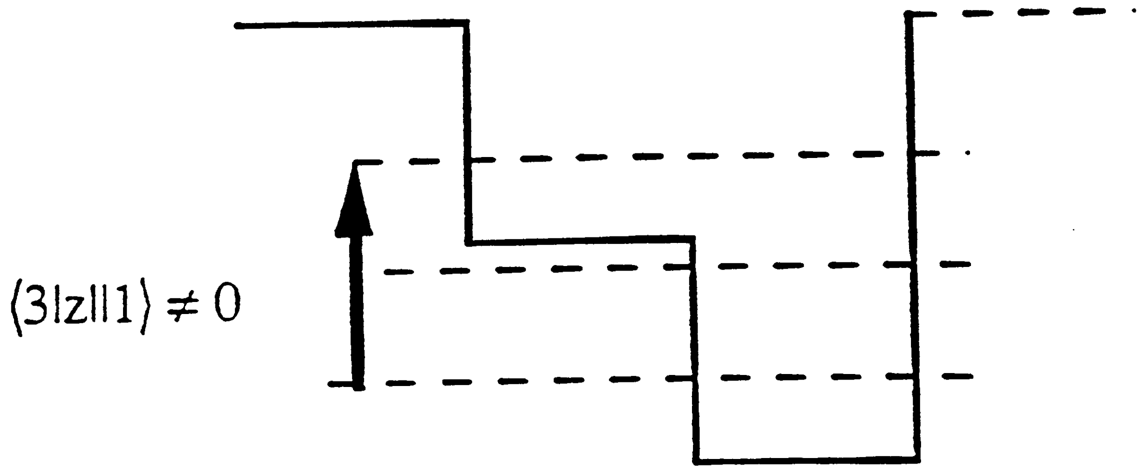

Figure 6.1. The conduction-band scheme of a stepped quantum well. Since the structure is not symmetric, the dipole matrix element between subbands 1 and 3 (or any other odd-parity or even-parity pair of subbands) is not vanishing. Another advantage is the possibility of designing equispaced subbands, which sets up a double-resonance configuration.

well. Due to these considerations more than an order of magnitude can be gained for the ISOS in configurationally asymmetric quantum wells with respect to the biased symmetrical well. These considerations about the stepped quantum well system were experimentally verified, and values approaching 7×10^{-7} m/V were inferred for the ISOS from measurements of second-harmonic generation [9]. Optical rectification, another second-order effect, has also been measured in stepped quantum wells [10] and in asymmetric coupled quantum wells [11] and, again, large enhancements over bulk values were observed. Second-harmonic generation via intersubband transition has been observed also in different material systems [12].

It is worthwhile noting that the ISOS in symmetric, biased quantum wells is not a monotonic function of the applied field: for fields strong enough an optimum can sometimes be achieved when the symmetry is strongly broken and, at the same time, Stark shifts tend to bring the system as close as possibly to a double resonance process; from the practical point of view this requires designing the energy level separations to fit the pump wavelengths for the deformed, final, optimal configuration rather than for the unbiased quantum well. In stepped quantum wells or in additional systems, such as, for example, asymmetric, coupled, double quantum wells, the application of an external field can be used to fine-tune the second-harmonic resonance to the configuration yielding maximum efficiency [13].

Our first experiments to generate second harmonic in both biased, symmetric systems and configurational asymmetric samples used the front illumination, Brewster angle geometry. Later on, our main efforts reverted to show the feasibility of second-harmonic generation in samples with longer interaction lengths [14]. Typically, in the Brewster angle geometry, the length of the active multiquantum well region is of the order of 1 μm, so that no real problem arises due to phase matching and absorption. By increasing the interaction length, for example in a multipass waveguide geometry or in a side-entrance geometry, one could hope to generate higher second-harmonic power. However the detection or utilization of higher second-harmonic power would be impaired in samples with longer interaction length by the problems of phase matching and absorption.

Due to dispersion one has $\Delta k = k^{2\omega} - k^{\omega} = (2\omega/c)[n(2\omega)-n(\omega)] = 0$. Hence, the effective contribution to SHG is limited to a somewhat short coherence length $L_c = 1/\Delta k$. One way to circumvent this would be to resort to quasi-phase matching [15], by taking advantage of the sensitivity of the ISOS to an external electric field. By applying a periodically alternating field along the direction of propagation one can spatially modulate $\chi^{(2)}$ with a period Λ. By choosing $1/\Delta k = \Lambda$ we get quasi-phase matching condition $\Delta k_{eff} = \Delta k - \Lambda = 0$.

The absorptions of the pump and of the SHG also play an important role. In particular, near resonance, the intersubband absorption of these optical fields is fairly large. Under most practical situations the oscillator strength for the $1\mapsto 2$ transition is larger than the one for the $1\mapsto 3$ transition, in the stepped quantum well system. Thus one can assume $\alpha^{\omega} >> \alpha^{2\omega}$. The expression for the absorption coefficients can be written as

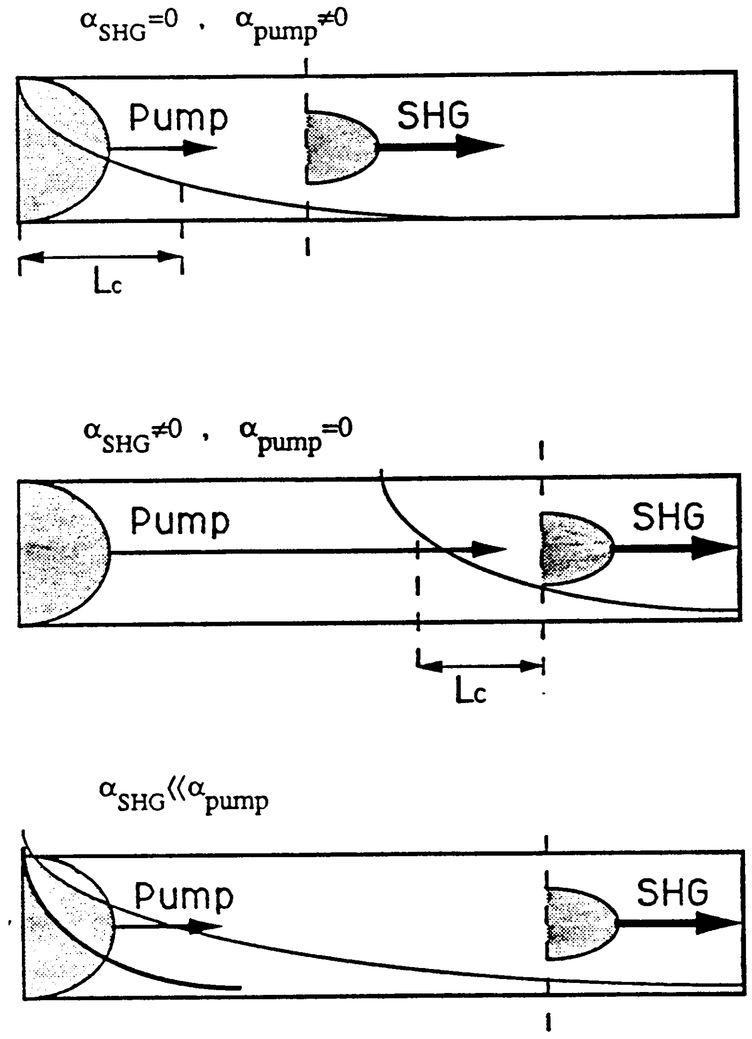

Figure 6.2. The effects of absorption, both of the pump and of the generated second harmonic are displayed for three different scenarioes in a long sample. In each case the effective range for efficient generation and collection of second-harmonic generation is shown.

$$\alpha_{i,j} = e^2 \sqrt{\frac{\mu_o}{\varepsilon}} \left|\langle Z_{i,j} \rangle\right|^2 n \frac{\Gamma_{i,j}\,\omega}{(\Omega_{i,j} - \omega)^2 + \Gamma_{i,j}^2} \tag{6.12}$$

Figure 6.2 sketches a number of possible situations for different absorption strengths of pump and SHG beams. It is clear that to benefit of larger conversion efficiency one has to consider not only phase matching, but also absorption problems.

By taking into account the effects of phase matching and absorption of both fundamental (pump) and second harmonic, the efficiency of SHG can be approximated by

$$\frac{P^{2\omega}}{P^{\omega}} = 8\left(\frac{\mu}{\varepsilon_o}\right)^{3/2} \varepsilon_o^2 \omega^2 \frac{\left|\chi_{(2\omega)}\right|^2}{n^3} \left[\frac{P^{\omega}}{\text{Area}}\right] \frac{e^{-\alpha_{(2\omega)} z}}{\Delta k^2 + \left(\alpha_{(\omega)}\right)^2} \tag{6.13}$$

In the regime where $\Delta k << \alpha^{\omega}$ one can see that a coherent contribution to the SHG is limited to an effective length $1/\alpha^{\omega}$, while the length of the device should not exceed $1/\alpha^{2\omega}$ for an efficient conversion.

6.3 Experimental results

The sample used was an asymmetrically stepped QW, grown by MBE, consisting of a 60 Å GaAs layer followed by 40 Å $Al_{0.1}Ga_{0.9}As$ clad by 300 Å $Al_{0.4}Ga_{0.6}As$ barriers. A similar sample was used by Rosencher et al. [8]. The doping concentration is

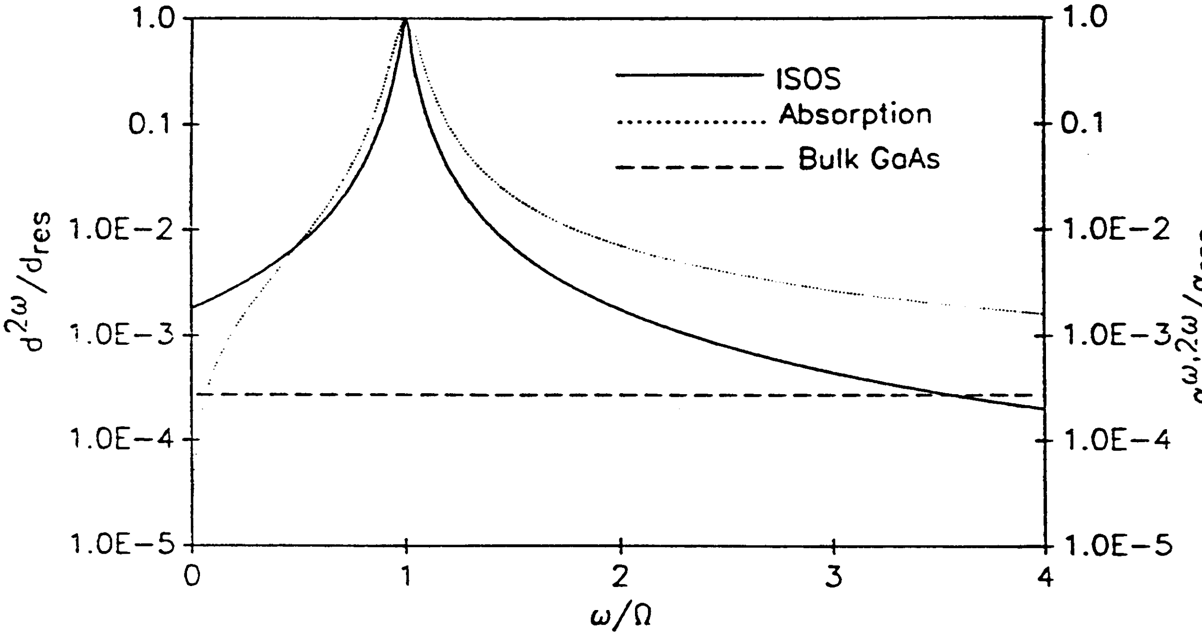

Figure 6.3. The normalized calculated second-order susceptibility (solid line) and the intersubband absorption (dashed line), as a function of the normalized frequency.

$1\times10^{18}\,cm^{-3}$, applied to the deeper well. The structure is designed so as to exhibit three confined levels with approximately equal energy spacings, $\hbar\Omega \approx E_{32} \approx E_{21} \approx 115meV$, corresponding to a transition wavelength of 10.8 μm.

By inserting these values, together with the calculated values of the matrix dipole elements), as well as the value of the carrier density and the measure of the linewidth of the states, taken to be $\Gamma = 7$ meV, one can calculate the ISOS from Eq. (6.10), or from its approximation which neglects nonresonant terms, when appropriate. This is shown in Figure 6.3, together with the shape of the absorption linewidth and the value of the ISOS for bulk GaAs .

It is worthwhile noting that the linewidth of the absorption is somewhat broader than the linewidth of the second harmonic generated. This is understood by analyzing Eq. (6.10), compared to Eq. (6.12). This issue has also been verified experimentally [16].

The experimental set-up for the generation and monitoring of second harmonic generation is described in Figure 6.4. The intensity of the SHG was measured by using a CO_2 laser chopped at 325 Hz, together with a Mercury-Cadmium-Telluride detector in a standard lock-in detection technique. A sapphire window was used to block the CO_2 laser wavelength at 10.6 μm, while a second narrow-band filter ensured that only the SHG was detected.

In Figure 6.5 the intensity of the SHG, as a function of the pump level, is shown for a sample 500 μm long, used in the side-entrance geometry. The quadratic dependence expected for second-order effects is observed. Figure 6.6 displays the

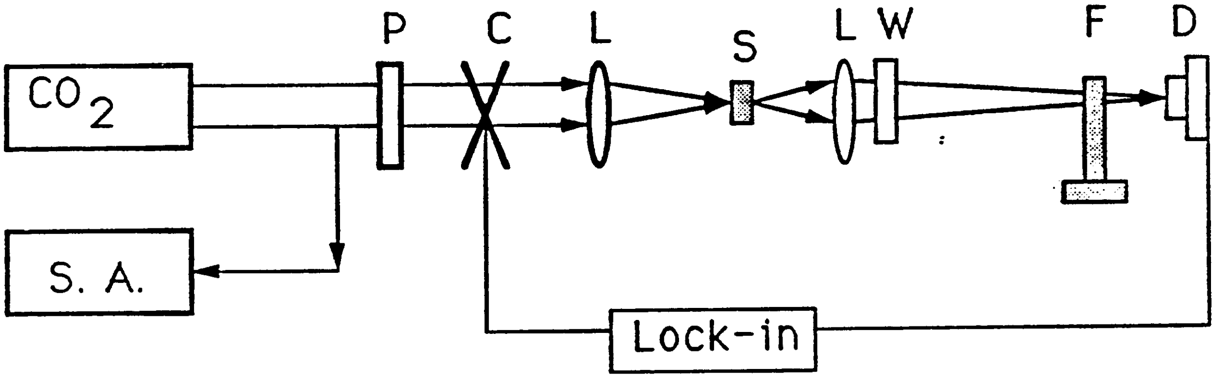

Figure 6.4. The experimental set-up for the measurements of second-harmonic generation. The infrared light, generated by a tunable CO_2 laser, and checked by a spectrum analyzer (S.A.) is polarized (P), chopped (C), focused onto the sample S by a lens (L). A second lens (L) collects the light after the sample. A sapphire window (S) and a narrow-band filter centered at the second harmonic insure a complete filtering of the pump signal. The double filter arrangement prevents also heating effects. The detector D is inserted in a standard lock-in technique.

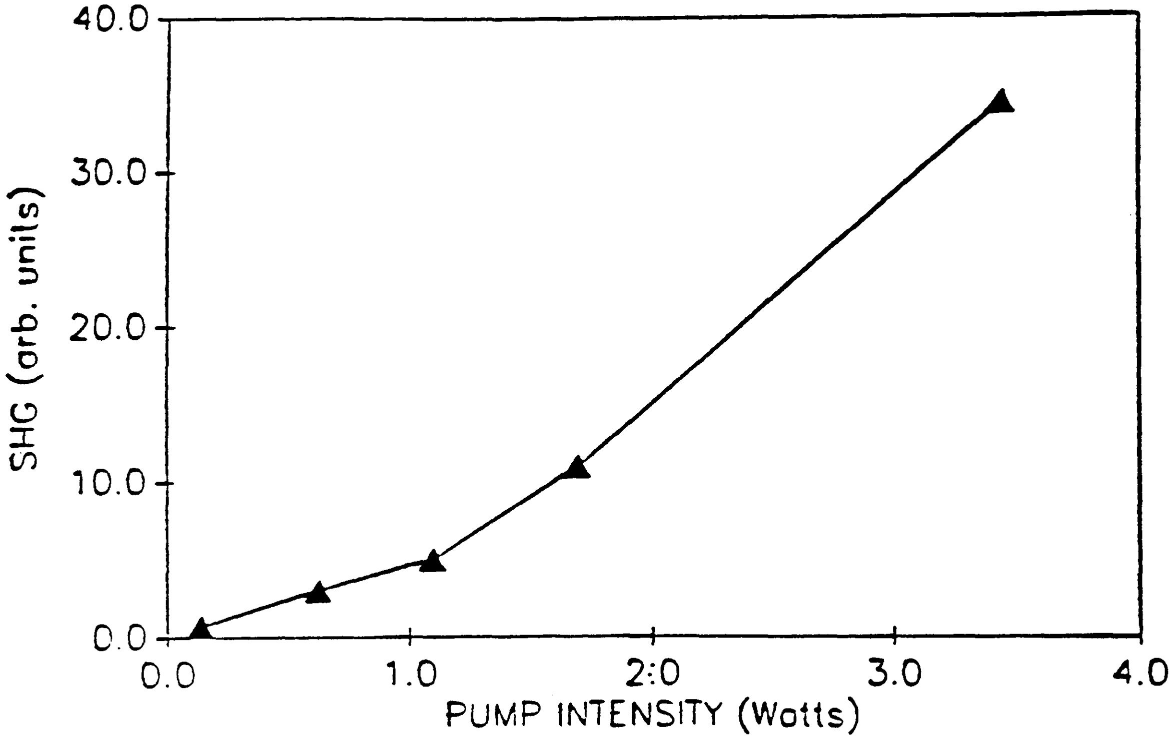

Figure 6.5. The intensity of the second harmonic generated as a function of the pump level in a long sample (500 μm).

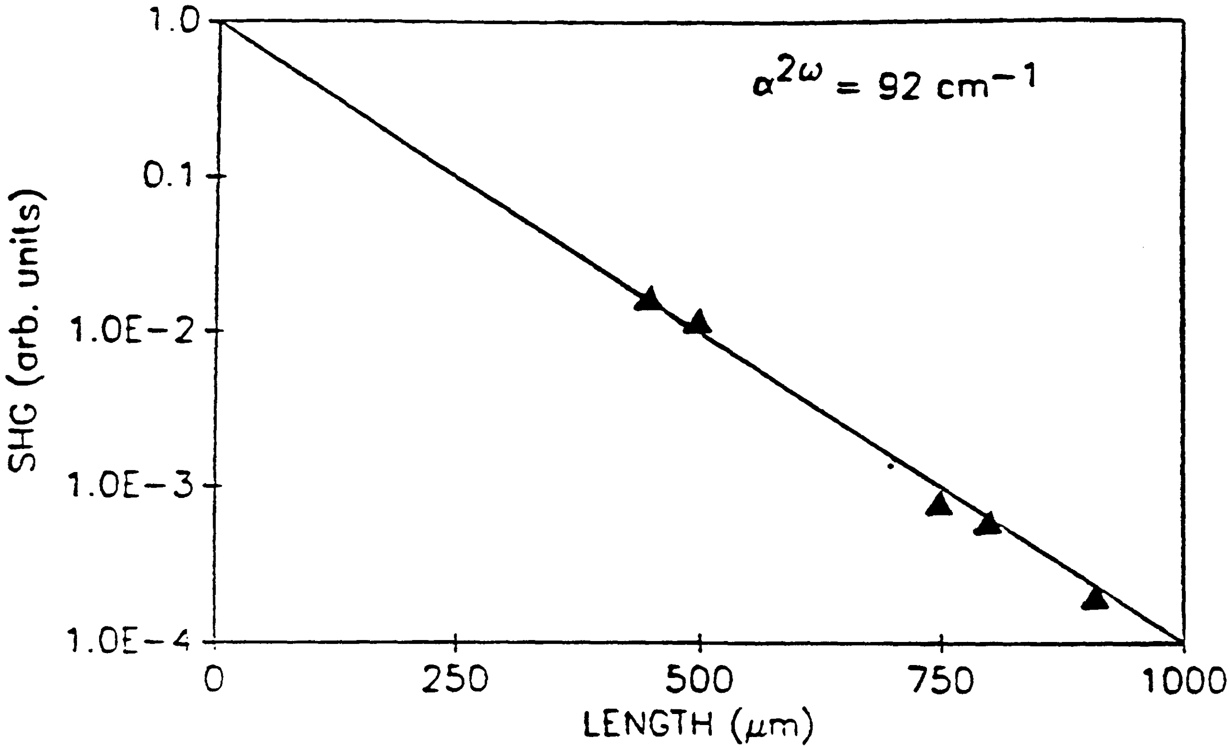

Figure 6.6. The intensity of the second harmonic generated as a function of the interaction length. Pump power is 3.5 W.

measured intensity of the SHG as a function of sample length. The exponential dependence is an indication that absorption processes are dominant. From the experimental results we estimate the value of $\alpha^{2\omega}$ to be 92 cm^{-1}.

6.4 Conclusions

We have presented in this chapter a review of second-harmonic generation via intersubband transitions and the details of our experiments, in which, for the first time, second-harmonic generation was obtained in long samples. We also discussed the effects of absorption of both the fundamental and the harmonic, as well as the issue of phase matching, for various configurations.

References

[1] A. Yariv: "Quantum Electronics," 3rd ed., J. Wiley & Sons .

[2] R.W. Boyd: "Nonlinear Optics." Academic Press.

[3] P.N. Butcher and D. Cotler: "The Elements of Nonlinear Optics," Cambridge University Press.

[4] M.K.Gurnick and T.A. DeTemple, IEEE J. Quantum Electron., QE-19, 791 (1983).

[5] Z. Ikonic, V. Milanovic and D. Tjapkin, IEEE J. Quantum Electron., QE-25, 54 (1989).

[6] M.M. Fejer, S.J.B. Yoo, R.L. Byer, A. Harwit and J.S. Harris, Jr., Phys. Rev. Lett. 62, 1041 (1989).

[7] J. Khurgin, Appl. Phys. Lett. 51, 2100 (1987).

[8] J. Khurgin, Phys. Rev. B 38, 4056 (1988).

[9] E. Rosencher, P.Bois, J. Nagle and S. Delaitre, Electron. Lett. 25, 1063 (1989).

[10] E. Rosencher, P.Bois, J. Nagle , E. Costard and S. Delaitre, Appl. Phys. Lett. 55, 1597 (1989).

[11] E. Rosencher, P.Bois, B. Vinter, J. Nagle , and D. Kaplan, Appl. Phys. Lett. 56, 1822 (1990).

[12] C. Sirtori, F. Capasso, D. L. Sivco, S.N.G. Chu and A.Y. Cho, Appl. Phys. Lett. 59, 151 (1991).

[13] C. Sirtori, F. Capasso, D. L. Sivco, A.L. Hutchinson and A.Y. Cho, Appl. Phys. Lett. 60, 151 (1992).

[14] A. Sa'ar, I. Gravé, N. Kuze and A. Yariv, Proceedings of the Topical Meeting NLO'90 on Nonlinear Optics, Hawai, p.113 (1990).

[15] S. Somekh and A. Yariv, Appl. Phys. Lett. 21, 140 (1972).

[16] P. Boucaud, F.H. Jùlien, D.D. Yang, J-M. Lourtioz, E. Rosencher, P. Bois and J. Nagle, Appl. Phys. Lett. 57, 215 (1990).

Chapter 7

Third-order non-linear effects via intersubband transitions

7.1 Introduction

Following the description, in the previous chapter, of our work on second-order nonlinear effects via intersubband transitions, we present in this chapter our work on third-order nonlinearities induced by the same transitions.

One of the motivations to deal and study third-order nonlinearities near an intersubband resonance is the fact that the very large dipole moment of the transition contributes to the n-order susceptibility as a factor to the n-th power. This means that if large enhancements of $\chi^{(2)}$ have been observed in experimental work on second-order effects (a factor of 100 - 1000 over corresponding bulk values), one could expect also large enhancements for $\chi^{(3)}$.

In addition, third-order effects include a number of interesting and useful phenomena, which allow for different applications, possibly for on-chip optical signal processing. The state of the art in research and technology, at this time, is not yet capable of taking full advantage of these possibilities in the mid-infrared region, in the same way as it has been happening for the visible and near infrared domains. Still, the demonstration of good quality detectors and the observation of strong nonlinear effects, all in the easily integrable and technologically mature III - V material systems, open the way for many applications. The eventual development of coherent powerful sources in the mid-infrared, based on the same materials (viz. an intersubband laser), could bring in a new set of integrated devices that will support new applications and expand system flexibility and performances in the thermal imaging domain.

7.2 Third-order nonlinear susceptibility

The third-order contribution to the nonlinear polarization is given by

$$P^{(3)}(t) = \chi^{(3)}E^{3}(t) \tag{7.1}$$

The applied optical field that induces the polarization can consist, in principle, of up to three different frequency components, and the resulting expression for the third-order polarization could then contain up to 44 different frequency components, considering both positive and negative frequencies. In addition to that, one has to recall that $\chi^{(3)}$ is a fourth-rank tensor, and that the final number of independent non-vanishing components depends on the symmetry of the crystal. However, in view of the structure and dimensionality of the intersubband transition in quantum wells, we are mainly interested in $\chi^{(3)}{}_{3333}$; it is clear that the enhanced nonlinearity is expected in the confinement direction.

Moreover, at this stage our experimental work was focused on the observation of nonlinear effects linked to the intensity-dependent refractive index, and the applied field could be considered to be monochromatic, for all practical purposes. For a monochromatic applied field of the form

$$E(t) = E_O \cos\omega t \tag{7.2}$$

considering that $\cos^3\omega t = 1/4 \cos 3\omega t + 3/4 \cos\omega t$, Eq. 7.1 will take the form

$$P^{(3)}(t) = \frac{1}{4}\chi^{(3)} E_o^3 \cos 3\omega t + \frac{3}{4}\chi^{(3)} E_o^3 \cos\omega t \tag{7.3}$$

The first term describes a response at frequency 3ω, i.e., it describes the process of third-harmonic generation. The second term in Eq. 7.3 represents the nonlinear contribution to the polarization at the same frequency as that of the applied field. The effect is usually represented by writing the refractive index in the form

$$n = n_o + n_2 I \tag{7.4}$$

n_0 being the linear refractive index, while

$$n_2 = \frac{12\pi^2}{n_o^2 c}\chi^{(3)} \tag{7.5}$$

and I is the intensity of the optical incident wave, $I = (n_o\, c/8\pi)E_o^2$.

7.3 The dc Kerr effect

In this section we report on the first observation of third-order intersubband nonlinearities via intersubband nonlinearities. We chose to start our study on third-order intersubband nonlinearities via the dc Kerr effect; this can be done in a relatively simple experimental configuration. This work was the fruit of a collaboration with A. Sa'ar. The author's contributions included the suggestion and drive to study third-order processes, the design, growth and optimization of MBE samples, the preparation and characterization of the samples through absorption spectroscopy, and the experimental set-up. The actual experimantal data were recorded in the author's absence.

The electrooptic effect is the change in the refractive index of a material induced by the presence of a dc (or low-frequency) electric field. For materials that do not possess centro-inversion symmetry, the dominant term in the change of the refractive index is linear with the amplitude of the applied electric field (linear electrooptic or Pockels effect). For centrosymmetric materials, such as a square quantum well, the lowest-order change in the refractive index depends quadratically on the strength of the applied dc field. This is the dc Kerr effect or quadratic electrooptic effect (QEE).

The QEE was measured [1] in a symmetric multi quantum well structure. The QEE was measured using a tunable CO_2 laser in the spectral range 9.3-10.6 μm for few wavelengths and the quadratic dependence on the dc electric field was established. The experimental results, combined with calculations of the induced intersubband birefringence and the (screened) internal field in the QW, indicate a strong enhancement of the related third-order susceptibility over bulk values and an agreement to theoretical calculations; a critic on the results and on their interpretation, following additional experiments and observations, is attempted later on.

The structure used in this experiment was grown by MBE on a semi-insulating GaAs substrate. The active region consisted of 25 periods of an 85 Å GaAs well followed by a 315 Å $Al_{0.4}Ga_{0.6}As$ barrier. The central 65Å of the wells are n-doped with Si at a density of $n = 4x10^{18}$ cm^{-3}. The MQW region is sandwiched between two buffer layers consisting of 3000Å of undoped $Al_{0.4}Ga_{0.6}As$ and 1μm of n-doped ($n = 4x10^{18}$ cm^{-3}) GaAs. The structure is shown in Figure 7.1.

We measured the intersubband absorption spectrum in the waveguide geometry, as described in chapter 3. We also measured the dependence of the absorption on the

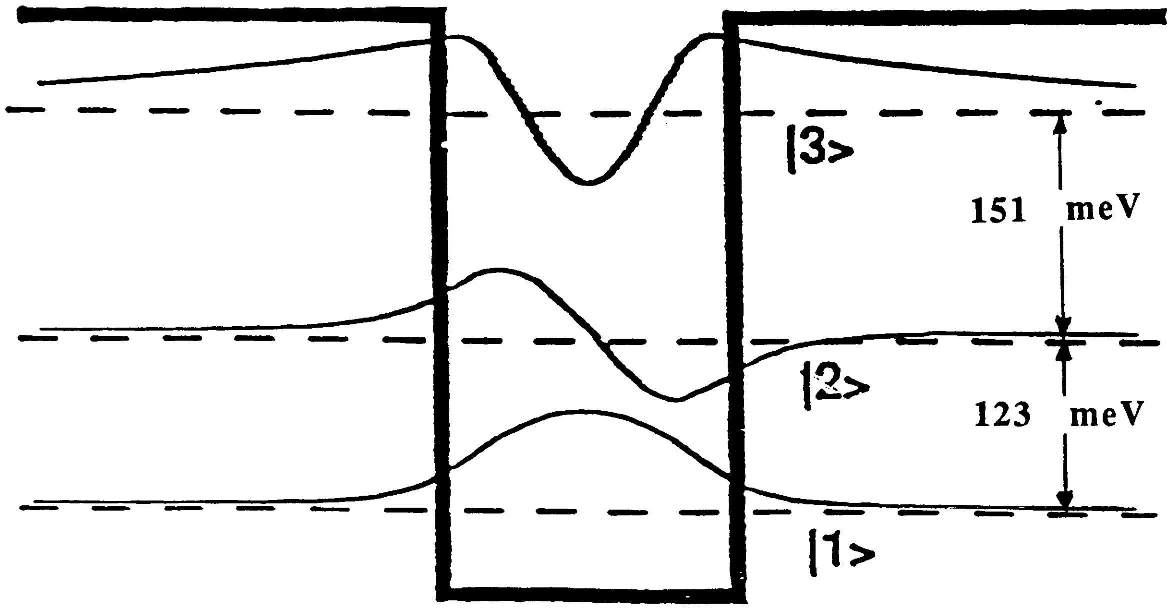

Figure 7.1. The conduction band diagram for one quantum well in the structures used to observe third-order nonlinearities via intersubband transitions. For the quadratic electrooptic effect, the doping in the central region was very high, $n = 4\times10^{18}$ cm^{-3}. In subsequent experiments, featuring the observation of phase conjugation and the optical Kerr effect, lighter doping was used in samples with the same configuration.

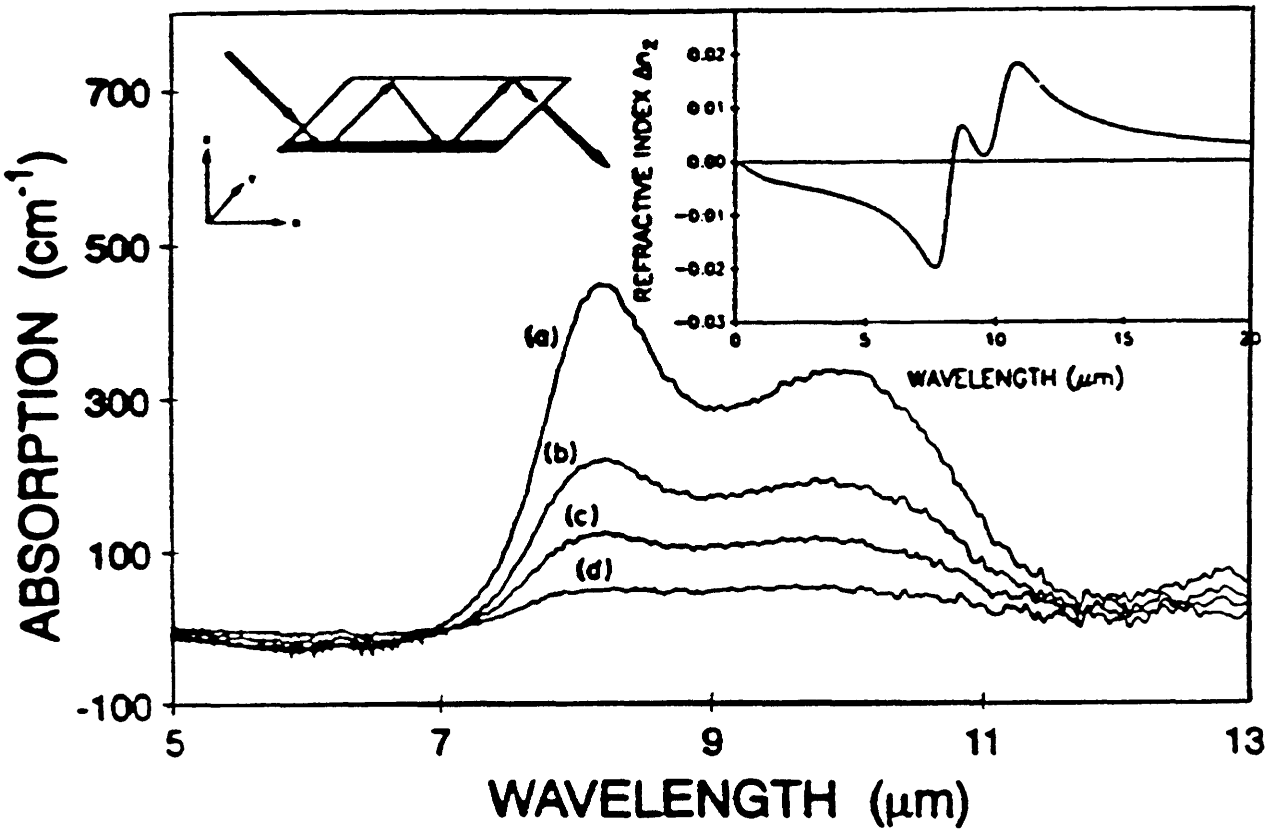

Figure 7.2. The intersubband absorption of the QW structure versus the infrared wavelength for various angles θ of the entrance polarizer. (a) θ=30°, (b) θ=45°, (c) θ=60°, (d) θ =90°. The inset on the right shows the change of the refractive index, calculated from the absorption data by the Kramers-Kroning relationship. The inset on the left shows the multi-pass geometry used in the experiment.

polarization angle, to check for the expected $\cos^2\phi$ dependance, as requested by the dipole transition selection rules. These measurements are shown in Figure 7.2. The two absorption resonances at 8.2 μm and 10.2 μm do indeed obey the intersubband selection rules. These peaks are related to transition energies e_{12} =123 meV and e_{23} = 151 meV, respectively, correspond to the $1\mapsto2$ and the $2\mapsto3$ transitions in the QW. The second transition is due to the very high electron density in the well, which results in an appreciable population in the second state. These energies are in good agreement with our calculations of the QW energy levels that give e_1 = 42 meV, e_2 = 165 meV and e_3 = 335 meV.

In order to measure the electrically induced intersubband birefringence $\Delta\varepsilon_z$ (where ε_z is the principal dielectric constant in the z direction), a standard cross-polarizer experimental set-up, with a lock-in detection scheme, was used to measure the electrically induced signal. The set-up is shown in Figure 7.3.

The sample was processed using standard photolithographic methods into 100-μm-wide, 2-μm-deep n-i-n mesas with AuGeNi alloy contacts at both sides of the mesa. The sample was mounted using In soldering with Au wire bonds providing the electrical connections. A linearly polarized CO_2 laser beam was focused onto one facet of the sample (with a power density of the order of 10^4 W/cm^2), while a cross-polarizer and a pyroelectric detector were used to detect the outcoming light. In order to ensure that the cross-polarizer was at the right angle, the light was chopped and a lock-in amplifier was used to align the polarizer at the angle where the signal was minimized. A square wave voltage pulse, at a repetition rate of 250 Hz, was then

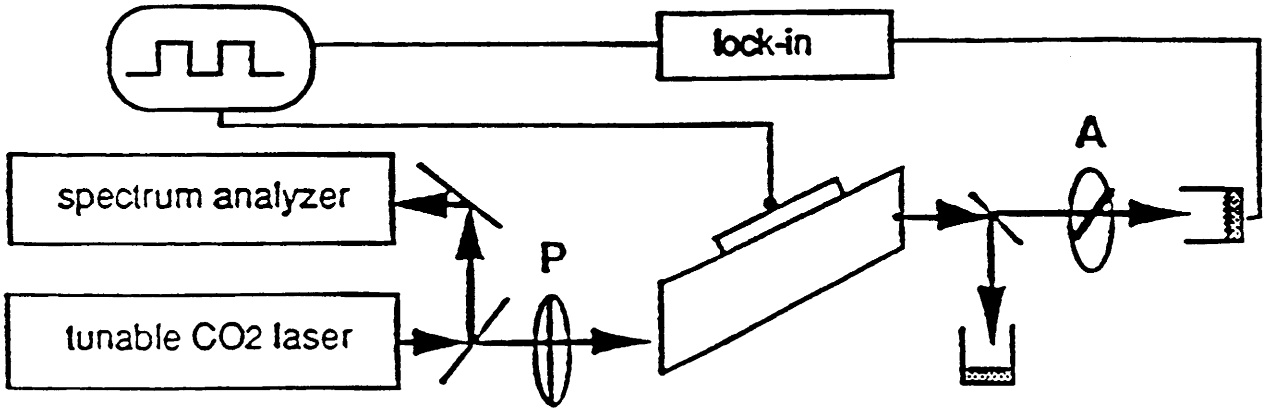

Figure 7.3. The experimental system used to observe and measure the dc Kerr effect. Radiation from a tunable CO_2 laser, is shed on the sample held in the multipass geometry. A cross-polarizer technique is used to measure the relative phase shift. The lock-in detection insures that the observed effects are synchronous with the applied dc field.

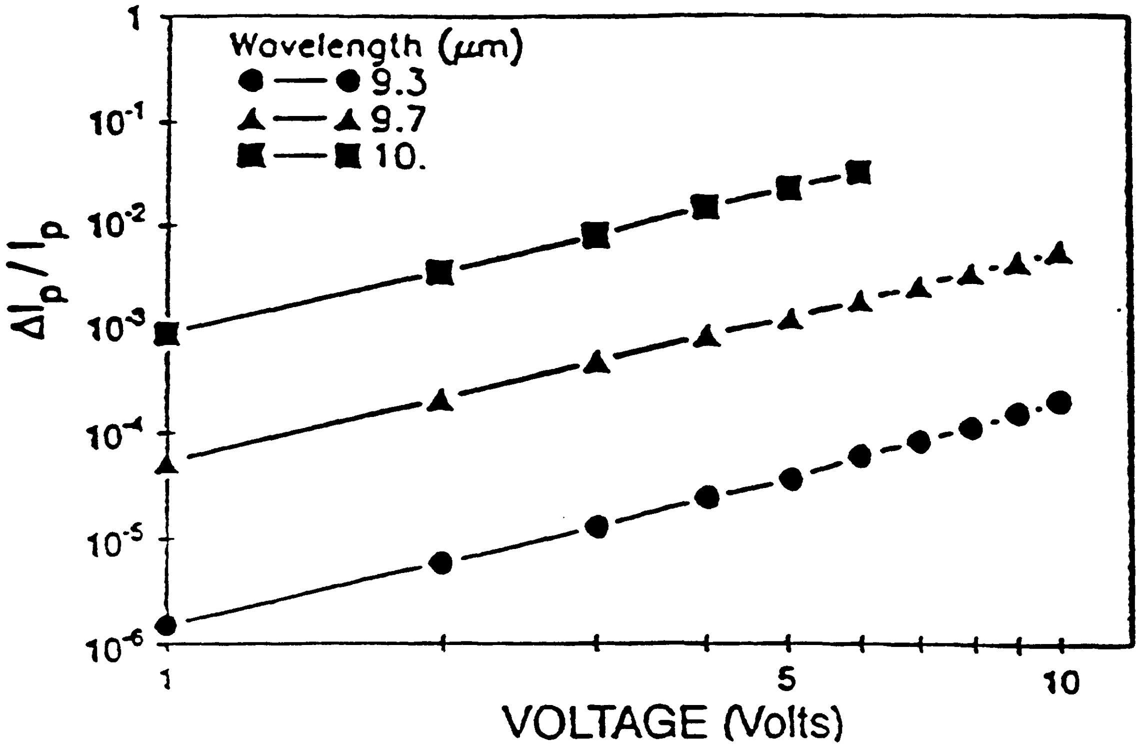

Figure 7.4. The experimental results for the relative change of detected intensity as a function of the applied voltage, for various wavelengths of the CO_2 laser, in the cross polarizers set-up. As shown in the text, these results can be used to calculate the nonlinear refractive index change.

applied across the mesa and a lock-in amplifier was used to detect the change of the signal due to the applied voltage for several infrared wavelengths of our CO_2 laser. The results of this experiment are shown in Figure 7.4.

In order to relate the measured signal to the electrically induced phase retardation, one can write the intensity of the light after the polarizer, I_p, as follows

$$I_p = I_o \sin^2 (\phi_o - \phi_1 E_o - \phi_2 E_o^2) \tag{7.6}$$

where E_o is the dc electric field and ϕ_o, ϕ_1 and ϕ_2 are, respectively, the zero order, linear and the quadratic intersubband induced phases. They can be directly related to the linear and quadratic electrooptical coefficients via the following relations

$$\phi_o = (\varepsilon_z^{1/2} - \varepsilon_y^{1/2})\, k_o L/2 \tag{7.7}$$

$$\phi_1 = \varepsilon_z^{3/2}\, r_{33}\, k_o L/4 \tag{7.8}$$

$$\phi_2 = \varepsilon_z^{3/2}\, K_{333}\, k_o L/4 \tag{7.9}$$

where ε_x, ε_y, ε_z are the principal dielectric costant in the 3 directions, k_o is the wave vector of the light, L is the optical path and r_{33} and K_{333} are the linear and Kerr coefficients defined by

$$\Delta\left(\frac{1}{\varepsilon}\right)_i = r_{ij} E_j + K_{ijk} E_j E_k \tag{7.10}$$

Note that we are using the contracted index convention used after the transformation to the principal axes. This explains why each tensor has one index less than its full rank require. Also, Φ_o in Eq. 7.7, should include the phase shift experienced by one polarization with respect to the other in the total internal reflections undergone by the beams along the optical path in the multipass geometry of this experiment.

Hence, the change of I_p with respect to the electric field E_o that is proportional to $|E_o|^2$, is related to ϕ_2 by

$$\phi_2 = \frac{\eta}{\sin(2\phi_o)} \tag{7.11}$$

where

$$\eta = \frac{\Delta I_P / I_P}{|E_o|^2} \tag{7.12}$$

It should be noted that the linear (Pockels) electrooptic effect is vanishing in a centrosymmetric structure. Application of the electric field breaks the symmetry, and we have seen that second-harmonic generation, for instance, can be obtained in this way. However, compared to the other terms in Eq. 7.6, the contribution of ϕ_1 was observed during the experiment to be negligible, since the results did not depend on the sign of the applied external field. Consequently, terms proportional to $\phi_1^2 E_o^2$ are neglected in Eq. 7.11. The birefringence induced by the intersubband transition, $\phi_1(\lambda)$, and due to the change in the refractive index, can be calculated from the absorption data through the Kramers-Kroning relations, as displayed in the inset of Fig. 7.2.

The value of the Kerr coefficient K_{333} can be calculated from perturbation theory. Allowing for the symmetry of the crystal and taking only near-resonant terms, one can simplify the standard formula, which includes, a priori, 48 terms [2], to the following

$$K_{333} = \frac{4\pi f n e^4}{\varepsilon^3 \hbar^3} \sum_{n,m,k,s} \frac{\langle Z_{n,m} \rangle \langle Z_{m,k} \rangle \langle Z_{k,s} \rangle \langle Z_{s,n} \rangle}{(\omega_{mn} - \omega - i\,\Gamma_{mn})\,(\omega_{kn} - \omega - i\,\Gamma_{kn})\,(\omega_{sn} - \omega - i\,\Gamma_{sn})} \tag{7.13}$$

where the exchange dipole moments matrix elements and the frequencies labeled by the running indices in the summation correspond to transitions among the various levels in the well. Also n is the 3D electron density in the wells, f the filling factor of the structure, and $1/\Gamma_{ij}$ are the dephasing times.

Figure 7.5 shows a calculation of the Kerr coefficient based on Eq. 7.13. The calculation includes a dephasing time $1/\Gamma$ of 0.14 psec. The experimental results, appearing as triangles in Fig. 7.5 , have been obtained by scaling the field to take into account the screening, according to $E_o = 0.42\ E_{ex}$. To calculate this relation between the applied external field and the internal field $E_o = E_{ex} - E_{sc}$, one has to solve self-consistently Poisson's equation for the screening field together with Schroedinger's

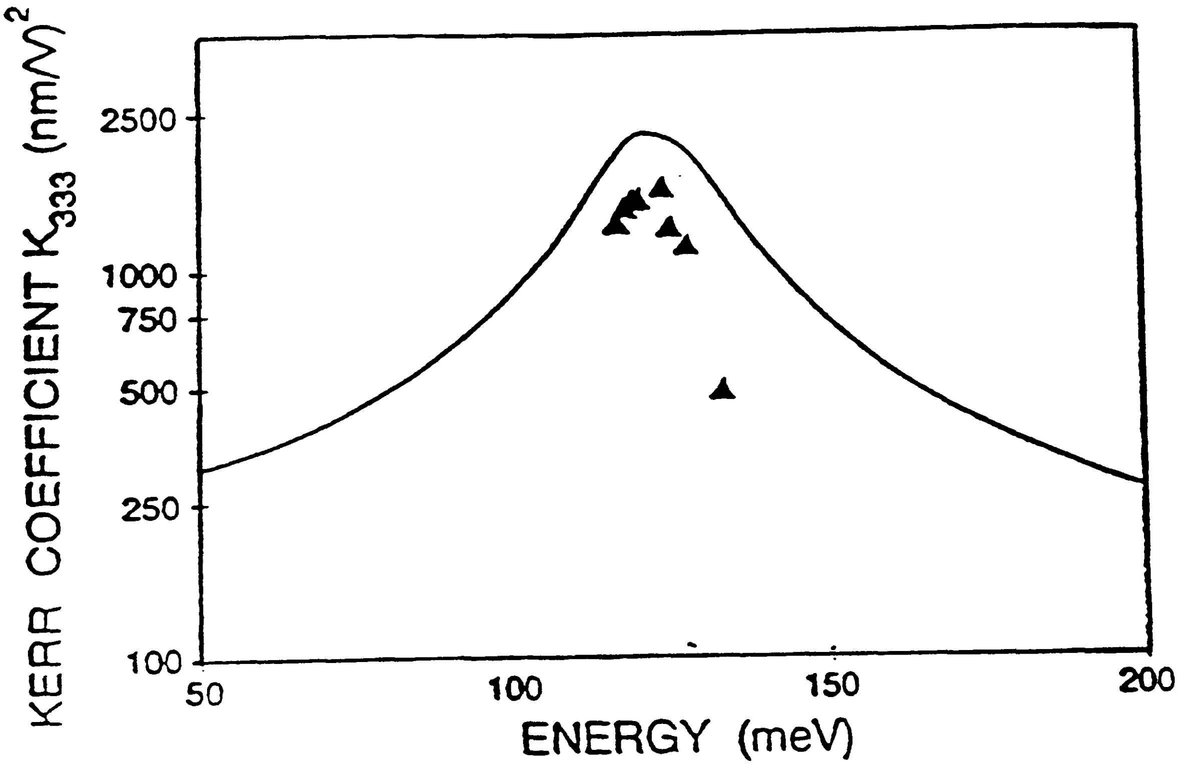

Figure 7.5. The calculation of the Kerr coefficients based on perturbation theory. The values inferred from the experimental results, including correction for the screening and an adjusted dephasing time of 0.14 psec, are superimposed as triangles. The spectral dependence of the experimental results demonstrate the quadratic electro-optic effect.

equation in the presence of the internal field. Alternatively, and for low fields, one can resort to perturbation theory. (These calculations for the screening field, to yield $E_o = 0.42\ E_{ex}$, were performed by J. Feng).

The largest value inferred for K_{333}, as from data measured at 10.0 μm is 1720 $(nm/V)^2$, reportedly six orders of magnitude larger than in bulk GaAs.

However a critical analysis of these data is in order here, especially from insight and information gathered in subsequent work. The main result of this work is the demonstration of the existence of a third order dc Kerr effect via intersubband transitions. This is evidenced by the qualitative fit of the calculated spectrum of K_{333} to the data points inferred from the experimental results. However the accuracy of the absolute measurement of the third-order susceptibility was probably quite poor, in view of the omission of factors influencing the zero-order phase. Also the use of dephasing times as an adjustable parameters, taken from results in the literature, could introduce some large errors. These considerations indicate that a more conservative estimate of the magnitude of the third-order nonlinearity (scaling down about one to two order of magnitudes) might be in order, but the results is still an impressive enhancement. Another point to ponder is the poor choice of the sample used in the experiment. A very high doping density inhibits the possible absorptions and, as a consequence, tends to diminish the magnitude of the nonlinearity, due to the partial filling of the second subband. All these considerations were taken into account for improvement in subsequent experiments, which are described later on. Together with the possible critics and remarks, this work stands in its importance as the first demonstration of third-order nonlinearities via intersubband transitions.

7.4 Phase conjugation

In this section we describe the observation of phase conjugation at 10.6 μm via intersubband third-order nonlinearities in a GaAs/AlGaAs multi-quantum well structure [3].

The sample used was grown by molecular beam epitaxy and consisted of 25 periods of the following: an 85-Å wide GaAs quantum well, clad by $Al_{0.4}Ga_{0.6}As$ barriers 315 Å wide. Each quantum well was Si-doped to $n=2x10^{18}$ cm^{-3} in the central 65 Å. The superlattice was sandwiched between two undoped layers of 0.3 μm , which served to separate the superlattice from the contact layers (not used in this experiment). The structure was grown on a semi-insulating GaAs substrate.

Figure 7.6 shows the absorption spectrum of the sample, normalized to that of the non-absorbing polarization, as obtained by measurement with a Mattson Fourier Transform Spectrometer. The wavelength used in the experiment (10.6 μm) is slightly shorter than the absorption peak centered at 11.3 μm.

Our experimental system is sketched in Figure 7.7, in which the sample is shown larger than scale, in order to bring out details of the waveguiding geometry. The side input face of the sample as well as the opposite back facet were lapped to 45^{o}.

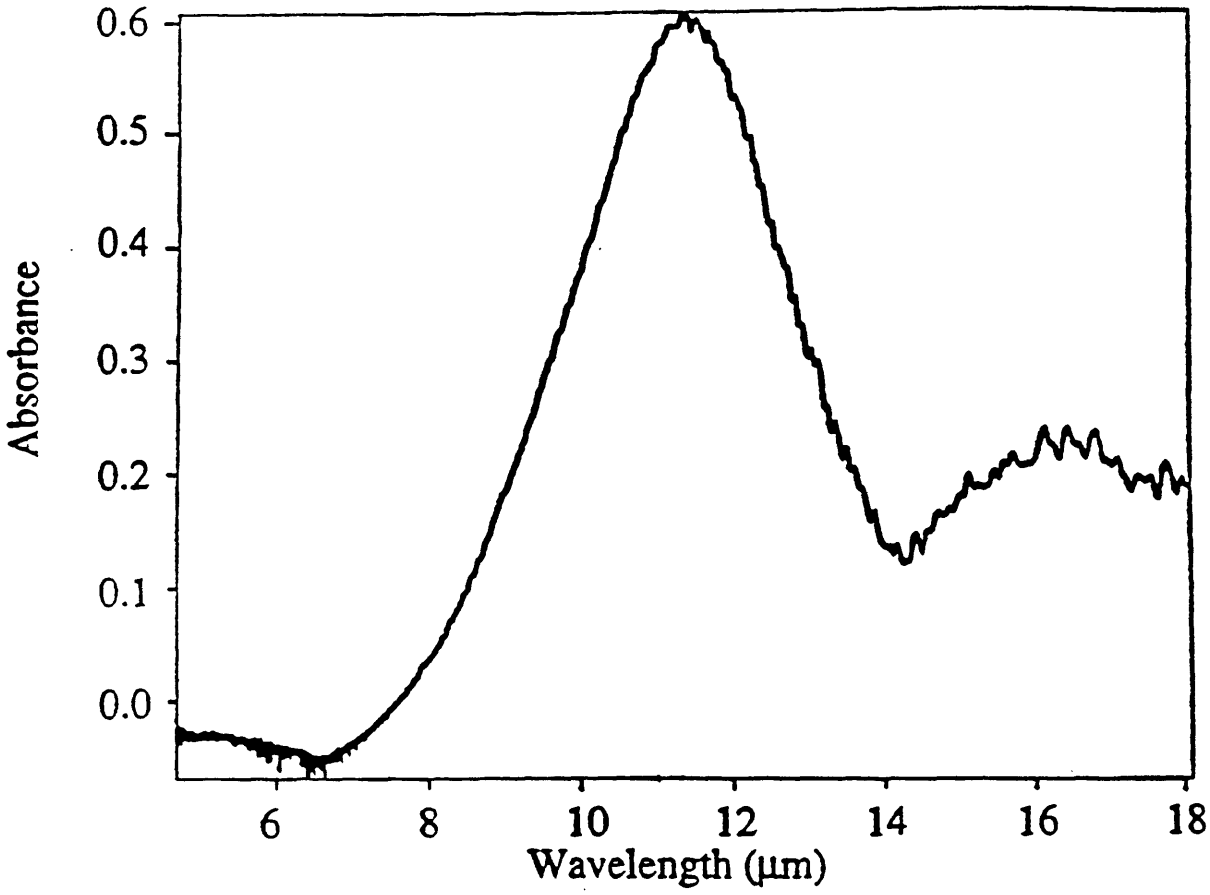

Figure 7.6. Absorption spectrum of the sample used in the phase conjugation experiment. Note that only one absorption peak is present, due to the lower doping of this sample, as compared to the sample used in the dc Kerr effect experiments.

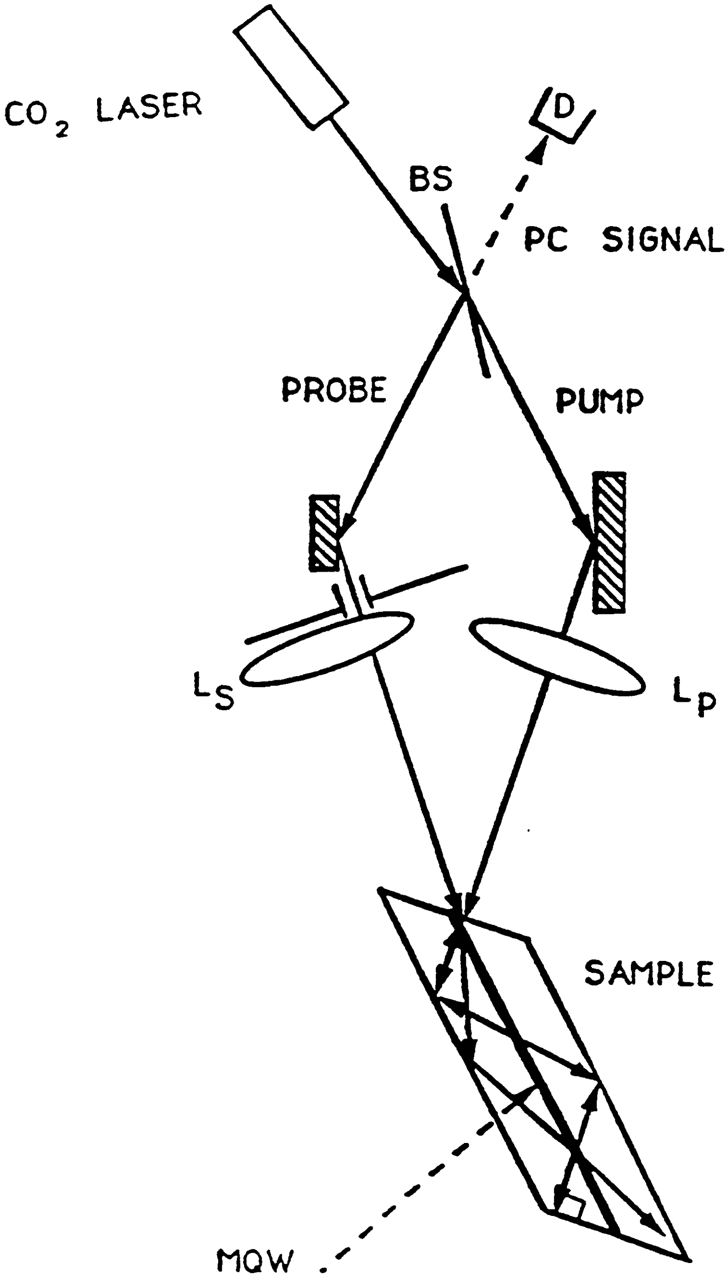

Figure 7.7. Sketch of the experimental system used for the observation of phase cojugation. The sample is enlarged out of proportion to show the multipass geometry. The phase conjugate beam is observed with detector D.

The 10.6 μm radiation from an air-cooled CO_2 laser is split by beamsplitter BS into two beams. The first beam, acting as the pump, is focused by the lens L_p onto the sample edge at normal incidence; the second (probe) beam, is focused on the sample through a second lens, L_s at an angle of 15^o from the normal. The optical path difference is less than one centimeter and is much less than the coherence length of the laser. The (normal) reflection of the first pump beam from the back facet inside the sample provides the second counter-propagating pump beam. The degenerate four-wave mixing process is completed with the creation and amplification of the phase conjugate beam, which retraces, in reverse, the path of the incident probe beam and whose power is measured by a pyroelectric detector D. Since this arrangement corresponds to the canonical phase conjugation configuration, phase matching obtains automatically for equal pump powers.

To determine whether the reflected beam was indeed the phase conjugate of the incident probe beam, we verified that apertures placed at different points along the path, which were just big enough so as not to interfere with the incident probe beam, had negligible influence on the reflected phase conjugate power. Moreover, the probe beam path was scanned to pass through different regions, including the outer regions, of the convex focusing lens (L_S in Fig.2): in this way the lens acted as a strong phase aberrator; yet, in each configuration, the aberration was self-corrected by the phase conjugated beam, and the retraced path and shape of the beam were the same.

Maximum phase conjugate reflectivity was observed when the incident laser beams were polarized consistent with the selection rules for intersubband absorption (normal to the well interface); the absorption was monitored by an additional detector at the back facet of the sample. When the polarization was in the perpendicular direction, (parallel to the well interface) - the phase conjugate beam all but disappeared, with an extinction ratio larger than 15:1.

The intensity of the phase conjugated beam is given by

$$I_{pc} = I_{probe} \frac{4|\kappa|^2 e^{-\alpha L} \tan^2(|\kappa_{eff}|L)}{[\alpha \tan(|\kappa_{eff}|L) + 2\kappa_{eff}]^2} \tag{7.14}$$

I_{pc} and I_{probe} are the intensities of the phase conjugate and the probe beams, respectively; L is the interaction length as obtained from the overlap of the beams in the superlattice region during their multipass path in the waveguide, k_{eff} is the effective nonlinear coupling coefficient, given by

$$\kappa_{eff} = \sqrt{|\kappa|^2 e^{-\alpha L} - (\alpha/2)^2} \tag{7.15}$$

and k is defined (in cgs units) as

$$\kappa = \frac{2\pi\omega}{cn} \chi^{(3)} A_1 A_2 \tag{7.16}$$

where ω is the lightwave frequency, A_1 and A_2 are the pumps field amplitudes, $|\chi^{(3)}|$

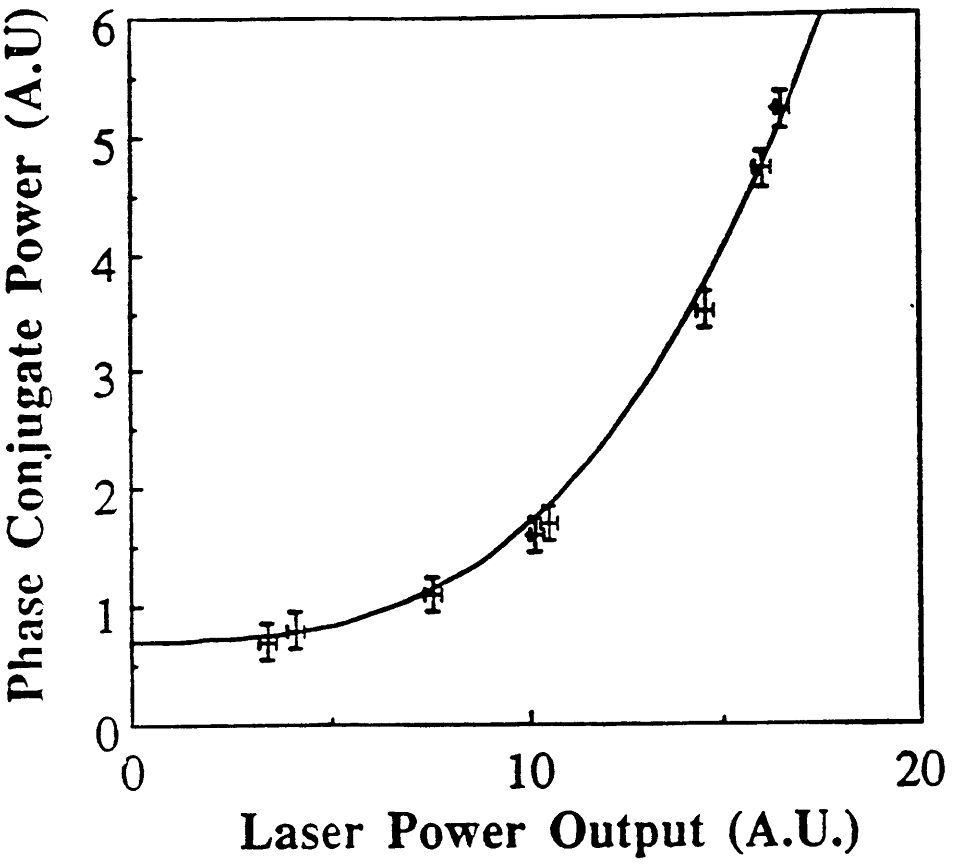

Figure 7.8. Experimental data on the dependence of the phase conjugate signal power on the power output of the laser. The cubic dependence confirms the presence of the strong third-order nonlinearity.

is the magnitude of the third-order nonlinear susceptibility in esu units, and α is the absorption coefficient in the superlattice. For situations in which $\tan(k_{eff}L) \cong k_{eff}L$, as in our experiment, the intensity of the phase conjugated beam is thus proportional, in addition to the probe beam intensity, also to the intensities of the two pump beams.

Figure 7.8 shows the measured dependence of the phase conjugate signal power on the power output of the laser. Since the intensities of the two pump beams as well as that of the signal are, each, proportional to the laser power output, a cubic dependence is expected for the phase conjugate power as a function of the laser power output. The experimental data of Fig. 7.8 display the expected cubic law dependence, thus confirming the involvement of a third-order nonlinearity. From a measurement of the actual power in each of the four beams, we obtained for the reflectivity of this "phase conjugate mirror" $\eta = I_{pc}/I_{probe} = 2\mathrm{x}10^{-3}$ uncorrected for Fresnel reflections, and the value of $\chi^{(3)}$ was determined, from the experimental data, to be $7\mathrm{x}10^{-5}$ esu.

This experiment, to our best knowledge is the first observation of phase conjugation in a multiquantum well GaAs sample. Almost degenerate four-wave mixing has been observed by another group [4], and the value reported for the third-order susceptibility is close to the one reported here.

Verification of the magnitude of the intensity-dependent refractive index and the real part of the third-order susceptibility was attempted through an additional experiment, the observation of the optical Kerr effect [5]. The sample used was of the same composition as the one employed in the phase conjugation experiment, but with a slightly lower doping (n=1.5x10^{18} cm^{-3}). The value induced from this measurement was $\mathrm{Re}\{\chi^{(3)}\} \approx 4\mathrm{x}10^{-5}$ esu; due to the nature of the experiment, the accuracy was no better than 50%. However this was an additional confirmation to the order of magnitude of the large nonlinearities associated with intersubband transitions near resonance.

7.5 Conclusions

We have described in this chapter our observations of third-order nonlinear effects via intersubband transitions, all linked to the intensity-dependent index of refraction. In different experiments, performed on different samples, we were able to measure very large values of the third-order susceptibility. On top of all the different observations and measurements, as for importance and interest, stands the first observation of phase conjugation in a multi-quantum well sample of GaAs.

Additional third-order effects via intersubband transitions were studied by others in the last year or so [4,7,8] and large enhancements over bulk values were recorded too.

References

[1] A. Sa'ar, N. Kuze, J. Feng, I. Gravé and A. Yariv, Appl. Phys. Lett. 61, 1263 (1992).

[2] N. Bloembergen, H. Lotem, and R.T. Lynch, Ind. J. Appl. Phys. 16, 151 (1978).

[3] I. Gravé, M. Segev and A. Yariv, Appl. Phys. Lett. 60, 2717 (1992).

[4] D. Walrod. S.Y. Auyang, P.A. Wolff, and M. Sugimoto, Appl. Phys. Lett. 59, 2932 (1991).

[5] M. Segev, I. Gravé and A. Yariv, Appl. Phys. Lett. 61, 2403 (1992).

[6] K.J. Kuhn, G.U. Iyengar, and S. Yee, Appl. Phys. Lett. 70, 5010 (1991).

[7] C. Sirtori, F. Capasso, D.L. Sivco, and A.Y. Cho, Phys. Rev. Lett. 68, 1010 (1992).

[8] C. Sirtori, F. Capasso, D.L. Sivco, and A.Y. Cho, Appl. Phys. Lett. 60, 2678 (1992).